UCSF

UC San Francisco Electronic Theses and Dissertations

Title
Biologic Drivers and Cellular Origins of Meningioma

Permalink
https://escholarship.org/uc/item/39h1h992

Author
Choudhury, Abrar Rahman

Publication Date
2021

Supplemental Material
https://escholarship.org/uc/item/39h1h992#supplemental

Peer reviewed|Thesis/dissertation

Biologic Drivers and Cellular Origins of Meningioma

by
Abrar Choudhury

DISSERTATION
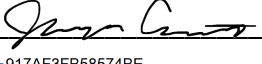Submitted in partial satisfaction of the requirements for degree of
DOCTOR OF PHILOSOPHY

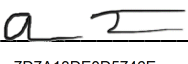in

Biomedical Sciences

in the

GRADUATE DIVISION
of the
UNIVERSITY OF CALIFORNIA, SAN FRANCISCO

Approved:

Joseph Costello
Chair

David Raleigh

Aaron Tward

_____

_____
Committee Members

Dedication

This dissertation is dedicated to my family and friends, who have supported and helped

me every step of the way along this journey.

Acknowledgements

First and foremost, I would like to thank Dr. David Raleigh for his mentorship and guidance over the past three and a half years. It has been a privilege and honor, as well as a wonderful learning experience, to be his first graduate student. I did not fully know what to expect when joining his lab in its infancy, but my experience working with David met and exceeded all of my expectations. He has served as an exemplary role model, mentor, and friend, and I will forever be grateful for everything he has taught me. In addition to nurturing my skills as a scientist by helping me improve my experimental abilities, scientific writing, and critical thinking, he has also given me countless advice about being a physician-scientist and about life in general. I know my experiences in the lab and lessons learned will serve as a strong foundation for the rest of my career.

I have had several other scientific mentors during my time in graduate school, who have guided me in countless ways. Dr. Joseph Costello mentored me during my first rotation, and remained a mentor in both unofficial and official capacities, serving on both my qualifying exam and dissertation committees. Dr. Aaron Tward, my MSTP advisor, taught me countless things about the physician-scientist pathway and MD-PhD program. He later also served on my qualifying exam and dissertation committees. The scientific advice and mentorship I received from Joe and Aaron directly improved my projects and scientific skills, and I am extremely grateful for all the time they spent giving me feedback and mentoring me.

I would be remiss not to mention the numerous scientific mentors I had before graduate school, without whom I would have never had the opportunity to join the UCSF MSTP. Dr. Yibin Kang, my undergraduate research mentor, provided me with rigorous

and comprehensive training in all aspects of molecular biology. I did not fully appreciate the importance of the strong foundational background and broad experimental repertoire I received under his mentorship until coming to graduate school. Many other mentors helped pave my path to UCSF as well. Dr. Puragra Guhathakurta gave me my first opportunity to engage in hypothesis-driven academic research and learn scientific data analysis. Dr. Hilary Coller allowed me to work in a biology lab environment despite my lack of any prior experience. Finally, Dr. Trever Bivona provided me with my first foray into cancer biology research, which set the stage for all my subsequent research experiences.

At UCSF, I am incredibly fortunate to have been a part of the Raleigh Lab, which has been a fun, supportive, and tight-knit community. Thank you to all current and former Raleigh Lab members who contributed to this community (and continue to do so, as the line between current and former member is often quite blurred): Addie Cady, Tim Casey-Clyde, Will Chen, Vikas Daggubati, Charlotte Eaton, Sydney Lastella, John Liu, Calixto-Hope Lucas, Stephen Magill, Minh Nguyen, Kyounghee Seo, Harish Vasudevan, Sarah Findakly Oshima, Chetna Gopinath, and Corinna Conroy.

I have been very lucky to have had a supportive environment outside of lab as well. My closest friends at UCSF have been my MSTP classmates: Marissa Chou, Fabian Fernandez, Sravani Kondapavulur, Elizabeth McCarthy, Cody Mowery, Marci Rosenberg, Iowis Zhu, and Larry Zhu. Thank you all for being better friends than I could have ever hoped for and for making us the best MSTP class. I would also like to acknowledge the leadership and administration within the MSTP and the Biomedical Sciences program who supported me in numerous ways over the years and answered my many, many

emails and questions. Thank you to Dr. Mark Anderson, Dr. Mark Ansel, Geri Ehle, Demian Sainz, Amanda Andonian, Ned Molyneaux, and Andres Zepeda.

Thank you to my many and dear friends who encouraged and helped me along this path in countless ways, big and small. Words on this page are not sufficient to express my gratitude, so I hope to see you all in person sooner rather than later to properly give my thanks. A woefully incomplete list follows: Anita Alem, Monika Alem, Simon Ammanuel, Nic Barton, Saumya Bollam, Ryan Budnick, Addie Cady, Cissy Chen, Naveed Chowdhury, Stephen Cognetta, Megan Dare, Devan Diwanji, Tina Doan, Caleb Edwards, Molly Fisch-Friedman, Shabab Hussain, Shannon Julian, Rex Lee, Kathy Li, Michael Li, Daniel Liu, Katie Little, Robin Lea, Megan Lo, Minhaz Mahbub, Lauren McHenry, Antara Murshed, Stacey Park, Richie Perrine, Hansen Qian, Amreen Rahman, Arifeen Rahman, Paarth Shah, Rebecca Tang, Mark Tengi, Mat Teoh, Aditya Trivedi, Ben Wheeler, Serena Wong, Elizabeth Yang, and Barbara Zhan.

Finally, I would like to thank my family. To Maa and Baba, thank you for nurturing my scientific interest from a very young age and for the countless Tupperware filled with home-cooked meals. To Zareen, thank you for being an amazing sister and for all the gifts, conversations, and time spent together.

Contributions

This dissertation was done under the direct supervision and guidance of Dr. David Raleigh and encompasses three and a half years of graduate education and research. Funding for this research was acquired by Dr. Raleigh and myself, with additional contributions noted in the acknowledgement section of each chapter. Additional contributions are described below.

Chapter 2 is under review as follows:

Choudhury A, Magill ST, Eaton CD, Prager BC, Chen WC, Cady MA, Seo K, Lucas C-HG, Casey-Clyde TJ, Villanueva-Meyer JE, Lam T-C, Pu JK-S, Li L-F, Leung GK-K, Swaney DL, Vasudevan HN, Liu SJ, Chan JW, Qiu Z, Zhang MY, Martin MV, Susko MS, Braunstein SE, Oberheim Bush NA, Schulte J, Butowski N, Sneed PK, Berger MS, Krogan NJ, Perry A, Phillips JJ, Solomon DA, Costello JF, McDermott MW, Rich JN, Raleigh DR. Meningioma DNA methylation grouping reveals biologic drivers and therapeutic vulnerabilities.

The introduction of Chapter 3 is adapted from the following published book chapter:

Choudhury A, Raleigh DR. Preclinical models of meningioma: Cell culture and animal systems. Handb Clin Neurol. 2020;169:131-136. doi: 10.1016/B978-0-12-804280-9.00008-1. PMID: 32553284.

"Cancer's life is a recapitulation of the body's life, its existence

a pathological mirror of our own."

-Siddhartha Mukherjee, *The Emperor of*

All Maladies: A Biography of Cancer

Biologic Drivers and Cellular Origins of Meningioma

Abrar Choudhury

ABSTRACT

Meningiomas arising from the meningothelial lining of the central nervous system are the most common primary intracranial tumors, and a significant cause of neurologic morbidity and mortality. There are no effective medical therapies for meningioma patients, and new treatments have been encumbered by limited understanding of meningioma biology. DNA methylation profiling provides robust classification of brain tumors, but has not informed new treatments for patients.

Here we use DNA methylation profiling on 565 meningiomas, controlled for confounding artifacts from copy number variants and integrated with genetic, transcriptomic, biochemical, and single-cell approaches, to show meningiomas are comprised of 3 groups with distinct clinical outcomes, biological drivers, and therapeutic vulnerabilities. Merlin-intact meningiomas have the best outcomes and are distinguished by *NF2*/Merlin regulation of glucocorticoid signaling and apoptosis. Immune-enriched meningiomas have intermediate outcomes and are distinguished by immune infiltration, *HLA* expression, and lymphatic vessels. Hypermitotic meningiomas have the worst outcomes and are distinguished by convergent genetic mechanisms misactivating the cell cycle. Translating these findings, we show cell cycle inhibitors block Immune-enriched and Hypermitotic meningioma growth in cell culture, organoids, xenografts, and patients.

To extend the relevance of our findings, we use single-cell RNA sequencing of 8 human meningiomas, 3 canine meningiomas, and 1 human hemangiopericytoma to identify Notch3$^+$ perivascular cells as a potential cell of origin for meningeal tumors. This

perivascular cell population is conserved across meningeal tumors in both humans and canines and across normal meningeal tissue in both humans and mice. These findings set the stage for developing new mouse models of meningioma, which will accelerate and enhance our ability to study meningioma biology, such as interrogating the pathways and phenotypes identified from DNA methylation groups. Moreover, new mouse models will also allow us to study meningiomas in the context of the immune system and test the efficacy of drugs in a more physiologic setting. Our results establish a framework for understanding meningioma biology, provide the basis for new meningioma treatments, and lay the foundation for future meningioma studies.

Contents

List of Figures

List of Tables

Chapter 1: Introduction

Meningiomas, tumors which arise from the meningothelial lining of the central nervous system, are the most common primary intracranial tumors and account for one-third of all primary central nervous tumors[1]. Elderly age and female sex are some of the strongest risk factors for meningiomas, which are a significant cause of neurologic morbidity and mortality[2]. Histologic comparisons of meningiomas with healthy meningothelial tissue have revealed similarities between tumor cells and arachnoid cap cells, suggesting these as possible meningioma progenitor cells[3]. The World Health Organization (WHO) uses mitotic activity and adverse histopathological features to classify meningiomas into three grades, which correlate with clinical outcome[2]. High-grade meningiomas (WHO grade 2 and 3) account for 25-30% of diagnosed cases[4]. The WHO also stratifies meningiomas into 15 subtypes based on histologic features, and although some of these subtypes correlate with WHO grade, the clinical relevance of the majority of subtypes remains unknown[2].

Surgery and radiation are the mainstays of meningioma treatment and can effectively treat most low-grade meningiomas (WHO grade 1). While low-grade meningiomas are typically benign and do not recur post-treatment, the majority of high-grade tumors recur, at which point there are no effective systemic or molecular therapies for these meningioma patients[5–7]. Substantial controversy exists concerning how aggressively to treat WHO grade 2 meningiomas and manage their risk of recurrence[8]. Recent studies have suggested that MIB1 labeling index, a marker of cell proliferation, can predict the risk of recurrence in patients with WHO grade 2 meningiomas and identify patients requiring more aggressive treatment regimens[9]. However, the use of MIB1

labeling index has yet to be widely adopted. Moreover, even with appropriately aggressive treatment, high-grade meningiomas often recur, and treatment options beyond surgery and radiation to mitigate this recurrence are nonexistent. The development of such new treatments has been encumbered by a limited understanding of the basic biology of meningiomas.

To elucidate meningioma biology, DNA sequencing has been performed on thousands of meningiomas. These studies have identified *NF2*, a gene located on chromosome 22, as the most commonly mutated gene, with mutations present in 60% of sporadic meningiomas[10]. *NF2* loss of function mutations vary significantly, ranging from point substitutions to monosomy 22, the most common chromosomal alteration in meningioma[11]. Further, germline *NF2* mutations are associated with neurofibromatosis type 2[12], a highly penetrant clinical syndrome associated with multiple meningiomas, and other tumors affecting the central and peripheral nervous system[13]. The protein product of *NF2*, Merlin, has been shown to inhibit cell growth by mediating contact inhibition *in vitro* in epithelial cells, although these observations have not been replicated in meningioma cells[14]. Merlin's homology to ERM family proteins originally implicated it as a scaffolding protein, linking transmembrane receptors to intracellular effectors[15,16]. However, more recent structural studies indicate that Merlin, unlike other scaffolding proteins, adopts a closed conformation regardless of whether it is active or inactive[17,18]. Thus, Merlin's role in tumorigenesis broadly and meningioma specifically remains poorly understood.

Several other recurrent mutations have been identified in meningiomas, including mutations in *TRAF7*, *KLF4*, *AKT1*, *SMO*, *POLR2A*, and *TERT*[19–21]. However, each

individual gene is mutated in only a tiny fraction of meningiomas[19], raising questions as to whether these genes and pathways are relevant to the biology underlying the majority of meningiomas. Descriptive analyses have revealed that these genes are typically mutated in meningiomas lacking *NF2* mutations. Notably, *TRAF7*, *AKT1*, and *KLF4* mutations are found in specific WHO histologic subtypes and *SMO* mutations are often identified in olfactory groove meningiomas[19]. While these correlative findings suggest non-*NF2* mutations may drive meningioma histopathology and location, no studies have shown causal biologic mechanisms linking these mutations to any of the aforementioned phenotypes.

Given the limitations of DNA mutational analysis in understanding meningioma biology, several other approaches to investigating meningiomas have been undertaken. One of these is DNA methylation profiling, which provides robust classification and differentiation across brain tumor types[22]. However, attempts to use DNA methylation profiling to identify biologically meaningful subgroups within meningiomas have been variable and unfruitful. Prior studies have reported between 2 and 6 meningioma methylation groups, and reanalysis of previously published data have prompted disagreements on the number of clusters suggested by the data[23–27]. Many of these DNA methylation groups have overlapping patient outcomes, calling into question the clinical relevance of these groups. One study attempted to mitigate this by merging two different DNA methylation subgroups based on similar clinical outcomes[23]. However, these analyses obscure methylation-based biologic differences between groups. Moreover, no DNA methylation studies of meningiomas have accounted for artifacts from copy number variants, which are highly prevalent in meningioma[28,29]. While biologic differences may

underlie some of the group classifications of these prior studies and some of the studies hypothesize about the importance of specific genes or copy number alterations, none of them provide experimental evidence to justify any speculative differences. Therefore, fundamental questions remain concerning the relevance and role of DNA methylation grouping in elucidating meningioma biology.

Beyond DNA-based analyses, various other small-scale studies of meningioma have been performed using transcriptomics, epigenomics, and proteomics as orthogonal means to study meningioma biology. RNA sequencing of meningiomas across WHO grades confirmed the importance of cell proliferation mechanisms in predicting tumor growth and recurrence, specifically identifying FOXM1 as a key regulator of the cell cycle in high-grade meningiomas[26]. An unbiased analysis of meningioma transcriptomes found a group of aggressive meningiomas which activate the cell cycle via loss of function inactivation of the DREAM complex[30]. Unfortunately, neither FOXM1 nor the DREAM complex are viable pharmaceutical targets. In contrast, an epigenetic analysis of enhancers and superenhancers in meningiomas revealed DUSP1, a dual specificity phosphatase upregulated in aggressive meningiomas, as a viable druggable target[31]. Finally, proteomic analyses of meningiomas suggest that larger and more aggressive meningiomas dysregulate mRNA processing, although the specific pathways involved are not understood[32]. While promising, each of these findings require validation in larger datasets and integration into a cohesive framework. The limitations of WHO grading and prior DNA methylation groupings of meningiomas suggest that new analyses of transcriptomics, epigenetics, and proteomics in the context of biologically distinct and

4

validated groups of meningiomas may provide valuable insights into meningioma biology that can be used to generate new treatment options.

References

1. Ostrom, Q. T. *et al.* CBTRUS Statistical Report: Primary Brain and Other Central Nervous System Tumors Diagnosed in the United States in 2012–2016. *Neuro-Oncol.* **21**, v1–v100 (2019).

2. Louis, D. N. *et al.* The 2016 World Health Organization Classification of Tumors of the Central Nervous System: a summary. *Acta Neuropathol. (Berl.)* **131**, 803–820 (2016).

3. Yamashima, T., Kida, S. & Yamamoto, S. Ultrastructural comparison of arachnoid villi and meningiomas in man. *Mod. Pathol. Off. J. U. S. Can. Acad. Pathol. Inc* **1**, 224–234 (1988).

4. Rogers, L. *et al.* Meningiomas: knowledge base, treatment outcomes, and uncertainties. A RANO review. *J. Neurosurg.* **122**, 4–23 (2015).

5. Brastianos, P. K. *et al.* Advances in multidisciplinary therapy for meningiomas. *Neuro-Oncol.* **21**, i18–i31 (2019).

6. Wen, P. Y., Quant, E., Drappatz, J., Beroukhim, R. & Norden, A. D. Medical therapies for meningiomas. *J. Neurooncol.* **99**, 365–378 (2010).

7. Le Van, T. *et al.* Multimodal management of surgery- and radiation-refractory meningiomas: an analysis of the French national tumor board meeting on meningiomas cohort. *J. Neurooncol.* (2021) doi:10.1007/s11060-021-03741-7.

8. Strand, P. S. & Solheim, O. The impact of authors' medical specialty on publication patterns and published results of adjuvant radiotherapy for WHO grade 2 meningiomas-a systematic review. *Acta Neurochir. (Wien)* (2021) doi:10.1007/s00701-021-04797-0.

9. Chen, W. C. *et al.* Histopathological features predictive of local control of atypical meningioma after surgery and adjuvant radiotherapy. *J. Neurosurg.* **130**, 443–450 (2018).

10.   Yuzawa, S., Nishihara, H. & Tanaka, S. Genetic landscape of meningioma. *Brain Tumor Pathol.* **33**, 237–247 (2016).

11.   Vasudevan, H. N. *et al.* Comprehensive Molecular Profiling Identifies FOXM1 as a Key Transcription Factor for Meningioma Proliferation. *Cell Rep.* **22**, 3672–3683 (2018).

12.   Rouleau, G. A. *et al.* Alteration in a new gene encoding a putative membrane-organizing protein causes neuro-fibromatosis type 2. *Nature* **363**, 515 (1993).

13.   Petrilli, A. M. & Fernández-Valle, C. Role of Merlin/NF2 inactivation in tumor biology. *Oncogene* **35**, 537–548 (2016).

14.   Chiasson-MacKenzie, C. *et al.* NF2/Merlin mediates contact-dependent inhibition of EGFR mobility and internalization via cortical actomyosin. *J Cell Biol* **211**, 391–405 (2015).

15.   Trofatter, J. A. *et al.* A novel moesin-, ezrin-, radixin-like gene is a candidate for the neurofibromatosis 2 tumor suppressor. *Cell* **72**, 791–800 (1993).

16.   Gronholm, M. *et al.* Homotypic and heterotypic interaction of the neurofibromatosis 2 tumor suppressor protein merlin and the ERM protein ezrin. *J. Cell Sci.* **112**, 895–904 (1999).

17.   Hennigan, R. F. *et al.* Fluorescence Resonance Energy Transfer Analysis of Merlin Conformational Changes. *Mol. Cell. Biol.* **30**, 54–67 (2010).

18. Ali Khajeh, J. *et al.* Molecular Conformation of the Full-Length Tumor Suppressor NF2/Merlin—A Small-Angle Neutron Scattering Study. *J. Mol. Biol.* **426**, 2755–2768 (2014).

19. Clark, V. E. *et al.* Genomic analysis of non-NF2 meningiomas reveals mutations in TRAF7, KLF4, AKT1, and SMO. *Science* **339**, 1077–1080 (2013).

20. Clark, V. E. *et al.* Recurrent somatic mutations in POLR2A define a distinct subset of meningiomas. *Nat. Genet.* **48**, 1253–1259 (2016).

21. Sahm, F. *et al.* TERT Promoter Mutations and Risk of Recurrence in Meningioma. *J. Natl. Cancer Inst.* **108**, (2016).

22. Capper, D. *et al.* DNA methylation-based classification of central nervous system tumours. *Nature* **555**, 469–474 (2018).

23. Sahm, F. *et al.* DNA methylation-based classification and grading system for meningioma: a multicentre, retrospective analysis. *Lancet Oncol.* **18**, 682–694 (2017).

24. Olar, A. *et al.* Global epigenetic profiling identifies methylation subgroups associated with recurrence-free survival in meningioma. *Acta Neuropathol. (Berl.)* **133**, 431–444 (2017).

25. Nassiri, F. *et al.* DNA methylation profiling to predict recurrence risk in meningioma: development and validation of a nomogram to optimize clinical management. *Neuro-Oncol.* (2019) doi:10.1093/neuonc/noz061.

26. Vasudevan, H. N. *et al.* Comprehensive Molecular Profiling Identifies FOXM1 as a Key Transcription Factor for Meningioma Proliferation. *Cell Rep.* **22**, 3672–3683 (2018).

27.   Harmancı, A. S. *et al.* Integrated genomic analyses of de novo pathways underlying atypical meningiomas. *Nat. Commun.* **8**, 14433 (2017).

28.   Zhou, W., Triche, T. J., Laird, P. W. & Shen, H. SeSAMe: reducing artifactual detection of DNA methylation by Infinium BeadChips in genomic deletions. *Nucleic Acids Res.* **46**, e123–e123 (2018).

29.   Bi, W. L. *et al.* Genomic landscape of intracranial meningiomas. *J. Neurosurg.* **125**, 525–535 (2016).

30.   Patel, A. J. *et al.* Molecular profiling predicts meningioma recurrence and reveals loss of DREAM complex repression in aggressive tumors. *Proc. Natl. Acad. Sci.* **116**, 21715–21726 (2019).

31.   Prager, B. C. *et al.* The Meningioma Enhancer Landscape Delineates Novel Subgroups and Drives Druggable Dependencies. *Cancer Discov.* (2020) doi:10.1158/2159-8290.CD-20-0160.

32.   Papaioannou, M.-D. *et al.* Proteomic analysis of meningiomas reveals clinically distinct molecular patterns. *Neuro-Oncol.* **21**, 1028–1038 (2019).

Chapter 2: Meningioma DNA methylation grouping reveals biologic drivers and therapeutic vulnerabilities

Introduction

Meningiomas arising from the meningothelial lining of the central nervous system are the most common primary intracranial tumors, and a significant cause of neurologic morbidity and mortality[1]. There are no effective medical therapies for meningioma patients[2,3], and new treatments have been encumbered by limited understanding of meningioma biology. DNA methylation profiling provides robust classification of brain tumors[4], but has not informed new treatments for patients.

Meningiomas are comprised of 3 DNA methylation groups

To identify biologic drivers and therapeutic vulnerabilities underlying meningiomas, DNA methylation profiling was performed on 565 meningiomas from patients with comprehensive clinical follow-up who were treated at 2 independent institutions from 1991 to 2019 (**Table 2.1**). Consistent with typical meningioma outcomes, local freedom from recurrence (LFFR) and overall survival (OS) were worse with higher World Health Organization (WHO) grade, recurrent presentation, or subtotal resection (**Fig. S2.1**). Meningiomas were stratified into a 200-sample discovery cohort from the University of California San Francisco (median follow-up 6.3 years), and a consecutive 365-sample validation cohort from The University of Hong Kong (median follow-up 5.3 years) (**Table 2.1**). Prior meningioma DNA methylation studies variably reported 2 to 6 groups of tumors[5–9], often with overlapping clinical outcomes[5], and questions remain regarding the biologic significance of meningioma DNA methylation grouping. Moreover, meningiomas

have an abundance of genomic copy number variants (CNVs)[8,10] (**Fig. 2.1a**), and prior studies neither accounted for confounding artifacts from CNVs[11], nor provided mechanistic or functional validation of the groups reported. Thus, opportunities exist to determine if DNA methylation profiles encode biologic information informing new treatments for meningioma patients, particularly through bioinformatic techniques clarifying DNA methylation groups in the context of CNVs, and mechanistic and functional studies to define biologic drivers.

Unsupervised hierarchical clustering of DNA methylation profiles, controlled for artifacts from CNVs using the SeSAMe preprocessing pipeline[11], revealed 3 meningioma DNA methylation groups in the discovery cohort (**Fig. 2.1b**). K-means consensus clustering validated 3 groups as the optimal number in the discovery and validation cohorts (**Fig. S2.2a**). A multi-class support vector machine classifier was constructed to assign meningiomas from the validation cohort into DNA methylation groups (**Fig. 2.2b**). Kaplan-Meier analyses showed DNA methylation groups were distinguished by differences in LFFR and OS (**Fig. 2.1c and S2.3a**), and correlated with WHO grade, sex, prior radiotherapy, and location (**Fig. 2.1d and S2.3b**). Nevertheless, DNA methylation groups were independently prognostic for LFFR on Kaplan-Meier analysis across WHO grades (**Fig. S2.3c, d**), and on multivariable regression (**Fig. 2.1e and S2.3e**).

Meningioma DNA methylation groups had CNVs affecting up to 80% of tumor genomes (**Fig. S2.4a, b**), but CNV profiles were independent from DNA methylation groups (**Fig. 2.4c**). Reanalysis using the minfi preprocessing pipeline[12], which does not control for CNV artifacts, reassigned 21% of meningiomas across poorly distinguished DNA methylation groups with overlapping clinical outcomes (**Fig. S2.5**). Thus, controlling

11

for CNV artifacts improves meningioma DNA methylation grouping and discrimination of meningioma outcomes.

Merlin drives meningioma apoptosis

Meningiomas are common in patients with neurofibromatosis type 2, a complex autosomal syndrome caused by loss of *NF2* on chromosome 22q, which encodes the tumor suppressor Merlin[13]. *NF2* is also the most recurrently mutated gene in sporadic and radiation-induced meningiomas[14–18]. Defining CNVs from DNA methylation profiles revealed *NF2* losses in 86% of syndromic (n=18) and radiation-induced meningiomas (n=34), which were predominantly found in DNA methylation groups with intermediate or poor outcomes (96%). Only 17% of meningiomas in the DNA methylation group with the best outcomes had *NF2* copy number losses (**Fig. 2.2a**), and RNA sequencing of 200 meningiomas from the discovery cohort confirmed higher *NF2* expression in this group compared to others (**Fig. 2.2b**). The combined distribution of *NF2* CNVs and somatic short variants from DNA amplicon sequencing of 65 meningiomas showed 89% of tumors in the DNA methylation group with the best outcomes encoded at least 1 wildtype copy of *NF2* (**Fig. S2.6a and Table 2.2**). Moreover, a comparison of meningiomas with loss of at least 1 copy of *NF2* revealed Merlin was only expressed in the DNA methylation group with the best outcomes (**Fig. 2.2c**).

NF2 variants are mutually exclusive from *TRAF7* somatic short variants in meningiomas[14,16,19], and *TRAF7* variants were enriched in Merlin-intact meningiomas compared to other DNA methylation groups (**Table 2.3**). Many Merlin-intact meningiomas did not encode *TRAF7* variants (79%), suggesting the DNA methylation group with the

best outcomes may not be unified by a single genetic driver. Indeed, meningioma histologic subtypes associated with $AKT1^{E17K}$ variants were also enriched in Merlin-intact meningiomas compared to tumors from other DNA methylation groups[20] (**Table 2.3**). Further, analysis of matched exome sequencing and DNA methylation profiling on 53 meningiomas revealed no solitary *TRAF7*, *AKT1*, *KLF4*, or other somatic short variants associated with favorable outcomes[5,16,20,21] in DNA methylation groups with intermediate or poor outcomes (**Table 2.4**).

Merlin has myriad tumor suppressor functions in schwannoma cells[22–24], but Merlin tumor suppressor functions in meningiomas are incompletely understood. M10G and IOMM-Lee meningioma cells express Merlin[25,26], and Merlin suppression increased meningioma cell proliferation (**Fig. S2.6b-f**). To identify gene expression programs underlying Merlin tumor suppressor functions in meningioma cells, RNA sequencing was performed on triplicate M10G cultures stably expressing the CRISPR interference (CRISPRi) components dCas9-KRAB[27,28] and either non-targeting control sgRNA (sgNTC), sgRNA suppressing *NF2* (sg*NF2*), or sg*NF2* with *NF2* rescue (**Fig. S2.6c**). Differential expression and ontology analyses revealed Merlin induced pro-apoptotic interferon regulatory factor (IRF) pathways previously unassociated with either Merlin or meningiomas (**Fig. S2.6g, h and Table 2.5**). Merlin suppression also blocked IRF target gene expression in MSC1 cells[25] (**Fig. S2.6i, j**), whose DNA methylation profiles classified with Merlin-intact meningiomas. Thus, to determine if Merlin regulates meningioma cell apoptosis, MSC1, M10G$^{dCas9-KRAB}$, and IOMM-Lee cultures were treated with the chemotherapy actinomycin D, revealing Merlin suppression reduced apoptosis (**Fig. 2.2d and S2.6k-m**). To define the relevance of this mechanism *in vivo*, CH-157MN

13

meningioma cells, which do not express Merlin[29], were grown as xenografts harboring an inducible Merlin construct. Merlin rescue in CH-157MN xenografts increased apoptosis in response to ionizing radiation compared to meningiomas lacking Merlin (**Fig. 2.2e and S2.6n**)

Merlin regulates protein degradation to control schwannoma cell proliferation[24], but Merlin suppression did not alter IRF stability or subcellular localization in meningioma cells (**Fig. S2.6o**). To elucidate if Merlin regulates IRF activity to control meningioma apoptosis, Merlin constructs encoding APEX tags were expressed in meningioma cells for proximity-labeling proteomic mass spectrometry[30] (**Table 2.6**). ARHGAP35, a DNA binding factor that inhibits glucocorticoid receptor expression[31,32], was detected in proximity to wild-type Merlin, but not Merlin[L46R], a missense variant associated with neurofibromatosis type 2[24] (**Fig. S2.6p**). Glucocorticoid signaling inhibits IRF activity to prevent apoptosis[33,34], and immunoprecipitation of Merlin from meningioma cells validated Merlin interaction with ARHGAP35 (**Fig. 2.2f**). IRF proteins were not detected in proximity to Merlin[APEX] constructs (**Table 2.6**), or in Merlin immunoprecipitates (**Fig. S2.6q**), suggesting Merlin indirectly regulates IRF activity via ARHGAP35. In support of this hypothesis, *NF2* suppression in meningioma cells induced glucocorticoid receptor expression, which was inhibited by *NF2* rescue (**Fig. 2.2g**). Further, glucocorticoid receptor suppression in meningioma cells lacking *NF2* rescued meningioma cell apoptosis (**Fig. 2.2h and S2.6r**), and glucocorticoid receptor expression was increased in human meningiomas with loss of *NF2* compared to euploid tumors (**Fig. 2.2i**). In sum, these data shed light on a novel pro-apoptotic tumor suppressor function of Merlin via regulation of glucocorticoid signaling in meningiomas (**Fig. 2.2j**).

14

Meningioma immune enrichment is associated with *HLA* expression and lymphatic vessels

Meningiomas in the DNA methylation group with intermediate outcomes had fewer CNVs than other groups (**Fig. S2.4a, b**), and clustered with non-tumor DNA methylation profiles from meningioma patients (**Fig. S2.7a**), suggesting bulk bioinformatic analyses of meningiomas in this group may be influenced by non-tumor cells in the meningioma microenvironment. In support of this hypothesis, meningioma DNA methylation probe clusters identified generic intercellular mechanisms regulating tissue development and homeostasis that were not organized into specific or cohesive biochemical mechanisms (**Fig. 2.1b and Table 2.7**). SeSAMe cell-type deconvolution of DNA methylation profiles showed immune cell enrichment in the meningioma DNA methylation group with intermediate outcomes compared to other groups (**Fig. 2.3a**). xCell RNA sequencing deconvolution and PAMES tumor purity analysis validated these findings[35,36] (**Fig. S2.7b-e**). Further, differential expression and gene ontology analyses showed enrichment of immune genes in the meningioma DNA methylation group with intermediate outcomes (**Fig. S2.7f and Table 2.8**), and immunohistochemistry revealed T cell enrichment compared to tumors from other groups (**Fig. 2.3b**).

To define meningioma cell types, single-cell RNA sequencing was performed on 57,114 cells from 8 meningioma samples representing each DNA methylation group (**Fig. 2.3c and S2.8**). Reduced dimensionality clusters of meningioma and non-meningioma cells were distinguished by chromosome 22q loss using CONICSmat[37] (**Fig. S2.9a**). Non-meningioma cell clusters with intact chromosome 22q were classified by expression of immune, neural, or vascular marker genes (**Fig. S2.9b, c and Table 2.9**). Meningioma

15

cell clusters with chromosome 22q loss were distinguished by differentially expressed cellular pathways (**Fig. S2.8c, S2.9b, S2.9c and Table 2.9**). Single-cell transcriptomes revealed more immune cells in Immune-enriched meningiomas compared to tumors from other groups (**Fig. 2.3d**). Further, analysis of DNA methylation profiles on 86 spatially distinct samples from 13 meningiomas revealed 92% of samples classified in concordance with the consensus DNA methylation group of each tumor[25] (**Fig. S2.10a**). Thus, meningioma DNA methylation grouping is not confounded by intratumor heterogeneity or sampling bias, suggesting coordinated genetic mechanisms may underlie meningioma immune infiltration.

HLA loss on chromosome 6p can decrease immune infiltration in cancer[38], and 88% of losses at the *HLA* locus were found in non-Immune-enriched meningiomas (**Fig. 2.3e**). Controlling for DNA methylation artifacts from CNVs was essential for this finding, as SeSAMe masked 48.4% of β values across 206 CpG probes associated with *HLA* genes in meningiomas, and analysis of matched whole exome sequencing and DNA methylation profiling revealed no instances of *HLA* loss of heterozygosity in Immune-enriched meningiomas[8] (**Fig. S2.10b**). *HLA* loss correlated with decreased *HLA* expression in meningiomas (**Fig. S2.10c**), and Immune-enriched meningiomas had increased *HLA* expression compared to tumors from other DNA methylation groups (**Fig. S2.10d**). Single-cell transcriptomes confirmed increased *HLA* expression in Immune-enriched meningioma cells compared to meningioma cells from other groups (**Fig. 2.3f**), suggesting *HLA* differences across DNA methylation groups were not confounded by non-tumor cells.

To identify additional mechanisms underlying Immune-enriched meningiomas, reference transcriptomic signatures of meningioma single-cell clusters were used to estimate proportions of meningioma cell types across DNA methylation groups. Meningioma cells expressing extracellular matrix remodeling genes were enriched in Immune-enriched meningiomas compared to tumors from other DNA methylation groups (**Fig. 2.3g**), and changes in the extracellular matrix can create a permissive microenvironment for lymphatic vessel formation[39–42]. Meningeal lymphatics near dural venous sinuses are necessary for central nervous system immune surveillance[43–47], but associations between lymphatic vessels and meningiomas have not been previously reported. Preoperative magnetic resonance imaging showed meningiomas from multiple DNA methylation groups were likely to involve dural venous sinuses (**Fig. S2.10e, f**), suggesting meningioma location might be necessary but not sufficient for immune infiltration. Compared to tumors from other DNA methylation groups, Immune-enriched meningiomas had hypomethylation and increased expression of meningeal lymphatic genes such as *LYVE1*, *CCL21*, and *CD3E*[46,48–50] (**Fig. 2.3h and S2.10g, h**). Immunofluorescence confirmed lymphatic enrichment in Immune-enriched meningiomas compared to tumors from other groups (**Fig. 2.3i**), and also in CH-157MN xenografts (**Fig. S2.10i**), whose DNA methylation profiles classified with Immune-enriched meningiomas. Thus, *HLA* expression and lymphatic vessels distinguish a novel DNA methylation group of Immune-enriched meningiomas.

Convergent genetic mechanisms misactivate the cell cycle in meningioma

High-grade meningiomas are defined by brisk cell proliferation leading to local recurrence and death in 50-90% of patients[51,52]. Cell proliferation was highest in the meningioma DNA methylation group with the worst outcomes (**Fig. 2.4a**), but deconvolution using single-cell reference transcriptomic signatures revealed similar proportions of cycling G2M phase meningioma cells in both Immune-enriched and Hypermitotic meningiomas (**Fig. 2.4b**). Thus, meningioma cell proliferation cannot explain the biologic differences among DNA methylation groups. RNA sequencing, gene ontology analysis, and immunohistochemistry showed FOXM1 and the FOXM1 transcriptional program were enriched in Hypermitotic meningiomas compared to tumors from other groups (**Fig. 2.4c, S2.11a, and Table 2.8**), and correlated with meningioma cell proliferation (**Fig. S2.11b, c**). FOXM1 drives meningioma cell proliferation and is a biomarker for meningioma recurrence, and putative FOXM1 target genes are accessible in the chromatin of meningioma DNA methylation groups with adverse clinical outcomes[8,9,53,54]. However, many FOXM1 targets are also induced by other cell cycle regulators, such as E2F1[55], and the FOXM1 gene expression program in meningiomas is incompletely understood.

To determine if the FOXM1 gene expression program was specifically misactivated in Hypermitotic meningiomas, FOXM1 and E2F1 target genes was studied across meningioma DNA methylation groups. FOXM1 targets nonoverlapping with E2F1 targets were enriched in Hypermitotic meningiomas compared to tumors from other groups (**Fig. S2.11d**), but E2F1 targets nonoverlapping with FOXM1 targets did not distinguish meningioma DNA methylation groups (**Fig. S2.12**). To elucidate the function of FOXM1

target genes in meningiomas, differentially expressed genes with FOXM1 binding motifs were analyzed across 25 meningiomas with matched RNA sequencing, H3K27ac ChIP sequencing, and DNA methylation profiling[56]. FOXM1 targets regulated the cell cycle, tumor metabolism, and the DNA damage response (**Fig. S2.13a**), suggesting FOXM1 may underlie meningioma resistance to cytotoxic therapies. In support of this hypothesis, FOXM1 protein increased in response to meningioma cell apoptosis (**Fig. S2.13b**), and over-expression of FOXM1 increased meningioma cell resistance (**Fig. S2.13c, d**).

Differential expression of enhancers and super-enhancers revealed Hypermitotic meningiomas were dominated by epigenetic mechanisms and transcription factors, such as FOXM1, that are impractical pharmacologic targets (**Fig. S2.14**). Further, druggable somatic short variants in meningiomas are rare, and are not associated with adverse clinical outcomes[10,13–17,19,20,53,57–60], with infrequent exceptions[61–64]. There were more CNVs in Hypermitotic meningiomas compared to other DNA methylation groups (**Fig. S2.4a, b**), and chromosome instability drives cancer evolution and response to therapy[65–67]. Thus, CNVs contributing to cell cycle misactivation may harbor therapeutic vulnerabilities that could inform new treatments for meningioma patients.

Loss of the endogenous CDK4/6 inhibitor *CDKN2A/B* on chromosome 9p is associated with worse outcomes in brain tumors[68], including meningiomas[64]. CNVs deleting the *CDKN2A/B* locus were enriched in Hypermitotic meningiomas (62%), and were associated with worse LFFR (**Fig. 2.4d and S2.15a**). *CDKN2A/B* methylation is an alternate mechanism of cell cycle misactivation in cancer[69,70], and *CDKN2A/B* was hypermethylated in Hypermitotic meningiomas compared to other groups (**Fig. 2.4e**). Stable suppression of *CDKN2A* or *CDKN2B* increased M10G$^{dCas9-KRAB}$ cell proliferation

(**Fig. S2.15b, c**), and re-classified M10G$^{dCas9-KRAB}$ DNA methylation profiles from Immune-enriched to Hypermitotic (**Fig. 2.4f**). Nevertheless, many Hypermitotic meningiomas retained *CDKN2A/B* (85%) (**Fig. 2.4d**), unsupervised hierarchical clustering of meningioma transcriptomes was unable to distinguish DNA methylation groups (**Fig. S2.16**), and the FOXM1 transcriptional program was not enriched in all Hypermitotic meningiomas (**Fig. S2.11d**). Thus, multiple mechanisms may drive the meningioma DNA methylation group with the worst clinical outcomes.

To identify additional mechanisms driving Hypermitotic meningiomas, enriched transcription factor binding motifs were intersected with H3K27ac ChIP sequencing troughs, revealing the poorly understood transcription factor USF1 may be bound to the *CDK6* promoter in meningiomas (**Fig. S2.17a and Table 2.10**). CNVs amplifying the *USF1* locus on chromosome 1q were enriched in Hypermitotic meningiomas (88%), and were associated with worse LFFR (**Fig. 2.4g and S2.17b**). Moreover, USF1 bound and activated the *CDK6* promoter in meningioma cells (**Fig. 2.4h, i and S2.17c, d**), and over-expression of USF1 increased meningioma cell proliferation (**Fig. 4j and S2.17e**). Thus, convergent genetic mechanisms misactivate the cell cycle in meningiomas.

Clinical translation of meningioma DNA methylation groups

Merlin regulation of glucocorticoid signaling drives meningioma apoptosis (**Fig. 2.2j**), and Merlin-intact meningiomas have the best clinical outcomes with current therapies (**Fig. 2.5a**). Immune-enriched and Hypermitotic meningiomas have adverse outcomes (**Fig. 2.5a**), exist along a continuum of cell cycle misactivation (**Fig. 2.4a, b**), and are resistant to cytotoxic therapies due to loss of Merlin (**Fig. 2.2j**) or misactivation of

FOXM1 (**Fig. S2.13**). The conjunction of mechanisms driving cytotoxic resistance or cell cycle misactivation suggests cytostatic cell cycle inhibitors may be effective treatments for meningiomas with adverse outcomes. To test this, the clinical CDK4/6 inhibitors abemaciclib, palbociclib, and ribociclib were studied in cell culture, organoids, and xenografts using Immune-enriched and Hypermitotic meningioma cells (**Fig. 2.5a**). CDK4/6 inhibitors blocked clonogenic growth of meningioma cells (**Fig. S2.18a**), but suppression of *CDKN2A* or *CDKN2B*, or over-expression of *USF1*, increased the efficacy of treatment (**Fig. S2.18b, c**). To test this therapeutic strategy in the context of a tumor microenvironment, meningioma cells were co-cultured with cerebral organoids comprised of pre-differentiated human pluripotent stem-cell derived astrocytes. This model recapitulates intratumor heterogeneity in meningioma cells[25], and intratumor heterogeneity drives cancer resistance to therapy[71]. Nevertheless, CDK4/6 inhibition attenuated meningioma cell growth in organoid co-culture (**Fig. S2.18d**). To define the pharmacodynamics and efficacy of this strategy for meningiomas *in vivo*, CH-157MN xenografts were treated with CDK4/6 inhibitors, which decreased RB phosphorylation (**Fig. S2.18e**), inhibited cell proliferation (**Fig. S2.18f**), attenuated xenograft growth (**Fig. 2.5b**), and prolonged survival (**Fig. 2.5c**).

These data provide preclinical rationale to treat patients with Immune-enriched or Hypermitotic meningiomas with cell cycle inhibitors, which achieve therapeutic doses in human meningiomas[72]. In support of our preclinical investigations, we have observed encouraging early results with compassionate use of CDK4/6 inhibitors in patients with meningiomas that were resistant to surgery and radiotherapy (**Fig. 2.5d and S2.19**). Clinical trials to establish the efficacy of this and other molecular therapies for

meningiomas will require rigorous patient selection and biologic stratification. In anticipation, we developed nomograms demonstrating DNA methylation groups provide superior discrimination of meningioma outcomes compared to CNVs or clinical variables[73] (**Fig. 2.5e and S20**).

Discussion

DNA methylation profiling is a powerful tool for biologic discovery, but clinical adoption of this technique has been encumbered by a lack of medical indications. The data presented here demonstrate an urgent need for clinical DNA methylation profiling to stratify meningioma patients for molecular therapies. Integrating genetic, epigenetic, transcriptomic, biochemical, and single-cell approaches, we find meningiomas are comprised of 3 DNA methylation groups with distinct clinical outcomes and biological drivers (**Fig. 2.5a**). We validate our results using mechanistic and functional studies in cells, organoids, xenografts, and patients to elucidate novel mechanisms underlying the most common primary intracranial tumor.

Controlling for DNA methylation artifacts from CNVs was essential for these discoveries. Meningioma DNA methylation analysis uncontrolled for CNV artifacts failed to identify robust groups (**Fig. S2.5b**), or groups with nonoverlapping differences in clinical outcomes, *NF2* loss, immune enrichment, and cell proliferation (**Fig. S2.5c, S21**). Quantifying the signal-to-noise ratio (SNR) of *NF2* loss across 3 meningioma DNA methylation groups, we found an SNR of 5.57 for SeSAMe groups compared to 2.25 for minfi groups. Although DNA methylation analysis uncontrolled for CNV artifacts provides robust classification across brain tumor types[4], meningiomas have significant

22

chromosome instability (**Fig. 2.1a and S2.4a, b**), and meningioma DNA methylation groups uncontrolled for CNV artifacts are variable across institutions and have uncertain biologic drivers[5–9]. We show controlling for DNA methylation artifacts from CNVs is necessary to identify robust groups of meningiomas with unifying biologic drivers. Our bioinformatic approach, integrated with mechanistic and functional studies, represents a significant conceptual advance for meningiomas, and may reveal biologic drivers and therapeutic vulnerabilities in other cancers with chromosome instability.

Effective treatments for meningioma patients have not changed in more than half a century, but new therapies are under investigation[2]. Our mechanistic and functional studies validate the first biomarker-based treatment for meningiomas with adverse clinical outcomes. We also find T cells in the meningioma microenvironment display multiple markers of immune exhaustion[74] (**Fig. S2.22**), suggesting immune checkpoint inhibition may be ineffective for meningiomas as monotherapy. These data also shed light on why meningioma immune infiltration does not correlate with better clinical outcomes, as it does in other cancers[75]. Thus, we encourage careful consideration of meningioma DNA methylation groups in the context of mechanistic and functional studies, and WHO grade, when stratifying meningioma patients for new treatments. Indeed, DNA methylation grouping does not obviate the importance of meningioma grading (**Fig. S2.3e**). These complementary systems provide independent information about meningioma outcomes (**Fig. 2.1e**), but unlike WHO grade, the meningioma DNA methylation groups we report reveal novel biologic drivers and therapeutic vulnerabilities informing new treatments for meningioma patients.

Acknowledgements

Data availability

DNA methylation, RNA sequencing, and exome sequencing data supporting the findings of this study will be deposited in the NCBI Gene Expression Omnibus. Single cell RNA sequencing data will be deposited in the Sequence Read Archive. The remaining data are available in the Article, Extended Data, or from the corresponding authors upon request.

Code availability

This manuscript contains no custom code or mathematical algorithms. A full description of the open-source code used to collect the data in this study (including, but

not limited to, HISAT2, DESeq2, R package, and FASTQC), as well as the version of each program, is available in the Methods section.

Methods

Meningiomas and clinical data

This study was approved by the UCSF Institutional Review Board (IRB #17-22324, #17-23196, and #18-24633). Meningioma samples for the discovery cohort were selected from the UCSF Brain Tumor Center Biorepository and Pathology Core in 2017, with an emphasis on high-grade meningiomas and low-grade meningiomas with long clinical follow-up. All WHO grade 2 and grade 3 meningiomas with available frozen samples were included. For WHO grade 1 meningiomas, frozen samples in the tissue bank were cross-referenced for clinical follow-up data from a retrospective institutional meningioma clinical outcomes database (IRB #13-12587), and all cases with available frozen tissue and clinical follow-up greater than 10 years (n=40) were included. To achieve a discovery cohort of 200 cases, additional WHO grade 1 meningiomas with available frozen tissue and the longest possible clinical follow-up (albeit less than 10 years, n=47) were included. The electronic medical record was reviewed for all patients in late 2018, and paper charts were reviewed in early 2019 for patients treated prior to the advent of the electronic medical record. All available clinical pathology material was reviewed for diagnostic accuracy by a board-certified neuropathologist (D.A.S.). WHO grading was performed using contemporary criteria outlined in the most recent edition of the WHO classification of tumors of the central nervous system[76]. Cases for which other tumors remained in the differential diagnosis (such as schwannoma or solitary fibrous

tumor/hemangiopericytoma) were excluded. The validation cohort was comprised of 365 consecutive meningiomas from patients who were treated at The University of Hong Kong (HKU) from 2000 (the year of the most recent WHO update in meningioma classification) to 2019 that had frozen tissue suitable for DNA methylation profiling. The medical record was reviewed for all patients in late 2019. For the discovery and validation cohorts, meningioma recurrence was defined as new radiographic tumor on magnetic resonance imaging after gross total resection, or enlargement/progression/growth of residual tumor on magnetic resonance imaging after subtotal resection. All magnetic resonance imaging studies in the discovery cohort were reviewed for accuracy by a board-certified radiologist with a Certificate of Added Qualification in Neuroradiology (J.E.V-M.).

Nucleic acid extraction

Frozen meningiomas were mechanically lysed using a TissueLyser II (QIAGEN) according to the manufacturer's instructions. DNA and RNA were extracted from lysed tissue using the AllPrep DNA/RNA/miRNA Universal Kit (#80224, QIAGEN). DNA and RNA quality were initially assessed using a NanoDrop One (Thermo Fisher Scientific). DNA samples with 260/280 values less than 1.8 or 260/230 values less than 1.6 were cleaned using ethanol precipitation and re-assessed. RNA samples with 260/280 values less than 1.8 or 260/230 values less than 1.6 were cleaned using the RNA Cleanup protocol from the RNeasy Mini Kit (#74106, QIAGEN). RNA samples were analyzed on a Bioanalyzer 2100 using the RNA 6000 Nano Kit (#5067-1511, Agilent Technologies). Only meningioma samples with high-quality DNA (260/280 greater than 1.8 and 260/230 greater than 1.6) and high-quality RNA (RIN greater than 8) were used for DNA

methylation profiling and RNA sequencing. After quality control, the discovery cohort was comprised of 200 meningiomas from patients who were treated at UCSF from 1991 to 2016 (median clinical follow-up 6.3 years), and the validation cohort was comprised of 365 consecutive meningiomas from patients who were treated at HKU from 2000 to 2019 (median clinical follow-up 5.3 years).

DNA methylation profiling and analysis

Genomic DNA was processed on the Illumina Methylation EPIC Beadchip (#WG-317-1003, Illumina) according to manufacturer's instructions at the Molecular Genomics Core at the University of Southern California. Downstream analysis was performed in R version 3.5.3 with SeSAMe[11].

Probes were filtered and analyzed using the standard SeSAMe preprocessing pipeline, including normal-exponential out-of-band background correction, nonlinear dye bias correction, p-value with out-of-band array hybridization masking, and β value calculation (β = methylated/[methylated+unmethylated]). A total of 272,041 probes were masked in at least one sample by the SeSAMe preprocessing pipeline, and 593,877 were retained for subsequent analysis.

Pre-processing and β value calculation were repeated using the minfi R package for comparison[12], using functional normalization[77]. Probes were filtered based on the following criteria: (i) removal of probes containing common single nucleotide polymorphisms (SNPs) within the targeted CpG sites or on an adjacent base pair (n=30,435), (ii) removal of probes targeting the X and Y chromosomes (n=19,298), (iii) removal of cross-reactive probes previously reported in the literature[78] (n=39,605), and

(iv) removal of probes with a detection p>0.05 in any samples (n=12,572). A total of 763,949 probes were retained for analysis after minfi pre-processing, representing 31.4% more probes than were included for analysis using the SeSAMe preprocessing pipeline.

Principal component analysis on the β values from both pre-processing pipelines was performed in R using the base command 'prcomp' with the parameters 'center = TRUE, scale. = FALSE'. Variable probes were identified from the first 3 principal components, and the top 700 probes from each principal component (2,100 total probes) were selected for analysis by ranking the absolute gene loading score values within principal components. Duplicate probes were removed, and the probes with the lowest gene loading scores were culled until 2,000 variable probes remained, which were used for unsupervised hierarchical clustering (Pearson correlation distance, Ward's method).

Sampling distributions of DNA methylation group proportions were generated via bootstrapping. In brief, the population size of the discovery cohort was sampled with replacement 100 times, and the proportion of meningiomas in each DNA methylation group was calculated for each sampling. K-means consensus clustering was performed to determine the optimal number of clusters using the ConsensusClusterPlus R package[79], subsampling 1000 times per cluster number and using all 2,000 probes and 80% of samples per subsample. SeSAMe consensus clustering clearly identified 3 robust clusters as the optimal number, while minfi consensus clustering was unable to discriminate between 3 and 4 clusters. Even within 3 groups, minfi re-assigned 21% of meningiomas to different DNA methylation groups compared to the SeSAMe preprocessing pipeline. To quantify differences in SeSAMe and mini preprocessing pipelines, we calculate a signal-to-noise ratio (SNR) using *NF2* copy number status

28

across meningioma DNA methylation groups. For the SNR calculation in the 3 SeSAMe meningioma DNA methylation groups, signal = (*NF2* intact in Merlin-intact meningiomas) + (*NF2* loss in non-Merlin-intact meningiomas) and noise = (*NF2* loss in Merlin-intact meningiomas) + (*NF2* intact in non-Merlin-intact meningiomas). In the 3 minfi meningioma DNA methylation groups, we calculated a SNR three times, assuming each group was Merlin-intact in turn, and the most favorable minifi SNR was reported, which remained worse than the SNR for SeSAMe meningioma DNA methylation groups.

A methylation profile multi-class support vector machine (SVM) classifier was generated using the caret R package. In brief, a linear kernel SVM was constructed using training data comprising 75% of randomly selected samples from the discovery cohort (n=200) with 10-fold cross validation. 2,000 probes from each pre-processing pipeline were used as variables. As a sanity check, the remaining 25% of samples from the validation cohort were used to test the model, which performed with 97.9% accuracy when classifying samples into 3 SeSAMe groups (95% CI 89.2-99.9%, $p<2.2 \times 10^{-16}$). Classifiers for 3, 4, 5, or 6 minfi groups performed with 91.8% (95% CI 80.4%-97.7%, $p=4.69 \times 10^{-9}$), 91.8% (95% CI 80.4%-97.7%, $p=9.58 \times 10^{-16}$), 93.8% (95% CI 82.8%-98.7%, $p=2.98 \times 10^{-16}$), and 93.6% (95% CI 82.5%-98.7%, $p<2.2 \times 10^{-16}$) accuracy, respectively.

DNA methylation profiles from representative meningiomas and meningioma cell lines were compared in reduced dimensionality space using the Rtsne R package. A matrix of the samples and their β values for the 2,000 variable probes were used as input and the 'Rtsne' command was run with the parameters 'pca=F, normalize=F, perplexity=3.'

Leukocyte percentage within the tumor samples was calculated from DNA methylation using the 'estimateLeukocyte' command within the SeSAMe R package[11]. In brief, the intensity of DNA methylation probes uniquely hyper- or hypo-methylated in leukocytes were used to estimate the leukocyte percentage. Tumor purity was estimated from DNA methylation profiles using the PAMES R package[36]. To generate cross-platform comparable DNA methylation profiles on meningiomas and normal tissue samples from meningioma patients (muscle or fat), β values of adjacent CpG sites were combined and the sites were reduced to genomic regions, with a minimum of 3 CpG sites per region. Methylation status of genomic regions was used to compute the Area Under the Curve (AUC) to define the segregation between tumor and normal samples. Hypermethylated and hypomethylated genomic regions with the top 10 AUCs (20 regions in total) were selected for tumor purity estimation. These regions were completely methylated or unmethylated in normal tissue samples, but were partially methylated in meningiomas. The median of partial methylation across these regions in meningiomas was used to estimate tumor purity.

Copy number analysis

CNV profiles from methylation data were generated as previously described with the 'cnSegmentation' command within the SeSAMe R package[4], using the 'EPIC.5.normal' dataset from the sesameData package as a copy-number-normal control. CNV intensity value distributions were manually inspected for local minima and maxima, and nadirs separating copy number losses, gains, and neutral events were identified. Based on this analysis, segments with mean intensity values less than -0.1

were defined as copy number losses, segments with mean intensity values greater than 0.15 were defined as copy number gains, and segments with intensity values between -0.1 and 0.15 were defined as neutral copy number events. The percentage of the genome with copy number variation was determined by calculating the average number of segments per sample with mean intensity values less than -0.1 or greater than 0.15, weighted by segment length.

CNV profiles across meningioma DNA methylation groups were generated by sampling DNA methylation profiles every 30,000 genomic base pairs and determining the percentage of segments containing the sampled location that were lost or gained. Specific gene loci (*NF2*, *HLA*, *CDKN2A/B,* and *USF1*) were determined to be lost or gained if the entire locus was contained in a segment with mean intensity values less than -0.1 or greater than 0.15, respectively.

Chromosome arm-level CNVs were identified by calculating the percentage of each chromosomal arm containing segments with mean intensity values less than -0.1 or greater than 0.15. Chromosome arms with at least 80% of their length meeting these criteria were considered losses or gains of the chromosomal arm, respectively. This analysis excluded sex chromosomes and the p arms of acrocentric chromosomes, which had insufficient methylation probes for robust CNV quantification (13p, 14p, 15p, 21p, and 22p). To validate this approach, chromosomal losses and gains from DNA methylation profiles were compared to those from whole-exome sequencing of 25 previously described meningiomas overlapping with the discovery cohort[8], and to CNVs from *de novo* Clinical Laboratory Improvement Amendments (CLIA)-certified exome sequencing of 10 spatially distinct meningioma samples[25,80] (3 Merlin-intact, 15 Immune-enriched,

31

and 17 Hypermitotic meningiomas). To define CNVs from previously described meningioma whole exome sequences and from *de novo* CLIA-certified exome sequences, reads were aligned with the Burrows-Wheeler Aligner (BWA)[81], deduplicated using the Genome Analysis Toolkit (GATK)[82,83], and large-scale copy number alterations were called using CNVkit[84]. In support of our approach, CNVs were 99.12% concordant across research and clinical bioinformatic platforms using DNA methylation and exome sequences technologies.

Co-occurrence of chromosomal arm CNVs were visualized as an undirected weighted graph where nodes represented the frequency of CNV co-occurrences, and edges represented the frequency of co-occurrence between CNV pairs. The size of each node was linearly proportional to the sum of total co-occurrences with other CNVs, while the thickness of each edge was linearly proportional to the frequency of the co-occurrence pair with a frequency cutoff ≥5 for display. The igraph R package was used for graph visualization.

The interdependence of CNVs and meningioma DNA methylation groups was analyzed by identifying pairs of meningiomas with identical CNV profiles, and subsequently comparing the DNA methylation profile between meningioma pairs. This approach revealed 37% of meningioma pairs with identical CNVs were assigned to different DNA methylation groups, demonstrating meningioma CNV profiles were independent from meningioma DNA methylation groups.

RNA sequencing and analysis

Library preparation was performed using the TruSeq RNA Library Prep Kit v2 (#RS-122-2001, Illumina) and 50 bp single-end reads were sequenced on an Illumina HiSeq 4000 to a mean of 42 million reads per sample at the UCSF IHG Genomics Core. Quality control of FASTQ files was performed with FASTQC (https://www.bioinformatics.babraham.ac.uk/projects/fastqc/). Reads were trimmed with Trimmomatic to remove Illumina adapter sequences[85], leading and trailing bases with quality scores below 20, and any bases that did not have an average quality score of 20 within a sliding window of 4 bases. Any reads shorter than 36 bases after trimming were removed. Reads were mapped to the human reference genome GRCh38[86] using HISAT2[87] version 2.1.0 with default parameters. For downstream expression analysis, exon level count data were extracted from the mapped HISAT2 output using featureCounts[88].

Differential expression analysis was performed in R version 3.5.3 with DESeq2[89], using the 'apeglm' parameter[90] to calculate log fold changes and setting a false discovery rate of 0.05. Differentially expressed genes were identified as those with log fold changes greater than 1 and an adjusted p-value less than 0.05. Gene ontology analysis of differentially expressed genes was performed using Enrichr, and combined scores displayed represent z-score weighted p-values, which lack error bars[91,92]. Cell types within samples were deconvoluted using xCell with transcripts per million values[35]. In brief, the strength of gene expression patterns unique to different cell types were used to estimate the proportion of cell types within each meningioma.

The variance stabilizing transformation of the RNA sequencing counts were used to calculate variances for each gene across the 200 meningioma samples. The 2,000 most variable genes were used for unsupervised hierarchical clustering (Pearson correlation distance, Ward's method), which did not reveal any clear clusters of genes or meningiomas. Moreover, transcriptome clustering failed to recapitulate DNA methylation groups. FOXM1 and E2F1 transcription factor targets were identified from the ChIP-X Enrichment Analysis (CHEA) dataset within the Harmonizome[93].

Somatic short variant sequencing and analysis

A custom amplicon DNA sequencing panel was designed with 100% coverage of all coding exons of *NF2*. Genomic DNA was processed using this panel and the CleanPlex Target Enrichment and Library Preparation kit, following manufacturer's instructions (#PGD364, Paragon Genomics). Library quality was assessed on a TapeStation 4200 using the High Sensitivity D1000 Kit (#5067-5584, Agilent Technologies). 150 bp paired-end reads were sequenced on an Illumina MiSeq v2 Micro at the UCSF Center for Advanced Technology. Quality control of FASTQ files was performed with FASTQC[94]. Reads were mapped to the *NF2* locus using Bowtie2[95]. Somatic short variants (point mutations and small indels) were identified using the Genome Analysis Toolkit (GATK)[96]. The mapped Bowtie2 output was processed with recalibration of base confidence scores, and processed reads were used as input for HaplotypeCaller[82] with the parameters '-ERC none' and '--max-reads-per-alignment-start 0' to identify somatic variants. Somatic short variants were filtered for a minimum total depth of 100 reads. Filtered variants were annotated using SnpEff[97,98], and all but one

NF2 somatic short variant identified across DNA methylation groups were predicted to have 'HIGH' variant impact.

Single nucleotide variants in *TRAF7* were identified from the RNA sequencing data by following the Genome Analysis Toolkit's (GATK)[96] "RNAseq short variant discovery" Best Practices Workflow. In brief, the mapped HISAT output was processed by de-duplication and recalibration of base confidence scores. Processed reads were used as input for HaplotypeCaller[82] with the parameters '--dont-use-soft-clipped-bases true' and '-stand-call-conf 20' to identify somatic short variants. The 'VariantFiltration' command within GATK was used to further filter the identified variants with the parameters '-window 35 -cluster 3 --filter-name "FS" -filter "FS > 30.0" --filter-name "QD" -filter "QD < 2.0".' Filtered variants were annotated using SnpEff[97,98]. The same pipeline was attempted to identify somatic short variants in *PIK3CA*, *SMARCB1*, *SMO*, *KLF4*, *POLR2A*, *NF2*, and *AKT1*. Low coverage (average FPKM<10 across samples) excluded *PIK3CA*, *AKT1*, and *NF2* from further analysis. The small number of mutations (<10) detected in *SMARCB1*, *KLF4*, and *POLR2A* could not be distinguished from background error rates in RNA-sequencing. Finally, mutations identified in *SMO* were unlikely to be activating mutations[21], and were discordant from prior studies[14], likely to be spurious findings. Thus, only single nucleotide variants in *TRAF7* were reported.

To generalize our analysis of meningioma short somatic variants across DNA methylation groups, 53 meningiomas with matched exome sequencing and DNA methylation profiling were analyzed for recurrent variants enriched in meningiomas[5,16,53]. Samples included 43 previously described meningioma whole exomes[8,56], 25 of which overlapped with the discovery cohort, and 10 spatially distinct meningioma samples

35

analyzed *de novo* using CLIA-certified exome sequencing of 500 genes, including all recurrently mutated genes reported in meningiomas, such as *TRAF7, AKT1, SMO, KLF4, CDKN2A/B, TERT, SMARCB1, BAP1, SUFU, TP53, PTEN, MYC, PBRM1, and PIK3CA*[25,80] (6 Merlin-intact, 21 Immune-enriched, and 26 Hypermitotic meningiomas). Short somatic variants were defined as previously described[8,56,80]. In brief, whole exome sequences were aligned with the Burrows-Wheeler Aligner (BWA)[81] and analyzed using Picard tools and the Genome Analysis Toolkit (GATK), following GATK Best Practices[96].

Immunoblotting, subcellular fractionation, and immunoprecipitation

Immunoblot cell line samples were prepared by lysis in radioimmunoprecipitation assay (RIPA) buffer containing Complete-Mini EDTA-free protease inhibitor (#11836170001, Sigma-Aldrich) and PhosSTOP phosphatase inhibitor (#04906837001, Sigma-Aldrich), followed by boiling i Laemmli reducing buffer. Immunoblot meningioma samples were first mechanically lysed using a TissueLyser II (QIAGEN) according to the manufacturer's instructions then processed identically to cell line samples. Samples were separated on 4-15% gradient TGX precast gels (#4561086, Bio-Rad), and transferred onto nitrocellulose membranes (#1620094, Biorad). Membranes were blocked in 5% TBST-milk, incubated in primary antibody, washed, and incubated in secondary antibodies. Membranes were subjected to immunoblot analysis using Pierce ECL (#32209, Thermo Fischer Scientific) or SuperSignal West Femto (#34095, Thermo Fischer Scientific) substrates. Primary antibodies were used against Merlin (#ab88957, Abcam), GAPDH (#MA515738, Thermo Fischer Scientific), Caspase-7 (#9492, Cell Signaling), IRF8 (#5628S, Cell Signaling), Tubulin (#T5168, Sigma), HH3 (#702023,

Thermo Fischer Scientific), FLAG (#F1804, Sigma), ARHGAP35 (#2860S, Cell Signaling), FOXM1 (#sc-376471, Santa Cruz), CDK6 (#3136S, Cell Signaling), RB (#9309S, Cell Signaling), pRB-S780 (#8180P, Cell Signaling), and pRB-S807/811 (#8516P, Cell Signaling).

Subcellular fractionation kits were purchased from Thermo Fischer Scientific (#78833) and used according to manufacturer's instructions. In brief, M10G cells were seeded into 10cm plates, and trypsinised and lysed in Cytoplasmic Extraction Reagent I containing protease and phosphatase inhibitors after 2 days of growth. Lysis solution was incubated on ice for 10 minutes before addition of Cytoplasmic Extraction Reagent II and incubation for 1 minute. Cytoplasmic fractions were isolated via centrifugation for 5 minutes, 21,000x g, 4°C. The Nuclear pellet was resuspended in Nuclear Extraction Reagent containing protease and phosphatase inhibitors followed by incubation on ice for 40 minutes with intermittent vortexing. Finally, the nuclear fraction was isolated by centrifugation for 5 minutes, 21,000 x g, 4°C. Protein concentration was measured using Bradford Reagent (#5000205, Biorad), samples were normalized, and processed for immunoblotting or immunoprecipitation.

For whole cell lysate immunoprecipitation, samples were lysed in ice-cold Jies buffer (100mM NaCl$_2$, 20mM Tris HCl (pH7.5), 5mM MgCl$_2$, 0.5% NP40, protease and phosphatase inhibitors) before centrifugation at 4°C for 5 minutes, 21,000 x g. Protein concentration was measured using Bradford reagent and equal protein from each sample was loaded onto pre-washed FLAG M2 beads (#M8823, Sigma-Aldrich) before incubation at 4°C, overnight with gentle rotation. The following day, proteins was eluted from the

beads with Laemmli buffer and boiled for 5 minutes. Immunoblotting revealed IRF8 in cytoplasmic and nuclear fractions, and ARHGAP35 in cytoplasmic fractions.

Cell culture and organoids

HEK293T, BenMen[99], IOMM-Lee[26], and CH157-MN[29] cells were cultured in Dulbecco's Modified Eagle Medium (DMEM) (#11960069, Life Technologies), supplemented with 10% fetal bovine serum (FBS) (#16141, Life Technologies), 1X GlutaMAX (#35050-061, Thermo Fischer Scientific), and 1X Penicillin/Streptomycin (#15140122, Life Technologies). DI-98 and DI-134 cells[56] and cultured in DMEM supplemented with 7% FBS and 1X Penicillin/Streptomycin. M10G cells[25] were cultured in a 1:1 ratio of DMEM/F12 media (#10565, Life Technologies) and Neurobasal media (#21103, Life Technologies), supplemented with 5% FBS, B-27 supplement without vitamin A (#12587, Life Technologies), N-2 supplement (#17502, Life Technologies), 1X GlutaMAX (#35050, Life Technologies), 1mM NEAA (#11140, Life Technologies), 100U/mL Anti-Anti (#15240, Life Technologies), 20 ng/mL EGF (#AF-100-15, Peprotech), and 20 ng/mL FGF (#AF-100-18B, Peprotech). MSC1 cells were cultured in the same conditions as M10G cells, but supplemented with 15% FBS[25]. Human cerebral organoids were created from astrocytes induced from pluripotent human stem cells and co-cultured with meningioma cells as previously described[25].

Colorimetric proliferation assays were performed using the CellTiter 96 Non-Radioactive Cell Proliferation Assay (#G4100, Promega), according to manufacturer's instructions. For clonogenic assays, 150 cells were seeded in triplicate in 6 well plates. Cells were treated with either vehicle or drug both 1 and 6 days after seeding. After 10

total days of growth, cells were fixed in methanol for 30 minutes and stained with 0.01%

crystal violet (C6158, Sigma-Aldrich) for 1 hour. Plates were rinsed with water three times,

allowed to air dry, and imaged on a Zeiss Stemi 508 stereo microscope. Colony area was

quantified by measuring total image intensity using ImageJ, with normalization to

background intensity. Apoptosis assays were performed by treating cells with actinomycin

D (#11421, Caymen Chemicals) 0.5 µg/ml for 24 hours.

CRISPRi gene suppression

Lentiviral particles containing pMH0001[100] (UCOE-SFFV-dCas9-BFP-KRAB,

#85969, Addgene) were produced by transfecting HEK293T cells with standard

packaging vectors using the *Trans*IT-Lenti Transfection Reagent (#6605, Mirus). M10G

cells were stably transduced with lentiviral particles to generate M10G$^{dCas9-KRAB}$ cells.

Successfully transduced cells were isolated through selection of BFP positive cells using

fluorescence activated cell sorting on a Sony SH800.

Single-guide RNA (sgRNA) protospacer sequences were individually cloned into

the pCRISPRia-v2 vector[101] (#84832, Addgene), between the BstXI and BlpI sites, by

ligation. Each vector was verified by Sanger sequencing of the protospacer. Protospacer

sequences were sgNTC (GTGCACCCGGCTAGGACCGG), sg*NF2*

(GGACTCCGCGCGCCTCTCAG)*,* sg*USF1* (GAGATACCTAGGCCGGGAGA)*,*

sg*CDKN2A* (GTGGCCAGCCAGTCAGCCGA)*,* sg*CDKN2B*

(GACTCTGCCAGAGCGAGGCG). Lentivirus was generated as described above for

each sgRNA expression vector. M10G$^{dCas9-KRAB}$ cells were independently transduced with

lentivirus from each sgRNA expression vector, and selected to purity using 20 μg/mL puromycin over 7 days.

shRNA gene suppression

Lentiviral particles containing pLKO.1 shRNA targeting control (RHS6848, Dharmacon) or *NF2* (RHS3979-201768826 or RHS3979-201768830) were generated by transfecting HEK293T cells with standard packaging vectors (psPAX2 and pMD2.9) and shRNA plasmids using *Trans*IT-Lenti Transfection Reagent. After 48 hours of virus production, viral particles were sterilized through a 0.45 μM filter and added to meningioma cells with polybrene 10 μg/ml (TR-1003, MerkMillipore). A polyclonal population of shRNA positive cells was selected using puromycin 2 μg/ml.

siRNA gene suppression

Small interfering RNA (siRNA) targeting the glucocorticoid receptor, NR3C1 (#J-003424-10-0002), or control (#D-001810-01-05), were purchased from Dharmacon. siRNA transfection was performed using Lipofectamine RNAiMax reagent (#13778, Thermo Fischer Scientific). In brief, 2 cocktails containing either siRNA (25 nM) or Lipofectamine RNAiMax (3 μl) in 150 μl OptiMEM were made per transfection. Cocktails were incubated for 5 minutes prior to combination of the 2 solutions, followed by incubated for an additional 10 minutes before adding to cells for 15 hours. The siRNA transfection was repeated after 48 hours and expanded. Cells were harvested 92 hours after first siRNA transfection.

RNA extraction, cDNA synthesis, and quantitative reverse transcriptase PCR

RNA was extracted from cultured cells using the RNeasy Mini Kit (#74106, QIAGEN) according to manufacturer's instructions. cDNA was synthesized from extracted RNA using the iScript cDNA Synthesis Kit (#1708891, Bio-Rad). Real-time qPCR was performed using PowerUp SYBR Green Master Mix (#A25918, Thermo Fisher Scientific) on a QuantStudio 6 Flex Real Time PCR system (Life Technologies). Real-time QPCR primer sequences were GAPDH-F (5'-GTCTCCTCTGACTTCAACAGCG-3'), GAPDH-R (5'-ACCACCCTGTTGCTGTAGCCAA-3'), CDKN2A-F (5'-ATGGAGCCTTCGGCTGACT-3'), CDKN2A-R (5'-GTAACTATTCGGTGCGTTGGG-3'), CDKN2B-F (5'-ACGGAGTCAACCGTTTCGGGAG-3'), CDKN2B-R (5'-GGTCGGGTGAGAGTGGCAGG-3'), USF1-F (5'-CTGCTGTTGTTACTACCCAGG-3'), USF1-R (5'-TCTGACTTCGGGGAATAAGGG-3'), CDK6-F (5'-TCTTCATTCACACCGAGTAGTGC-3'), CDK6-R (5'-TGAGGTTAGAGCCATCTGGAAA-3'), NR3C1-F (5'-ATAGCTCTGTTCCAGACTCAACT-3'), and NR3C1-R (5'-TCCTGAAACCTGGTATTGCCT-3'). Real-time qPCR data were analyzed using the ΔΔCt method relative to *GAPDH* expression.

Immunofluorescence

Immunofluorescence of primary meningioma cells was performed on glass coverslips. Cells were fixed in 4% paraformaldehyde (#15710, Electron Microscopy Sciences), blocked in 2.5% BSA (#BP1600, Fischer Scientific) and 0.1% Triton X-100 (#X100, Sigma) in Phosphate Buffered Saline (PBS) for 30 min at room temperature (#14190, Gibco), and labeled with Ki-67 (#ab15580, Abcam) primary antibodies at room

temperature for 1 h. Cells were labeled with Alexa Fluor secondary antibodies and either Hoechst 33342 (#H3570, Thermo Fisher Scientific) or DAPI (#D3571, Thermo Fisher Scientific) to mark DNA for 1 h at room temperature, and were mounted in ProLong Diamond Antifade Mountant (#P36970, Thermo Fisher Scientific). For apoptosis assays, cells were washed in Annexin V binding buffer, stained with Annexin V for 15 min (#550911, BD Bioscience), washed, labeled with DAPI to mark DNA for 1 h at room temperature, and mounted in ProLong Diamond Antifade Mountant.

Immunofluorescence of human and xenograft meningiomas for lymphatic vessels was performed on 10 μm cryosections of frozen tissue embedded in OCT Compound (Thermo Fisher Scientific). Slides with tissue were fixed in cold acetone for 10 min, air dried, washed in PBS, permeabilized with 0.3% Triton-X 100 in PBS, and washed again in PBS. Sections were blocked (2% BSA, 1% donkey serum, and 0.1% Triton-X 100 in PBS) for 30 min. Sections were labeled with either LYVE-1 (#ab14917, Abcam) or PROX-1 (#AF2727, R&D Systems) primary antibodies at room temperature for 1 h. Slides were subsequently labeled with Alexa Fluor secondary antibodies and Hoechst 33342 to mark DNA for 1 h at room temperature, and were mounted in ProLong Diamond Antifade Mountant.

Dual immunofluorescence of human meningiomas for FOXM1 and Ki-67 was performed on 5 μm formalin-fixed, paraffin-embedded (FFPE) human meningioma sections. Following antigen retrieval using CC1 for 32 min (#950-124, Roche Diagnostics), sections were incubated and detected sequentially with rabbit monoclonal Ki-67 (#30-9, Roche Diagnostics) and rabbit monoclonal FOXM1 primary antibodies

(#EPR17379, Abcam). Each primary antibody incubation was 32 min and single stained controls were used to verify specificity.

Mice

This study was approved by the UCSF Institutional Animal Care and Use Committee (AN174769-03A), and all experiments complied with relevant ethical regulations. Xenograft experiments were performed by implanting 3 million CH-157MN cells into the flank of 5-6-week-old NU/NU mice (Harlan Sprague Dawley Inc.). To induce Merlin expression in meningiomas *in vivo*, mice harboring CH-157MN cells encoding pLV.APEX2-Merlin were treated with doxycycline 200 µg/ml or 1 mg/ml (#D9891, Sigma) 14 days post implantation. After 7 days of treatment, 2 Gy of ionizing radiation per day was delivered using a Precision X-RAD 320 Cabinet Irradiation, with normal operating settings, on each of 2 successive days. Tumors were collected 24 hours after the second dose of ionizing radiation for immunoblotting and immunohistochemistry. For preclinical pharmacologic experiments, animals in the treatment arm were gavaged with 100 µg/g abemaciclib in 0.5% methylcellulose vehicle daily starting 12 days after injection, until protocol-defined endpoints. For Kaplan-Meier survival analysis, events were recorded when tumors reached the protocol-defined size of 2000 mm^3.

Histology and immunohistochemistry

Deparaffinization and rehydration of 5 µm FFPE human and mouse meningioma tissue sections and hematoxylin and eosin staining were performed using standard procedures. Immunostaining was performed on an automated Ventana Discovery Ultra

staining system. Immunohistochemistry was performed on 5μm FFPE meningioma xenograft sections using rabbit monoclonal Ki-67 (#30-9, Roche Diagnostics) with primary antibody incubation for 16 min following CC1 antigen retrieval for 8 min, or rabbit monoclonal cleaved Caspase-3 (#5A1E, Cell Signaling) with primary antibody incubation for 32 min at 37°C following CC1 antigen retrieval for 8 min.

CD3 immunoreactivity (#A0452, Agilent Technologies) for each tumor was categorized qualitatively. Tumors were scored CD3 positive if multiple aggregates of CD3-positive lymphocytes were identified, and were otherwise scored as CD3 negative. FOXM1 labeling index was quantified based on the total amount of nuclei with strong immunoreactivity for FOXM1 within a 200x field. Ki-67 labeling index was quantified based on the total amount of nuclei with strong immunoreactivity for Ki-67 within a 200x field. The labeling index for both FOXM1 and Ki-67 was averaged across 2 200x fields for each meningioma.

Microscopy

Fluorescence microscopy was performed on a LSM 800 confocal laser scanning microscope with a PlanApo 20X air objective (Zeiss). Images were processed and quantified from representative regions of each tumor or coverslip using ImageJ. Histologic and immunohistochemical features were evaluated using light microscopy on an BX43 microscope with standard objectives (Olympus). Images were obtained and analyzed using the Olympus cellSens Standard Imaging Software package.

APEX proteomic proximity-labeling mass spectrometry and analysis

M10G cells encoding pLV.APEX2-Merlin wild type and L46R-mutant constructs were seeded onto 5 x 15 cm plates. For APEX labelling, cells were treated with 0.5 uM Biotin-phenol (#BT1015, Berry & Associates) and returned to 37°C, 5% CO_2 for 30 minutes. After 24 hours, Merlin protein expression was induced with $0.1\mu g/ml$ doxycycline. Biotin treated cells were subject to free radical formation by adding media containing 1mM H_2O_2 to cells for exactly 30 seconds, on ice. Immediately, H_2O_2 media was aspirated and the reaction was quenched (10mM Sodium Ascorbate, 1mM Azide, 5mM Trolox), and cells were pelleted.

To prepare cell pellets for biotin/streptavidin precipitation, samples were lysed in Urea buffer (8M urea, 0.1M Ammonium Bicarbonate pH8, 150mM NaCl, protease inhibitors and phosphatase inhibitors), sonicated for 1 minute followed by alkylation of free cysteines (10mM iodoacetamide). Trypsin digest (#V5073, Promega) was performed at 37°C for 20 hours with gentle rotation. Digested proteins were desalted through a 100mg Sep-Pak C18 vacuum cartridge (#WAT023590, Waters) and lyophilized in a speed vac. Lyophilised proteins were dissolved in IAP buffer (50 mM MOPS, 10 mM HNa2PO4, 50 mM NaCl, pH 7.5), sonicated for 30 minutes in a 4°C water bath and centrifuged to clear insoluble material. For biotin/streptavidin precipitation, 20 μl of washed anti-biotin beads (#ICP0615, Immunechem Pharmaceuticals) were incubated with each protein sample (2 hours, 4°C, gentle rotation), beads were washed and eluted in 0.15% trifluoroacetic acid, desalted on nest tips, and lyophilized prior to mass spectrometry.

Samples were resuspended in 4% formic acid, 4% acetonitrile solution, and separated by a reversed-phase gradient over a nanoflow column (360 μm O.D. x

75 μm I.D.) packed with 15 cm of 1.7 μm BEH C18 particles (#186002350, Waters). The HPLC buffers were 0.1% formic acid and 100% acetonitrile on 0.1% formic acid for buffer A and B respectively. The gradient was operated at 300 nL/min from 5 to 25% buffer B over 36 min, followed by a 25%-36%B over 42 min, a column wash at 95% B, with a total acquisition time of 90 min. Eluting peptides were analyzed in on a Orbitrap Fusion Lumos Tribrid Mass Spectrometer system (Thermo Fischer Scientific) equipped with a n1200 Easy-nLC 1200 high-pressure liquid chromatography system (Thermo Fischer Scientific). A data-dependent acquisition method was used with following parameters: 1 second cycle time, MS1 acquisition in the orbitrap with 350-1350 m/z range at 240K resolution and a 50 milisecond maximum injection time, MS2 analysis was performed with HCD fragmentation in the ion trap with 32% normalized collision energy, 200-1200 m/z scan range, 18 milisecond maximum injection time, centroid format, and a rapid scan rate. Data was search against the human proteome database (canonical sequences downloaded from Uniprot 10/22/2020) using the default parameters in MaxQuant[102,103] (version 1.6.12.0), with the exception that match-between-runs was enabled (0.7 min time window) and a variable modification (361.14601 Da) representing the addition of biotin phenol to tyrosine residues was included.

HLA loss of heterozygosity analysis

Whole exome capture and read sequencing were performed as previously described on 25 meningiomas overlapping with the discovery cohort (9 Immune-enriched, 16 non-Immune-enriched) with matched normal tissue controls[8]. Paired-end sequence data were aligned using the Burrows-Wheeler Aligner to the reference human genome

build hg19[81]. Duplicate removal, base quality recalibration, and multiple-sequence realignment were performed using Picard suite and Genome Analysis Toolkit[82,83]. Exome HLA Class I genotyping was performed using Polysolver and SOAP-HLA[104,105].

Single cell isolation and RNA sequencing

Fresh human meningioma (n=8) and dura (n=2) samples were acquired from the operating room and transported to the laboratory in PBS at 4°C. Tissue samples were minced with sterile #10 scalpels (#4-410, Integra LifeSciences) and incubated at 37°C in a Collagenase Type 7 solution (#LS005332, Worthington) until digested (30-60 minutes). Collagenase was used at a concentration of 0.1 mg/mL for tumor and brain-tumor interface samples, and at a concentration of 0.2 mg/mL for dura samples. Samples were incubated in Trypsin-EDTA 0.25% (#25200056, Thermo Fisher Scientific) at 37°C for 5 minutes, and in 1X RBC lysis buffer (#00-4300-54, eBioscience) at room temperature for 10 minutes. Finally, samples were sequentially filtered through 70 µM and 40 µM cell strainers (#352350 and #352340, Corning) to generate single-cell suspensions.

Single cell suspensions were processed for single cell RNA sequencing using a 10X Chromium controller, and libraries were generated using the Chromium Single Cell 3' Library & Gel Bead Kit v3 on a 10X Chromium controller using the manufacturer recommended default protocol and settings (#1000121, 10X Genomics), at a target cell recovery of 5,000 cells per sample. Libraries were sequenced on an Illumina NovaSeq 6000, targeting >50,000 reads/cell, at the UCSF Center for Advanced Technology.

Single cell RNA sequencing analysis

Library demultiplexing, read alignment to the GRCh38 human reference genome, identification of empty droplets, and UMI quantification was performed using CellRanger version 3.0.2 (https://github/com/10xGenomics/cellranger). Cells with greater than 500 unique genes, less than 10,000 unique genes, and less than 20% of reads attributed to mitochondrial transcripts were retained. Single cell UMI count data were preprocessed in R version 3.6.1 with the Seurat[106,107] package version 3.0.1 using the sctransform[108] workflow, with scaling based on regression of UMI count and percentage of reads attributed to mitochondrial genes per cell. Dimensionality reduction was performed using principal component analysis, and principal components were corrected for batch effects using Harmony[109]. Uniform Manifold Approximation and Projection (UMAP) was performed on the reduction data with a minimum distance metric of 0.2 and Louvain clustering was performed using a resolution of 0.4. Marker identification and differential gene expression was performed in Seurat using a minimum fraction of detection of 0.75 and a minimum log-fold change of 0.5.

The presence or absence of CNVs in individual cells was assessed using CONICSmat[37]. Briefly, a two-component Gaussian mixture model was fit to the average expression values of genes on chromosome 22q across all cells assessed. CNVs were assessed in cells from tumor samples with copy-number loss of chromosome 22q at a bulk level as determined by DNA methylation, and for cells from copy-neutral normal dura samples. The command 'plotAll' from the CONICSmat R package was run with the parameters 'repetitions=100, postProb=0.75'. Cells with a posterior probability less than 0.15 were identified as tumor, while cells with a posterior probability greater than 0.85

were identified as normal. Clusters with greater than 80% of cells with intact chromosome 22q were determined to be non-meningioma cell clusters. Standard immune, neural, and vascular markers in the top 50 differentially expressed genes of the non-meningioma cell clusters were used to classify non-tumor clusters. Cell cycle phases of individual cells were assigned with the standard 'CellCycleScoring' function in Seurat. In brief, using previously described single-cell cell cycle marker genes[110], average expression levels were calculated for each cell using G2M and S phase marker genes, respectively. If both average expression levels were less than 0, cells were classified as G1 phase. Otherwise, they were classified as either G2M or S phase, depending on which average expression was greater. Meningioma cell clusters were labeled based on cell cycle phases of cells and gene programs were identified by inspection of the top 50 differentially expressed genes. Gene ontology and pathway analyses with Enrichr and literature searches via Pubmed of differentially expressed genes helped identify upregulated pathways in meningioma cell clusters.

Reference transcriptomic signatures of single-cell clusters were generated using CIBERSORTx[111]. CIBERSORTx was run on a counts per million (CPM) matrix of all genes and 300 randomly sampled cells per cluster with a minimum expression fraction of 0.1 and default settings for all other parameters. Bulk RNA-seq expression of meningiomas was deconvolved with CIBERSORTx using CPM expression of genes across bulk samples and with the generated single-cell transcriptomic signatures.

Magnetic resonance imaging analysis

All patients in the discovery cohort underwent preoperative magnetic resonance imaging (MRI) on clinical scanners at either 1.5 or 3.0 Tesla field strength. MRI protocols varied across the study period, but all patients included for image analysis (n=169) had T1 pre- and post-intravenous gadolinium contrast agent administration sequences, T2-weighted spin echo sequences, and T2-weighted fluid attenuated inversion recovery (FLAIR) sequences. Post-contrast T1 images evaluated in this study were high-resolution 3D, allowing for multiplanar reconstruction. Evaluation of meningioma proximity to dural venous sinuses was performed qualitatively by a board-certified radiologist with a Certificate of Added Qualification in Neuroradiology (J.E.V-M.) on post-contrast T1 images. Meningiomas were classified as involving a dural venous sinus if they abutted a dural reflection or invaded the sinus.

Gene over-expression

For transient over-expression of FOXM1 or USF1, M10G cells were transfected with pCMV6-FOXM1 (#RC202246, Origene) or pCMV6-USF1 (#RC204915, Origene) plasmids at a ratio of 1 µg of DNA to 2 µl of FuGENE transfection reagent (#E2311, Promega). Cells were harvested 48 hours after transfection for RNA extraction. For stable over-expression, USF1 was cloned from pCMV6-USF1 into the pLVX-IRES-puro vector using restriction digest and ligation. Lentivirus was generated and introduced onto CH-157MN cells and stable polyclonal cell lines were generated using antibiotic selection as described above.

ChIP sequencing and enhancer/super-enhancer analysis

H3K27ac ChIP sequencing data were derived from 25 previously reported meningiomas[56] (3 Merlin-intact, 7 Immune-enriched, and 15 Hypermitotic). Enhancer and super enhancer analyses were performed as previously described[56]. Briefly, FASTQ reads were trimmed to remove low quality reads and adaptors with TrimGalore and uniquely mapped reads were aligned to the human reference genome hg19/GRCh37 with the Burrows-Wheeler Aligner[81]. SAMtools was used to sort and index BAMs, and PCR duplicates were removed with PicardTools. Peaks were called using MACS2 with the default log2 fold change enrichment of 2 compared to input and a p-value cutoff of 10^{-5}. Consensus peaksets and normalized H3K27ac densities were generating using the DiffBinds R package. Peaks present in at least 2 tumor samples were used to generate a consensus peakset and overlapping peaks were merged. Peaks on chromosomes X or Y and peaks intersecting ENCODE blacklisted regions v1 on haplotype chromosomes were excluded from analysis. Bigwig tracks were generated using DeepTools (v3.1.2) with RPKM normalization and were visualized using Integrative Genomics Viewer software. Super-enhancers were called using ROSE with default parameters[112,113]. Gene set enrichment networks were generated using ClueGO and visualized in Cytoscape[114,115]. Prediction of FOXM1-regulated genes was performed by first identifying FOXM1 binding motif sites using Homer to scan across the genome for the known FOXM1 motif. These sites were intersected with H3K27ac peaks in the consensus meningioma peakset, annotated to the nearest gene using Homer, and intersected with genes positively and significantly (FDR<0.05) correlated with FOXM1 expression as well as

genes upregulated in the Hypermitotic meningiomas compared to tumors from other DNA methylation groups (FDR<0.05).

ChIP quantitative reverse transcriptase PCR

ChIP qPCR was performed using the EZ-Magna ChIP A/G Chromatin Immunoprecipitation Kit (#17-10086, Millipore), according to manufacturer's instructions. Briefly, cells were fixed in 1% formaldehyde and sonicated to fragment sizes of 200-800 bp. Samples were incubated overnight with 10 µg USF1 antibody (#ab180717, Abcam) or IgG antibody bound to protein A and protein G magnetic beads. After antibody incubation, samples were washed once each with high salt, low salt, lithium chloride and TE buffers. Samples were de-crosslinked by incubation at 65°C for 4 hours, followed by incubation at 95°C for 10 minutes, and purified using a PCR purification kit (#K3100-01, Invitrogen). qPCR was performed using PowerUp SYBR Green Master Mix (#A25918, Thermo Fisher Scientific). QPCR primer sequences targeting gene promoters were NC1-F (5'-AAAAGCAGCCCATCTCTGTG-3'), NC1-R (5'-TGGGAGACAGAGCAAGACTC-3'), NC2-F (5'-TTCTAACTTGGCTCGGGCATC-3'), NC2-R (5'-TCGCCTAACCTCTTCAGCTTC-3'), CDK6-F (5'-TTGTCTTTCGGCTCGCTGTC-3'), and CDK6-R (5'-AATCCTCAGGCCCAGAAAGG-3').

Patients

Patients were treated with Abemaciclib 100 mg *per os* twice daily. Treatment was held in the setting myelosuppression (absolute neutrophil count less than 1.5), and treatment-associated diarrhea was managed with over-the-counter medications.

Meningioma volumes on serial magnetic resonance imaging studies were determined using MIM (MIM Software Inc), and the electronic medical record for all patients was reviewed in early 2021.

Nomograms

Prognostic models for LFFR were generated using multivariable Cox regression via the survival R package. The proportional hazards assumption was confirmed by visual inspection of the Schoenfeld residuals and the Schoenfeld global test[116]. Variables included in the final model were selected by a two-step process, first by a univariable Cox regression threshold of p≤0.05, followed by selection of features with greatest variable importance as estimated by the Breiman permutation method using concordance as the model metric[117]. The top 7 features were selected to allow for at least 10 events per variable in the final model. This process was repeated for creation of the DNA methylation group model and the CNV group model. Models were compared using the bootstrapped time-dependent delta-AUC and delta-Brier-score for LFFR at 5 years[118]. The survAUC R package was used to calculate time-dependent AUC and Brier-scores. Nomograms based on the final Cox models were visualized using the 'nomogram' function of the rms R package. Within nomograms, each variable contributes points (top row) to the total score, which estimates the probably of 5-year LFFR (bottom 2 rows)[73]. Cox model calibration of 5-year LFFR was estimated using the 'calibrate' function of the rms R package with default settings, utilizing Kaplan-Meier estimates, bootstrapping, and with an average group size of 50 subjects per calibration level. Unless otherwise specified, all bootstrap procedures were performed with 500 iterations. Recursive partitioning analysis

of CNV and methylation groups was performed using the rpart R package, with a minimum of 30 observations per split attempt and minimum of 15 observations per terminal leaf. The optimal complexity parameter was determined by 5-fold cross-validation, with selection of the most parsimonious model defined as the model with fewest splits and no more than one standard-error above the error of the best model[119]. Finally, interactive web nomogram graphical user interfaces were created using the DynNom R package.

Statistics

All experiments were performed with at least 3 biologic replicates. Experimental replicates are indicated in each panel or figure legend. Unless specified otherwise, lines represent means, and error bars represent standard error of the means. Results were compared using log-rank tests, Student's t tests, ANOVA, and Chi-squared tests, which are indicated in all figure legends. Statistical significance is shown by *p$\leq$0.05, **p$\leq$0.01, or ***p$\leq$0.0001.
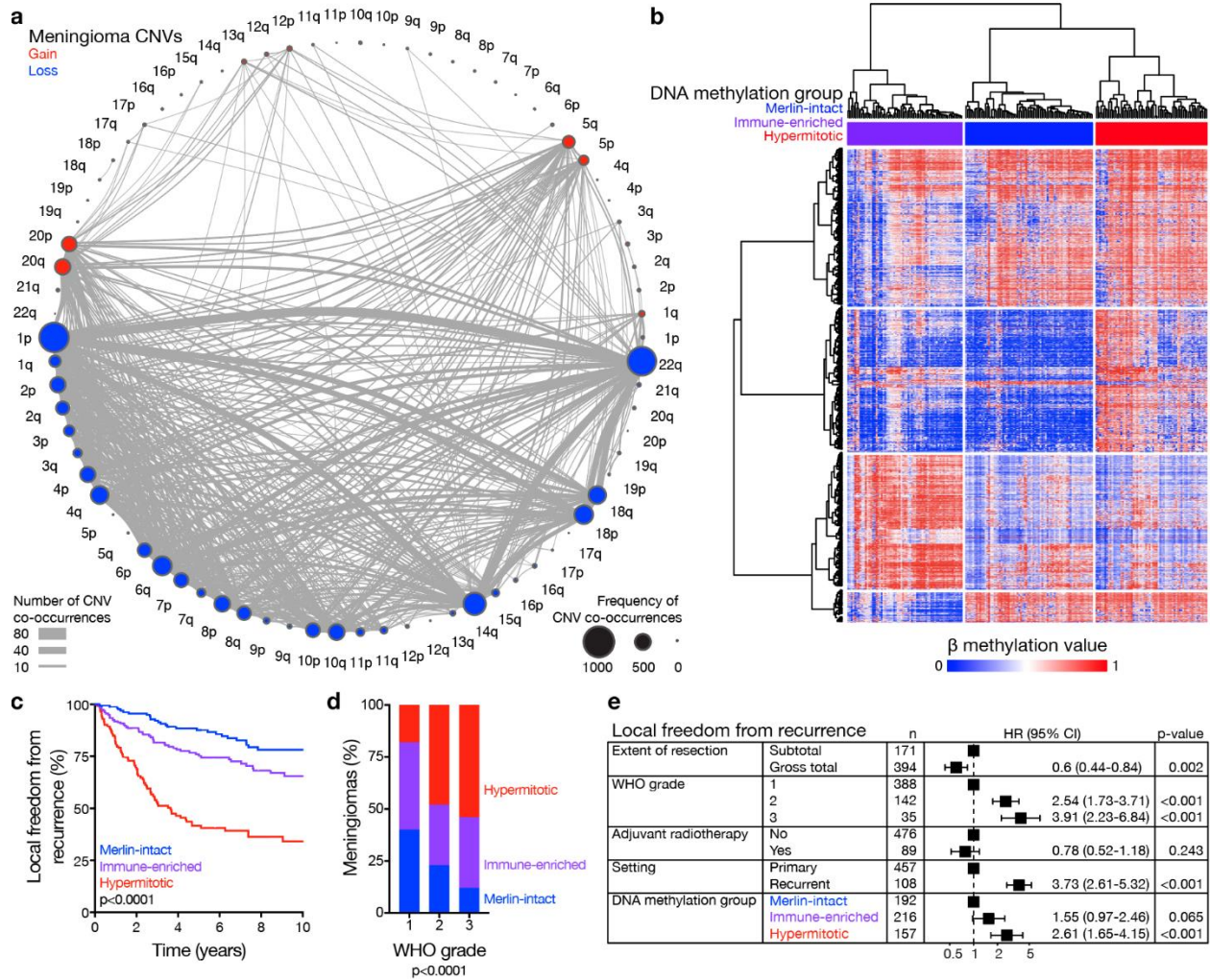
Figure 2.1 Meningiomas are comprised of 3 DNA methylation groups with distinct clinical outcomes.

a, Co-occurrence of chromosomal gains and losses in meningiomas (n=565). Circle size represents the frequency of copy number variant (CNV) co-occurrences. Line thickness represents the number of co-occurrences between CNVs. **b**, Unsupervised hierarchical clustering of meningiomas from the discovery cohort (n=200) using 2,000 differentially methylated DNA probes. **c**, Kaplan-Meier curves for meningioma local freedom from recurrence from the discovery and validation cohorts (n=565) across DNA methylation groups (Log-rank test). **d**, Meningioma WHO grades (n=565) across DNA methylation groups (Chi-squared test). **e**, Multivariable regression hazard ratio (HR) forest plots for local freedom from recurrence using meningioma clinical variables and DNA methylation groups (n=565, Cox proportional hazards model). Boxes represent means, and error bars represent 95% confidence intervals (CI).
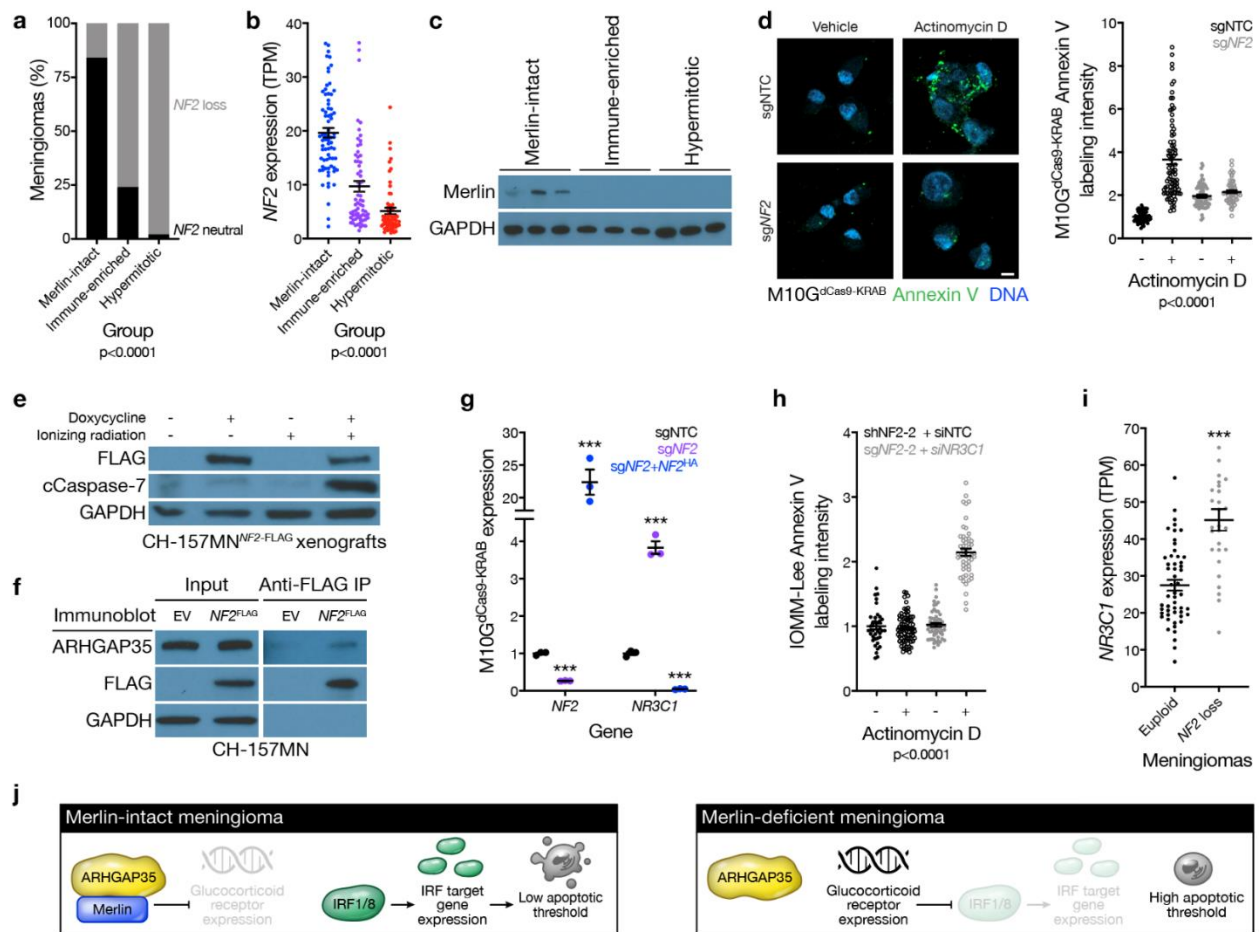
Figure 2.2 NF2/Merlin drives meningioma apoptosis.

a, Meningioma DNA methylation analysis of chromosome segment copy number loss containing the *NF2* locus across DNA methylation groups (n=565, Chi-squared test). **b**, Meningioma *NF2* transcripts per million (TPM) expression (n=200) across DNA methylation groups (ANOVA). **c**, Immunoblot for Merlin or GAPDH in 3 meningiomas with loss of at least one copy of the *NF2* locus from each meningioma DNA methylation group. **d**, Confocal microscopy and quantification of Annexin V in M10G$^{dCas9-KRAB}$ cells stably expressing a non-targeting control single-guide RNA (sgNTC) or a single-guide RNA suppressing *NF2* (sg*NF2*) after 24 hours of actinomycin D or vehicle control treatment. DNA is marked with DAPI. Scale bar 10 μM (ANOVA). **e**, Immunoblot for FLAG, cleaved Caspase-7 (cCaspase-7), or GAPDH from CH-157MN xenografts stably expressing doxycycline-inducible Merlin encoding a FLAG tag (*NF2*-FLAG) in NU/NU mice after 7 days of doxycycline or vehicle treatment, and 24 hours after 4 Gy ionizing radiation or control treatment. **f**, Immunoblot for ARHGAP35 or FLAG after FLAG immunoprecipitation from CH-157MN cells stably expressing Merlin encoding a FLAG tag (*NF2*^{FLAG}). EV, empty vector. **g**, QPCR for *NF2* or *NR3C1* in M10G$^{dCas9-KRAB}$ cells stably expressing sgNTC, sg*NF2*, or sg*NF2* with *NF2* rescue (sg*NF2*+*NF2*^{HA}). **h**, Quantification of Annexin V confocal microscopy in IOMM-Lee cells stably expressing a short-hairpin RNA suppressing *NF2* (sg*NF2*-2) and transiently expressing a non-targeting control siRNA (siNTC) or siRNAs suppressing *NR3C1* (si*NR3C1*). Cells were treated as in **d** (ANOVA). **i**, *NR3C1* TPM expression in euploid meningiomas (n=52) or meningiomas with loss of *NF2* as the only CNV (n=28) (Student's t test). **j**, Model of Merlin pro-apoptotic tumor suppressor function in meningioma cells. Lines represent means, and error bars represent standard error of the means. ***p≤0.0001 (Student's t test).
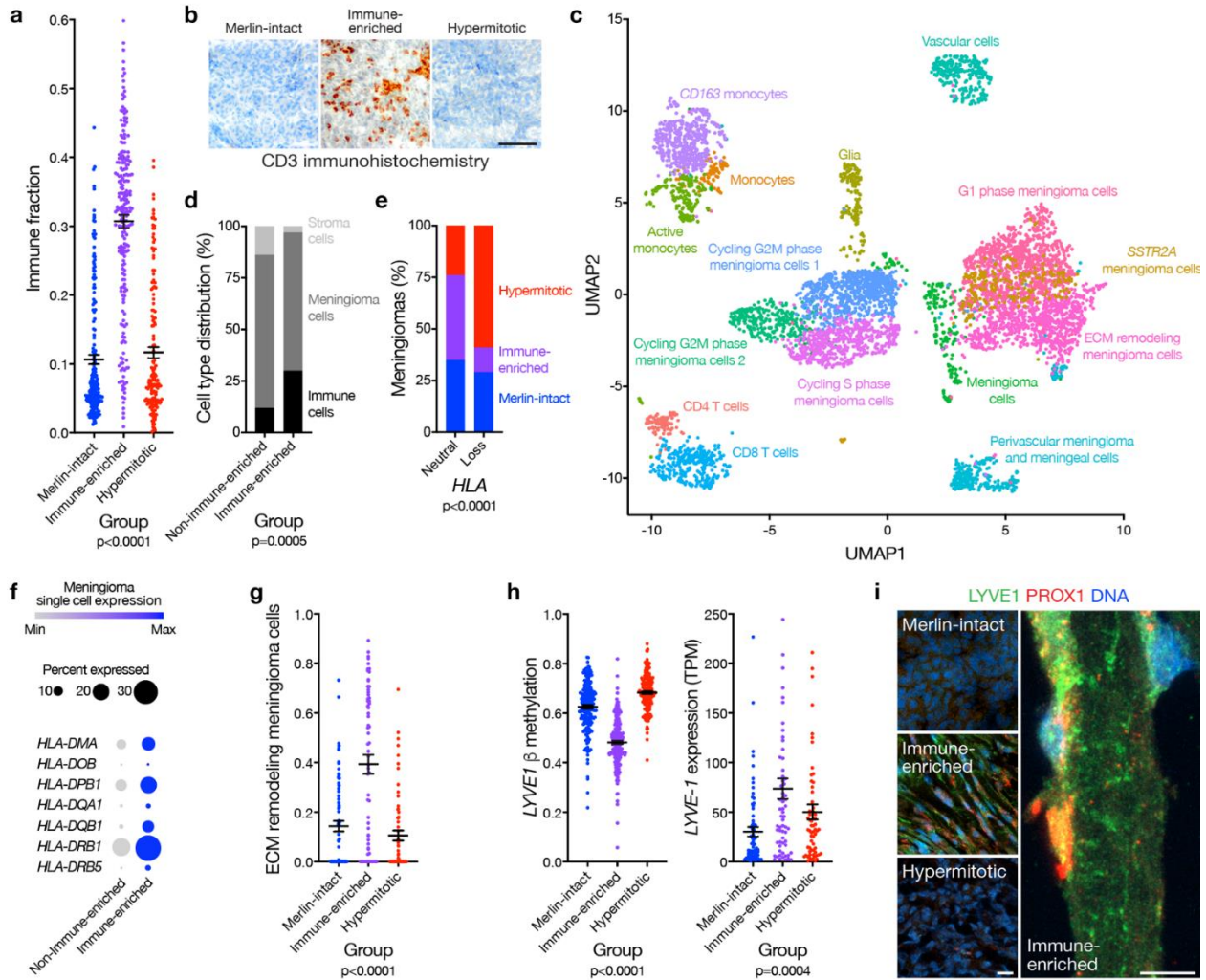
56

Figure 2.3 Meningioma immune enrichment is associated with HLA expression and meningeal lymphatics.

a, Meningioma DNA methylation estimation of leukocyte fractions (n=565) across DNA methylation groups (ANOVA). **b**, Representative images of CD3 immunohistochemistry across meningioma DNA methylation groups (n=87, $p < 0.0001$, Chi-squared test). Scale bar 100 μM. **c**, UMAP of single-cell RNA sequencing transcriptomes of 57,114 cells from 8 human meningioma samples and 2 human dura samples, colored by assignments from Louvain clustering. **d**, Single-cell RNA sequencing quantification of immune, stroma, and meningioma cells in Immune-enriched (n=5) and non-Immune-enriched (n=3) meningioma samples (Chi-squared test). **e**, Meningioma DNA methylation analysis of chromosome segment copy number loss containing the *HLA* locus across DNA methylation groups (n=565, Chi-squared test). **f**, Single-cell RNA sequencing relative expression of *HLA* genes in meningioma cells across Immune-enriched (n=5) and non-Immune-enriched (n=3) meningioma samples. Circle size denotes percentage of cells. Circle shading denotes average expression. **g**, Fraction of meningioma samples (n=200) classified as extracellular matrix (ECM) remodeling meningioma cells across DNA methylation groups, based on single-cell reference transcriptomes from **c**. **h**, Meningioma DNA methylation (n=565) of *LYVE-1* (cg26455970) and transcripts per million (TPM) expression (n=200) of *LYVE-1* across DNA methylation groups (ANOVA). **i**, Representative images of meningioma LYVE1 and PROX1 confocal immunofluorescence microscopy across DNA methylation groups (n=12). DNA is marked with Hoechst 33342. Scale bars 10 μM. Lines represent means, and error bars represent standard error of the means.
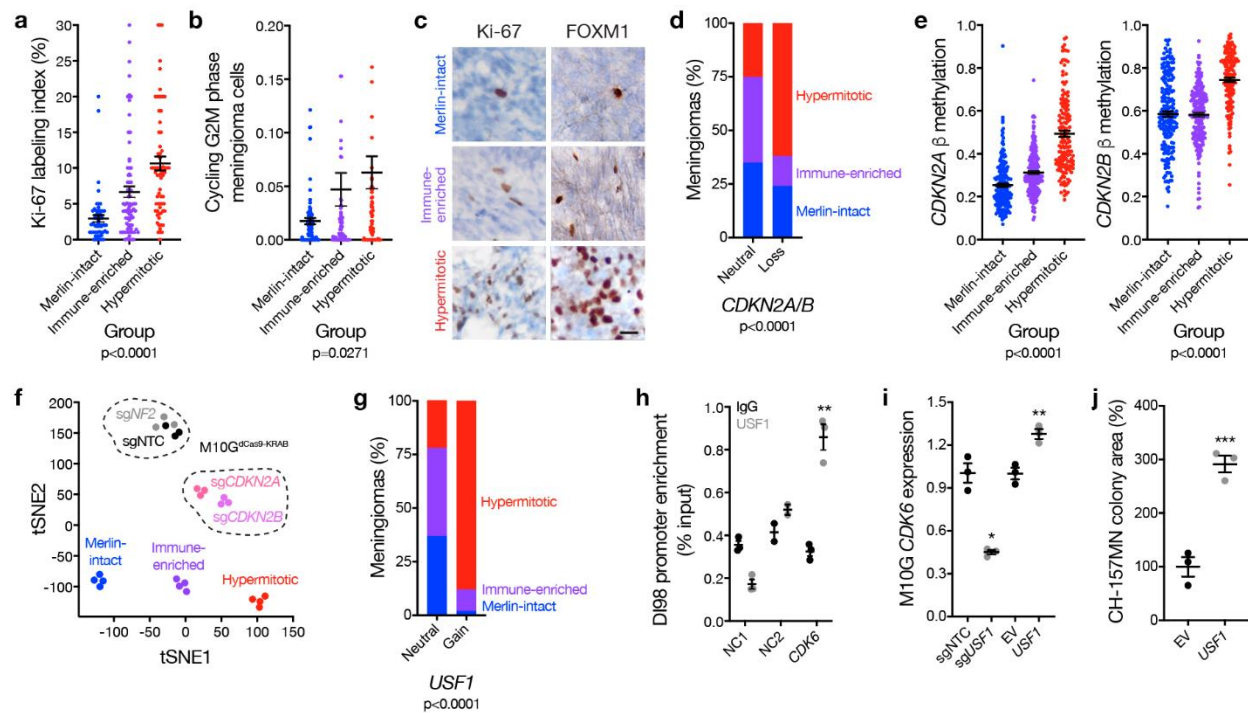
Figure 2.4 Convergent genetic mechanisms misactivate the cell cycle in meningioma.

a, Ki-67 labeling index from meningioma clinical pathology reports (n=206) across DNA methylation groups (ANOVA). **b**, Fraction of meningioma samples (n=200) classified as Cycling G2M phase meningioma cells across DNA methylation groups, based on single-cell reference transcriptomes. **c,** Representative images of meningioma Ki-67 and FOXM1 immunohistochemistry (n=92) across meningioma DNA methylation groups. Scale bar 10 μM. **d**, Meningioma DNA methylation analysis of chromosome segment copy number loss containing the *CDKN2A/B* locus across DNA methylation groups (n=565, Chi-squared test). **e**, Meningioma DNA methylation (n=565) of *CDKN2A* (cg26349275) or *CDKN2B* (cg08390209) across DNA methylation groups (ANOVA). **f**, tSNE plot of meningioma and meningioma cell line DNA methylation profiles. Meningiomas are comprised of 4 representative samples from each DNA methylation group. Cell line samples are comprised of triplicate M10G$^{dCas9-KRAB}$ cultures stably expressing a non-targeting control single-guide RNA (sgNTC) or single-guide RNAs suppressing *NF2* (sg*NF2*), *CDKN2A* (sg*CDKN2A*), or *CDKN2B* (sg*CDKN2B*). Differences in DNA methylation groups are captured in the tSNE1 axis, and a positive shift from Immune-enriched meningiomas to Hypermitotic meningiomas mimics the shift from M10G$^{dCas9-KRAB}$-sgNTC and M10G$^{dCas9-KRAB}$-sg*NF2* cells to M10G$^{dCas9-KRAB}$-sg*CDKN2A* and M10G$^{dCas9-KRAB}$-sg*CDKN2B* cells. Differences between tumors and cell lines are captured in the tSNE2 axis. **g**, Meningioma DNA methylation analysis of chromosomal segment copy number loss containing the *USF1* locus across DNA methylation groups (n=565, Chi-squared test). **h**, USF1 ChIP-QPCR in DI98 meningioma cells for the *CDK6* promoter compared to negative control primers targeting a gene desert (NC1) or a gene not predicted to be bound by USF1 (NC2) from ChIP sequencing (Student's t test). **i**, QPCR for *CDK6* in M10G$^{dCas9-KRAB}$ cells expressing sgNTC or a single-guide RNA suppressing *USF1* (sg*USF1*), or M10G cells over-expressing *USF1* or empty vector (EV) (Student's t test). **j**, Relative colony area of CH-157MN cells stably over-expressing USF1 or EV after 10 days of clonogenic growth (Student's t test). Lines represent means, and error bars represent standard error of the means. *p≤0.05, **p≤0.01.
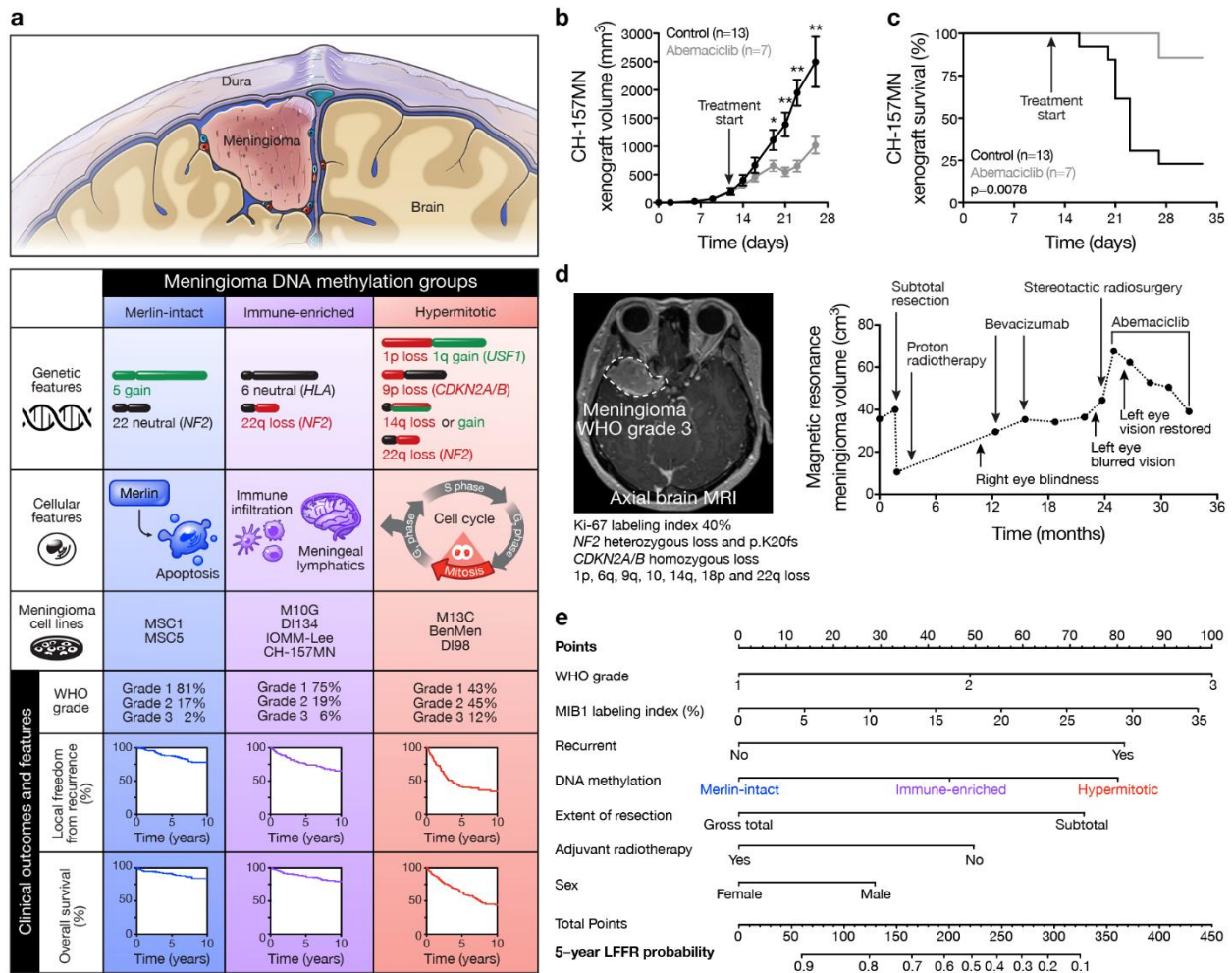
Figure 2.5 Clinical translation of meningioma DNA methylation groups.

a, Genetic, cellular, and clinical features across meningioma DNA methylation groups. DNA methylation profiling was performed on 9 meningioma cell lines to define reagents to study meningioma DNA methylation groups. **b**, Subcutaneous CH-157MN xenograft measurements in NU/NU mice treated with abemaciclib (100 μg/g) by daily oral gavage with versus control. Lines represent means, and error bars represent standard error of the means. *p≤0.05, **p≤0.01 (Student's t tests). **c**, Kaplan-Meier curve for CH-157MN xenograft overall survival in NU/NU mice treated as in **b** (Log-rank test). **d**, Magnetic resonance imaging and molecular features of a representative human meningioma (left) that was resistant to cytotoxic therapies but responded to cytostatic cell cycle inhibition (right). **e**, Nomogram for meningioma local freedom from recurrence (LFFR, n=201) integrating clinical features and DNA methylation groups. Variables contribute points (top row), which estimate the probably of 5-year LFFR (bottom rows)[73] (https://william-c-chen.shinyapps.io/RaleighLab_MethylationSubgroupNomogram/).
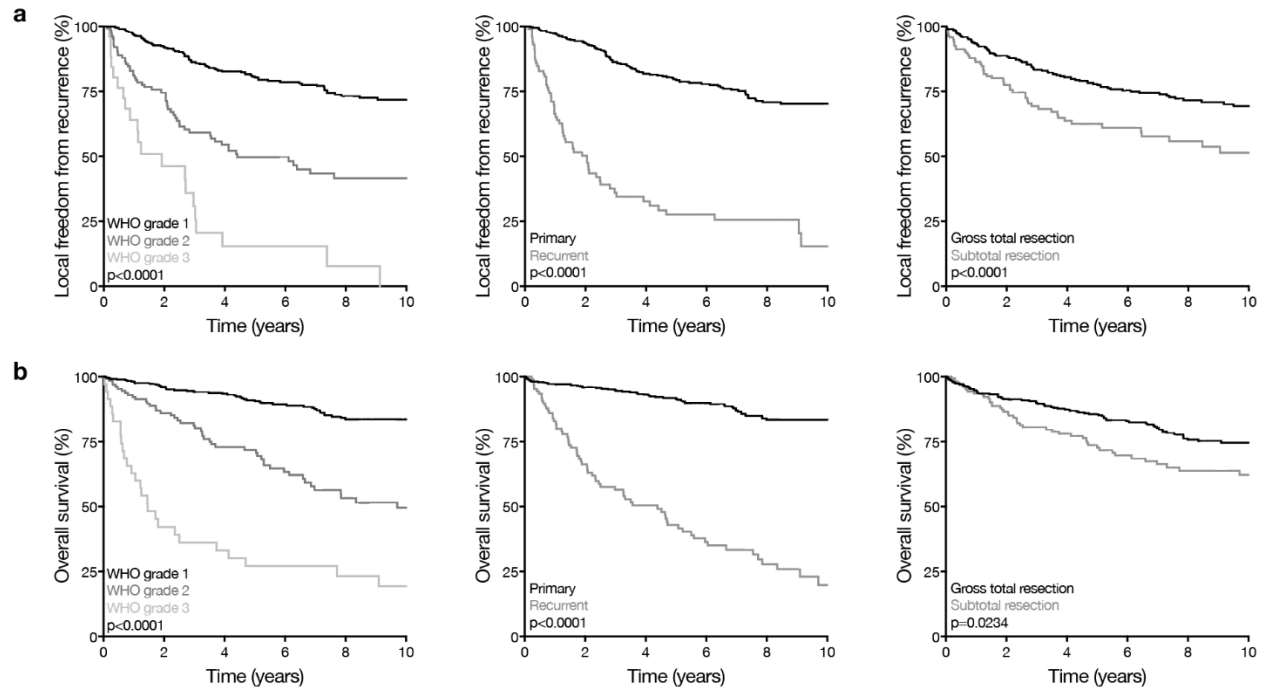
59

Figure S2.1 Clinical outcomes across meningioma DNA methylation discovery and validation cohorts.

a, Kaplan-Meier curves for meningioma local freedom from recurrence (n=565) across clinical contexts (Log-rank tests). **b**, Kaplan-Meier curves for meningioma overall survival (n=565) across clinical contexts (Log-rank tests).
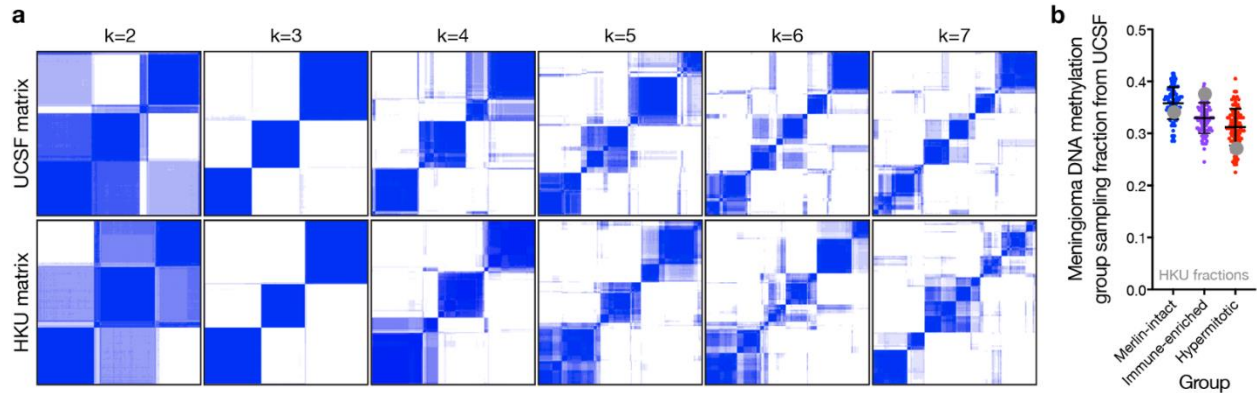
Figure S2.2 DNA methylation analysis using SeSAMe to control for CNV artifacts identifies 3 robust groups of meningiomas.

a, K-means consensus clustering of meningioma DNA methylation profiles from the discovery (n=200, UCSF) and validation (n=365, HKU) cohorts. **b**, Sampling distributions of DNA methylation group fractions from the discovery cohort, with the observed DNA methylation group fractions from the validation cohort denoted in grey. Lines represent means, and error bars represent standard deviations. The observed fractions of each DNA methylation group from the validation cohort fall within the sampling distributions from the discovery cohort, but Immune-enriched and Hypermitotic meningioma fractions from the validation cohort fall outside of the first standard deviation of sampling in the discovery cohort. These differences can be attributed to the enrichment of high grade meningiomas and worse outcomes in the discovery cohort compared to the validation cohort (Extended Data Table 1).
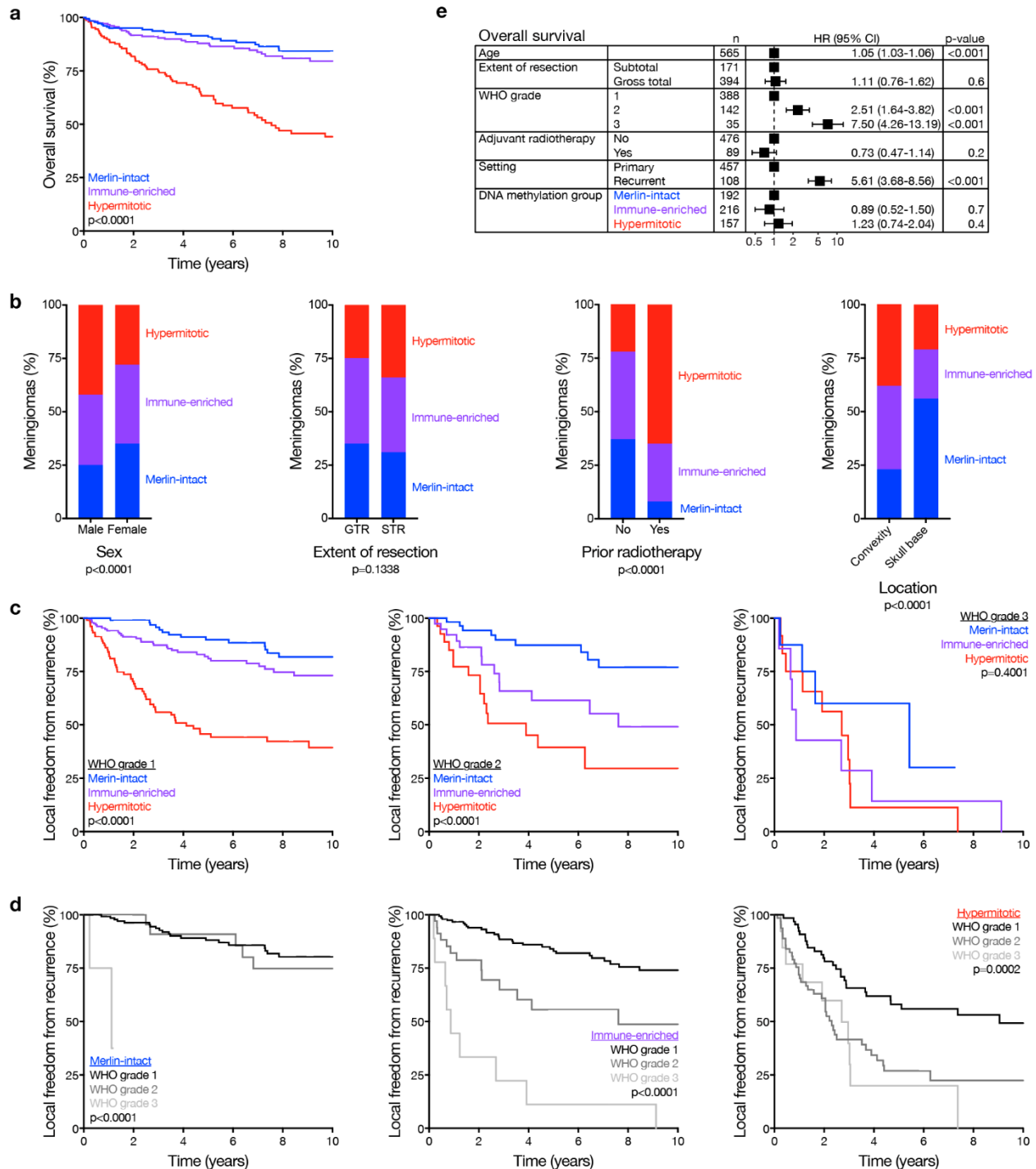
Figure S2.3 Clinical correlations across meningioma DNA methylation groups.

a, Kaplan-Meier curve for overall survival (n=565) across meningioma DNA methylation groups (Log-rank test). **b**, Meningioma clinical features (n=565) across DNA methylation groups (Chi-squared tests). GTR, gross total resection. STR, subtotal resection. **c, d**, Kaplan-Meier curves for meningioma local freedom from recurrence (n=565) across WHO grades and DNA methylation groups (Log-rank tests). **e**, Multivariable regression hazard ratio (HR) forest plots for overall survival using meningioma clinical variables and DNA methylation groups (n=565, Cox proportional hazards model). Age per year older than the median. Boxes represent means, and error bars represent 95% confidence intervals (CI).

62
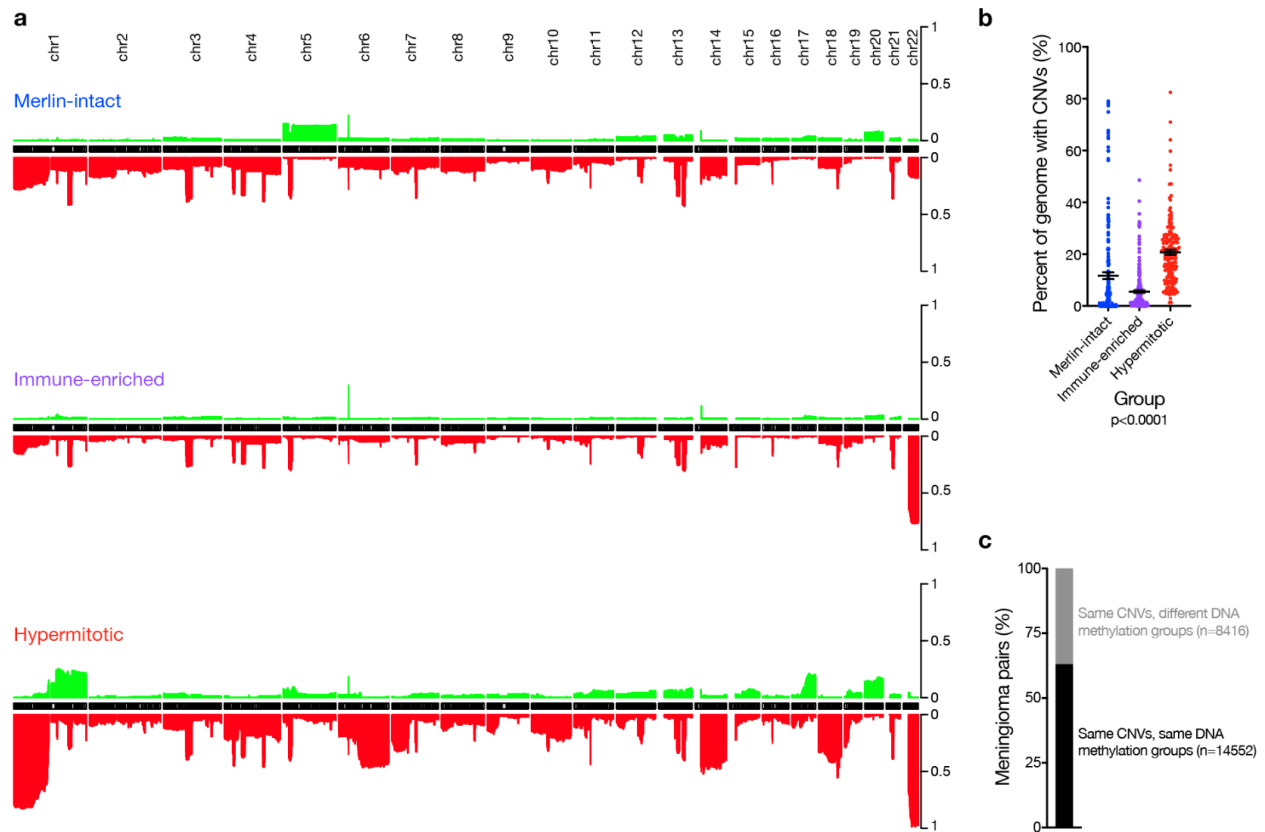
Figure S2.4 CNVs across meningioma DNA methylation groups.

a, Frequency of copy number losses (red) and gains (green) across meningioma DNA methylation groups. **b**, Meningioma genomes (n=565) with copy number variations (CNVs) across DNA methylation groups (ANOVA). Lines represent means, and error bars represent standard error of the means. **c**, Analysis of meningioma pairs with overlapping CNVs reveals 37% of meningiomas with identical CNVs are assigned to different DNA methylation groups, demonstrating meningioma CNV profiles are independent from meningioma DNA methylation groups.

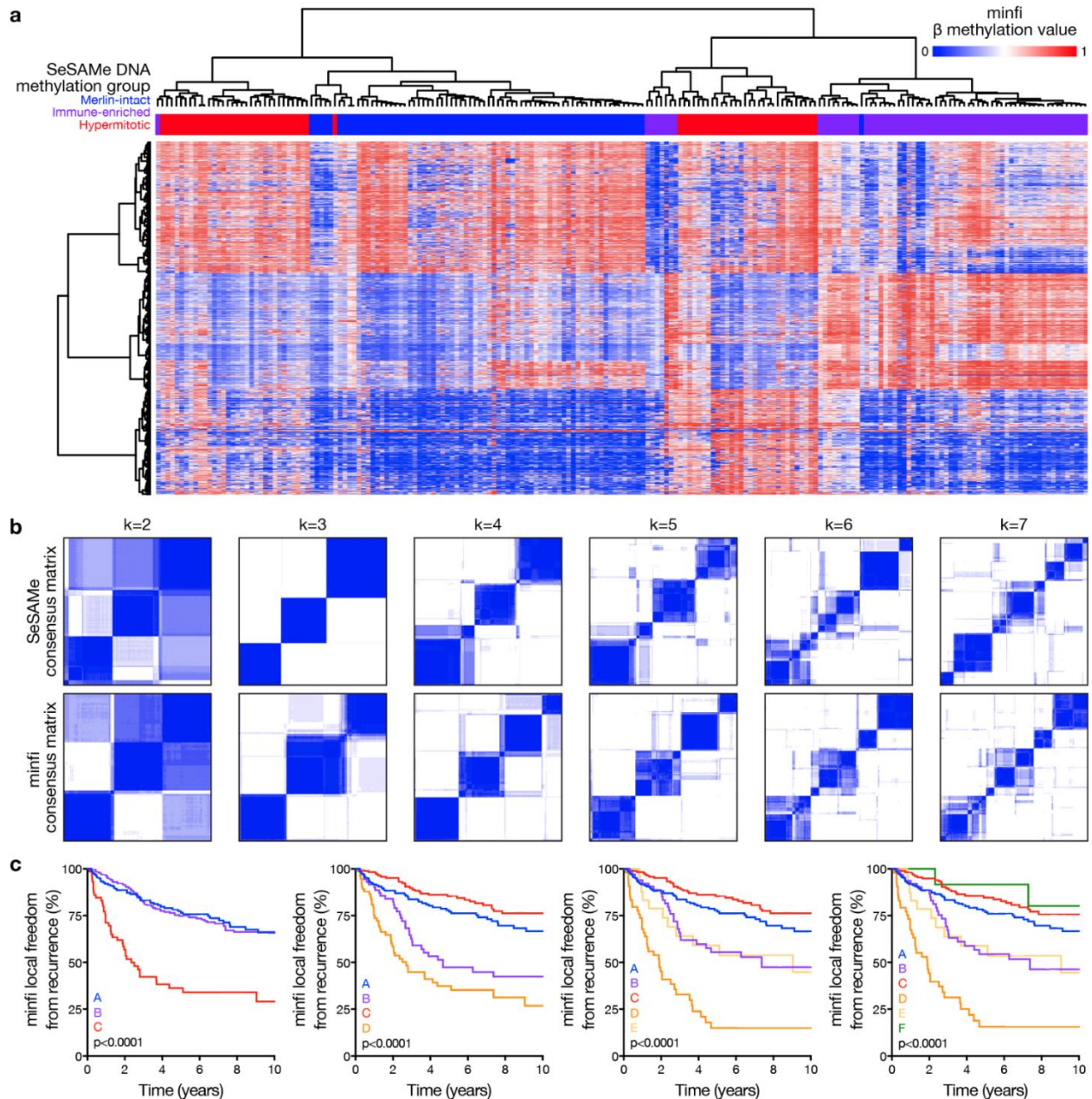*Figure S2.5* Meningioma DNA methylation grouping using SeSAMe to control for CNV artifacts is superior to approaches that are biased by CNV artifacts.

a, Unsupervised hierarchical clustering of meningiomas from the discovery cohort (n=200) using 2,000 differentially methylated DNA probes from the minfi pre-processing pipeline, which does not control for CNV artifacts. SeSAME meningioma DNA methylation groups (21% altered by minfi) are shown beneath the vertical dendrogram. **b**, K-means consensus clustering of meningiomas from the discovery and validation cohorts (n=565) using differentially methylated DNA probes and β values from SeSAMe or minfi. SeSAMe consensus clustering clearly identifies 3 groups as the optimal number, but minfi consensus clustering is unable to discriminate between 3 and 4 clusters. **c**, Kaplan-Meier curves for meningioma local freedom from recurrence (n=565) across minfi DNA methylation groups fails to identify a grouping scheme with non-redundant differences in clinical outcomes, in contrast to SeSAMe DNA methylation groups (Fig. 1c) (Log-rank tests).
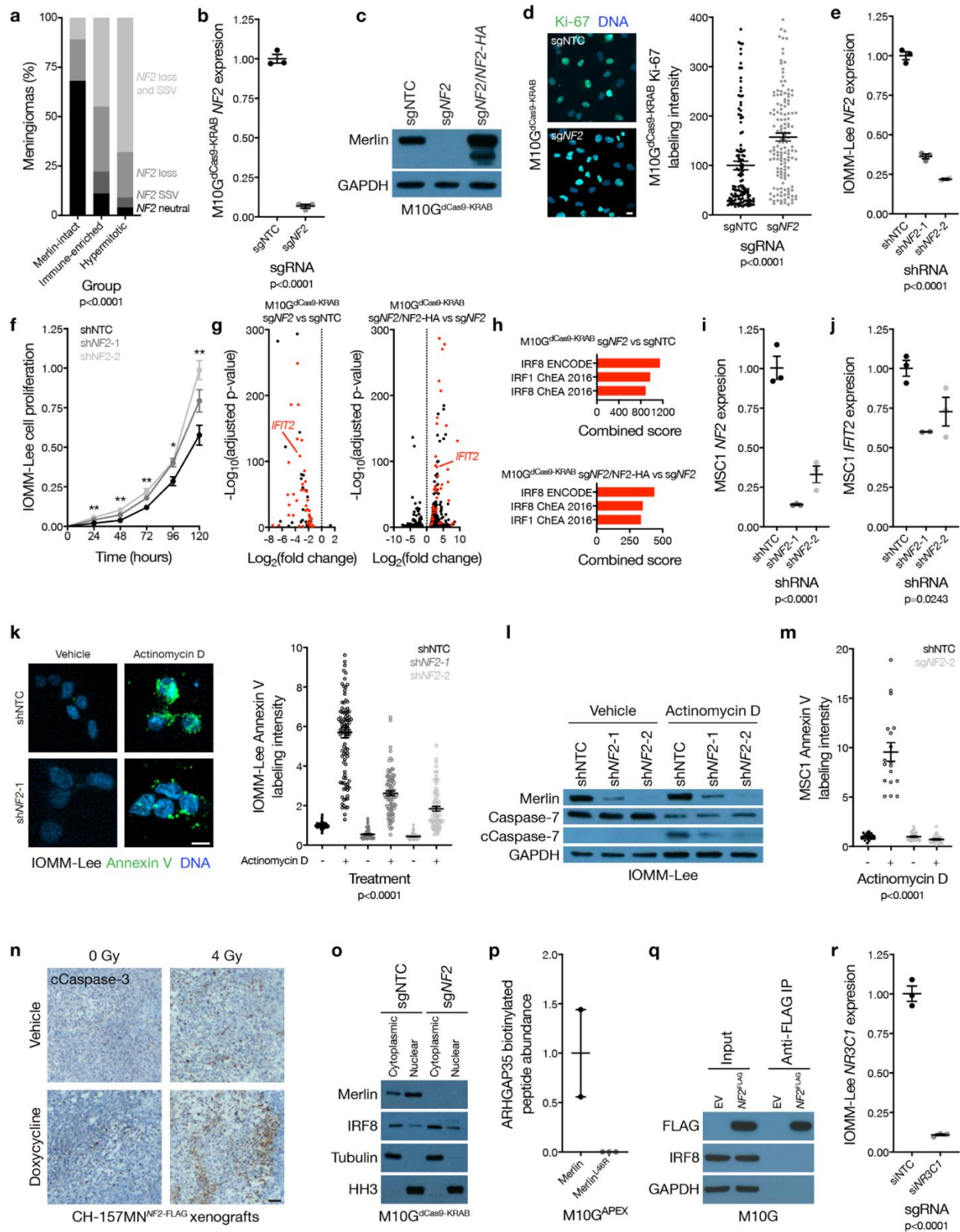
64

Figure S2.6 Mechanisms of NF2/Merlin tumor suppression in meningioma cells.

a, Meningioma *NF2* copy number loss and targeted sequencing of somatic short variants (SSV, n=65) across DNA methylation groups (Chi-squared test). **b**, QPCR for *NF2* in M10G$^{dCas9-KRAB}$ cells expressing a non-targeting control single-guide RNA (sgNTC) or a single-guide RNA suppressing *NF2* (sg*NF2*) (Student's t test). **c**, Immunoblot for Merlin or GAPDH in M10G$^{dCas9-KRAB}$ cells expressing sgNTC, sg*NF2*, or sg*NF2* with *NF2* rescue (sg*NF2*+*NF2*^{HA}). **d**, Confocal immunofluorescence microscopy and quantification of Ki-67 in M10G$^{dCas9-KRAB}$ cells from **b**. DNA is marked with Hoechst 33342. Scale bar 10 μM (Student's t test). **e**, QPCR for *NF2* in IOMM-Lee cells stably expressing a non-targeting control shRNA (shNTC) or shRNAs suppressing *NF2* (sh*NF2*-1 or sh*NF2*-2) (ANOVA). **f**, MTT cell proliferation of IOMM-Lee cells from **e**, normalized to shNTC at 120 hours. *p≤0.05, **p≤0.01 (ANOVA). **g**, Volcano plots of relative gene expression from RNA sequencing of M10G$^{dCas9-KRAB}$ cells in **c**. Interferon-regulated genes (including *IFIT2*, validated in **j**) are marked in red. **h**, Gene ontology analysis of differentially expressed genes from RNA sequencing of M10G$^{dCas9-KRAB}$ cells in **g**. **i**, QPCR for *NF2* in MSC1 cells stably expressing shNTC, sh*NF2*-1, or sh*NF2*-2 (ANOVA). **j**, QPCR for the IRF target gene *IFIT2* in MSC1 cells from **i**. **k**, Confocal microscopy and quantification of Annexin V in IOMM-Lee cells from **e** treated with actinomycin D or vehicle control for 24 hours. DNA is marked with DAPI. Scale bar 10 μM (ANOVA). **l**, Immunoblot for Merlin, Caspase-7, cleaved Caspase-7 (cCaspase-7), or GAPDH in IOMM-Lee cells from **k**. **m**, Quantification of Annexin V confocal microscopy in MSC1 cells stably expressing sgNTC or sg*NF2*-2. Cells were treated as in **k** (ANOVA). **n**, Representative images of cleaved Caspase-3 (cCaspase-3) immunohistochemistry from CH-157MN xenografts stably expressing doxycycline-inducible Merlin encoding a FLAG tag (*NF2*-FLAG) in NU/NU mice after 7 days of doxycycline or vehicle treatment, and 24 hours after 4 Gy ionizing radiation or control treatment. Scale bar 100 μM. **o**, Immunoblot for Merlin, IRF8, Tubulin, or Histone H3 (HH3) in cytoplasmic or nuclear fractions of M10G$^{dCas9-KRAB}$ cells from **b**. **p**, Normalized proteomic proximity-labeling mass spectrometry from M10G cells stably expressing Merlin constructs with APEX tags. **q**, Immunoblot for IRF8 or FLAG after FLAG immunoprecipitation from M10G cells stably expressing Merlin encoding a FLAG tag (*NF2*^{FLAG}). EV, empty vector. **r**, QPCR for the glucocorticoid receptor (*NR3C1*) in IOMM-Lee cells expressing a non-targeting control siRNA (siNTC) or siRNAs suppressing *NR3C1* (si*NR3C1*) (Student's t test). Lines represent means, and error bars represent standard error of the means.
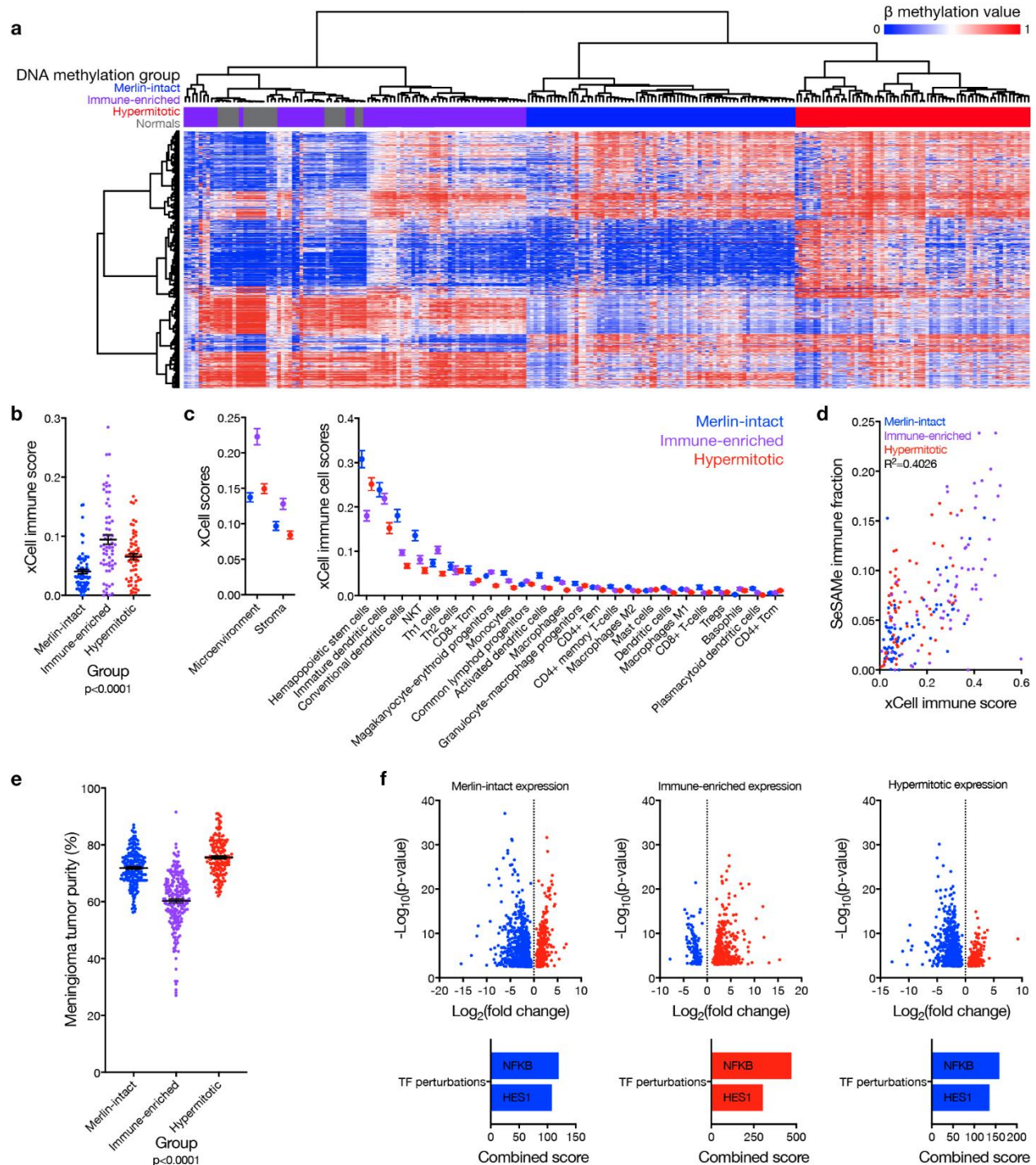
Figure S2.7 Genomic and cellular characteristics of Immune-enriched meningiomas.

a, Unsupervised hierarchical clustering of meningiomas (n=200) and normal tissue samples (muscle or fat) from meningioma patients (n=27) using 2,000 differentially methylated DNA probes. **b**, Meningioma RNA sequencing xCell immune score (n=200) across DNA methylation groups (ANOVA). **c**, Meningioma RNA sequencing xCell scores (n=200) across DNA methylation groups for microenvironment and stroma (left), and individual immune cell types (right). **d**, Correlation of DNA methylation leukocyte fraction (SeSAMe) and RNA sequencing immune score (xCell) (n=200) across DNA methylation groups. **e,** Meningioma DNA methylation tumor purity (n=565) across DNA methylation groups (ANOVA). **f**, Volcano plots of meningioma

differential gene expression (n=200) across DNA methylation groups iteratively comparing one group versus the others, with gene ontology transcription factor (TF) perturbation analysis of differentially enriched (red) or suppressed (blue) genes. Lines represent means, and error bars represent standard error of the means.

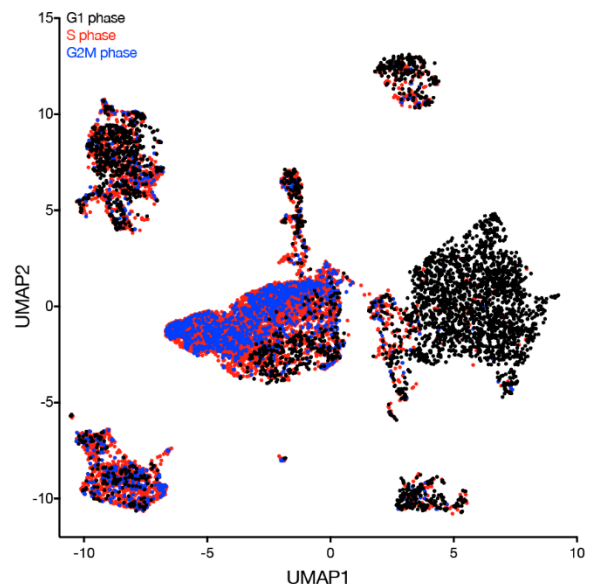| Sample	DNA methylation group	22q status	C0	C1	C2	C3	C4	C5	C6	C7	C8	C9	C10	C11	C12	C13	C14	Total
MSC1	Merlin-intact	Intact	1441	191	11	152	17	46	28	6	5	578	19	29	11	3	1	2538
MSC2	Immune-enriched	Loss	8	0	2	710	0	34	5	8	0	86	22	11	0	21	7	914
MSC3	Hypermitotic	Loss	638	383	26	83	70	8	44	11	57	939	56	20	911	38	3	3287
MSC4	Merlin-intact	Intact	855	1353	13	774	10	188	2170	1787	23	354	88	70	62	58	65	7870
MSC4 dura	---	Intact	228	13	5	32	0	265	159	140	0	24	135	12	0	3	129	1145
MSC5	Immune-enriched	Loss	6680	1510	18	1198	39	83	181	363	11	38	65	7	181	18	30	10422
MSC5 brain/tumor interface	Immune-enriched	Loss	198	6315	28	748	5	64	282	260	80	85	56	180	226	27	14	8568
MSC5 dura	---	Intact	9	5	3	40	0	160	57	163	0	0	51	6	17	0	43	554
MSC6	Immune-enriched	Intact	28	7	2509	330	1783	2546	265	154	1109	60	905	90	0	173	415	10374
MSC6 brain/tumor interface	Immune-enriched	Intact	35	19	3364	1164	2662	230	278	252	1847	264	554	1507	0	691	304	13171
Total	---	---	10120	9796	5979	5231	4586	3624	3469	3144	3132	2428	1951	1932	1408	1032	1011	57114
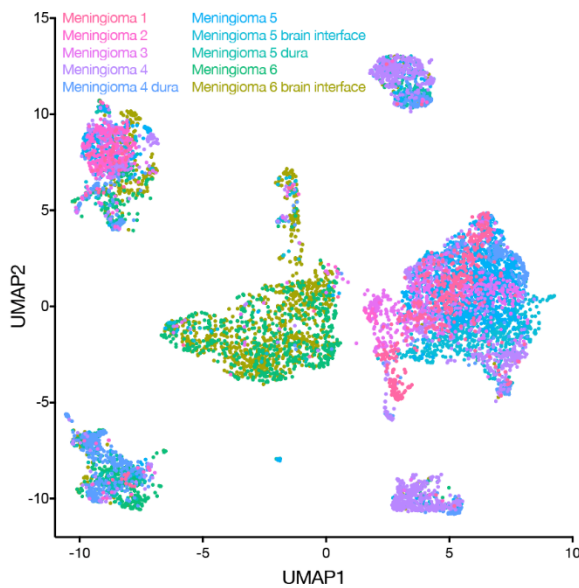
Figure S2.8 Meningioma single-cell RNA sequencing.

a, Cells in reduced dimensionality clusters from each sample analyzed using single-cell RNA sequencing. DNA methylation groups and chromosome 22q status of meningioma samples are annotated. **b**, UMAP of single-cell RNA sequencing transcriptomes of 57,114 cells from 8 human meningioma samples and 2 human dura samples, colored by sample of origin. **c**, UMAP of single-cell RNA sequencing transcriptomes from **b**, colored by cell cycle phase, as assigned by the 'CellCycleScoring' function in the Seurat R package.

Figure S2.9 Meningioma single-cell transcriptome cell types.

a, Percentage of cells with loss of chromosome 22q (whole arm) in reduced dimensionality clusters identified using CONICSmat. Cells from meningioma samples with loss of chromosome 22q and from dura samples with intact chromosome 22q were used for this analysis. **b**, Heatmap of differentially expressed genes across reduced dimensionality clusters, downsampled to 100 cells per cluster. **c**, Violin plots of marker gene expression across reduced dimensionality clusters. Lines represent means, and dotted lines represent quartiles.
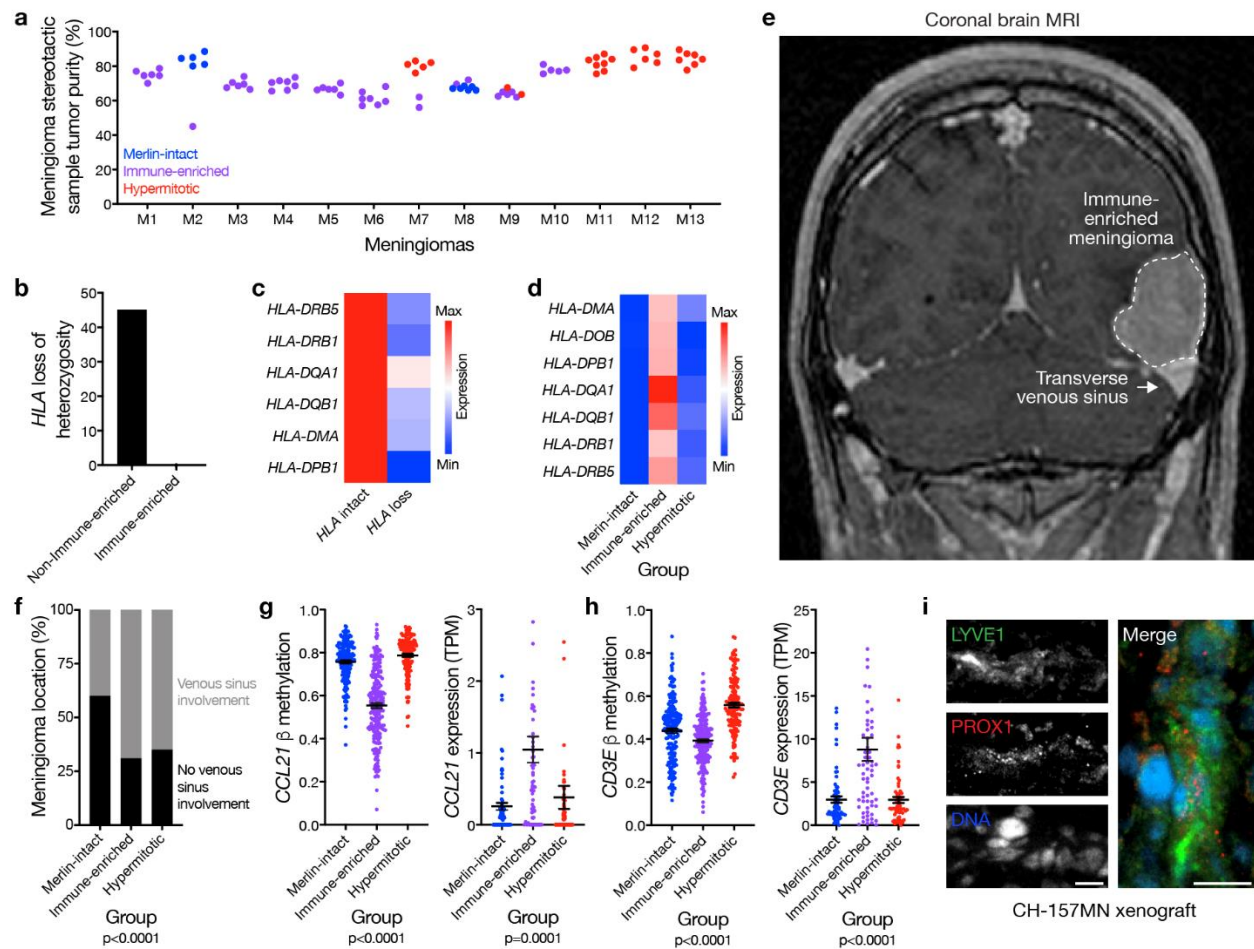
Figure S2.10 Mechanisms of meningioma immune infiltration.

a, Meningioma DNA methylation tumor purity of 86 spatially-distinct samples from 13 meningiomas, nonoverlapping with the meningiomas from the discovery or validation cohorts, colored by DNA methylation group. **b**, Percentage of meningiomas with *HLA* loss of heterozygosity from whole-exome sequencing of non-Immune-enriched (n=11) and Immune-enriched (n=5) meningiomas (and paired normal samples) overlapping with the discovery cohort. **c**, Meningioma RNA sequencing (n=200) relative expression of *HLA* genes according to *HLA* status. The expression of each gene in each row is normalized to the condition with greater expression (*HLA* intact or *HLA* loss). **d**, Meningioma RNA sequencing (n=200) relative expression of *HLA* genes across DNA methylation groups. *HLA* gene expression is normalized to the highest expressed gene across the 7 *HLA* genes shown. **e, f**, Meningioma location on preoperative magnetic resonance imaging (n=169) across DNA methylation groups (Chi-squared test). Representative magnetic resonance image shown. **g**, Meningioma DNA methylation (n=565) of *CCL21* (cg27443224) and transcripts per million (TPM) expression (n=200) of *CCL21* across DNA methylation groups (ANOVA). **h**, Meningioma DNA methylation (n=565) of *CD3E* (cg08956138) and transcripts per million (TPM) expression (n=200) of *CD3E* across DNA methylation groups (ANOVA). **i**, Representative image of LYVE1 and PROX1 confocal immunofluorescence microscopy in CH157-MN xenografts in NU/NU mice (n=3). DNA is marked with Hoechst 33342. Scale bars 10 μM. Lines represent means, and error bars represent standard error of the means.
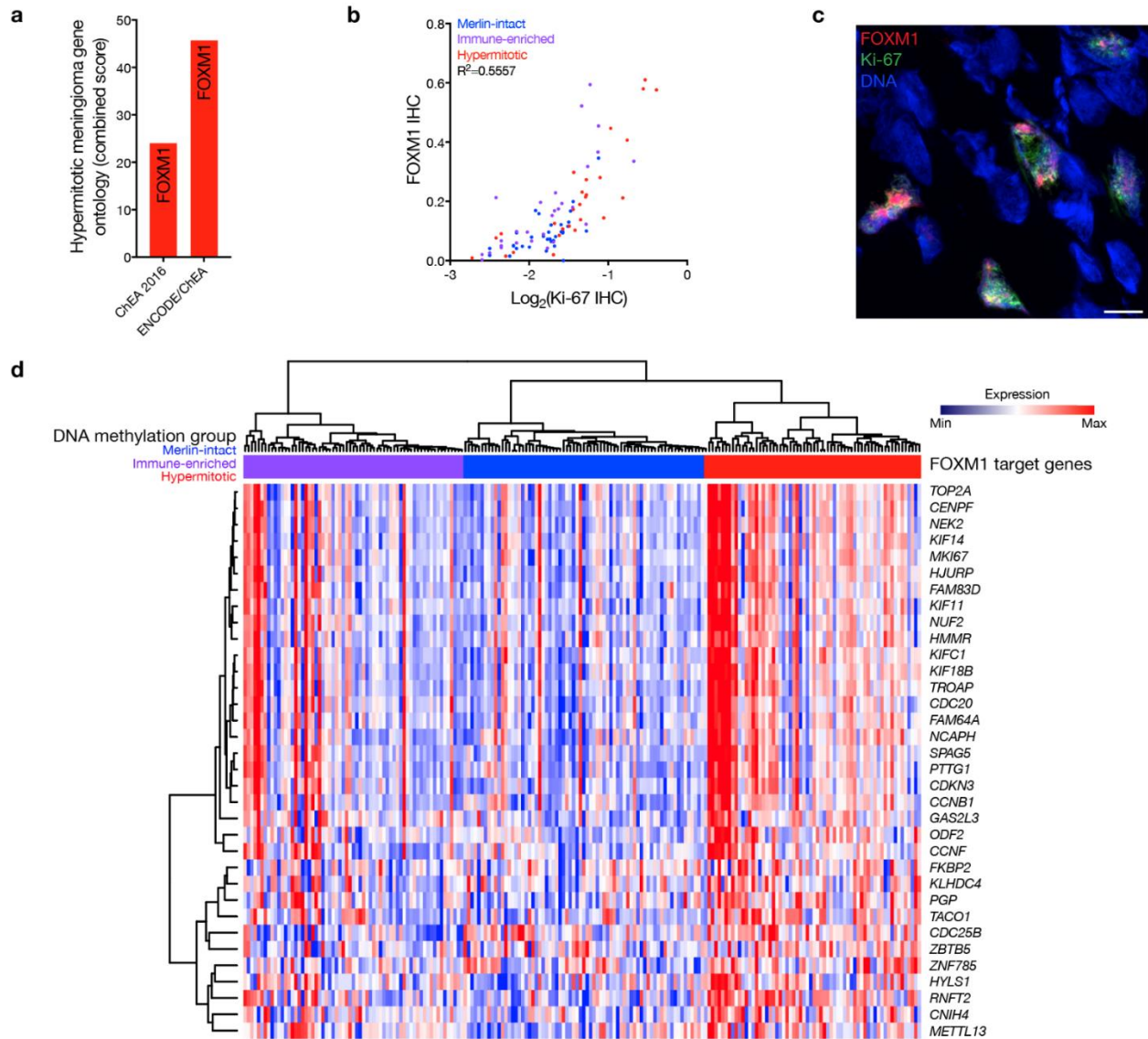
Figure S2.11 Meningioma DNA methylation groups are distinguished by FOXM1 and FOXM1 target gene expression.

a, Gene ontology analysis of differentially expressed genes in Hypermitotic meningiomas compared to tumors from other DNA methylation groups. ChEA, ChIP-X Enrichment Analysis. **b**, Correlated quantification of meningioma Ki-67 and FOXM1 immunohistochemistry (n=92) across meningioma DNA methylation groups. **c**, Representative image of meningioma Ki-67 and FOXM1 confocal immunofluorescence microscopy. DNA is marked with DAPI. Scale bar 10 μM. **d**, Heatmap of relative expression of FOXM1 target genes, nonoverlapping with E2F1 target genes, across meningioma DNA methylation groups (n=200). FOXM1 and E2F1 transcription factor targets were identified from the ChIP-X Enrichment Analysis (CHEA) dataset within the Harmonizome. SeSAME meningioma DNA methylation groups are shown beneath the vertical dendrogram.

Figure S2.12 Meningioma DNA methylation groups are not distinguished by E2F1 target gene expression.

a, Heatmap of relative expression of E2F1 target genes, nonoverlapping with FOXM1 target genes, across meningioma DNA methylation groups (n=200). FOXM1 and E2F1 transcription factor targets were identified from the ChIP-X Enrichment Analysis (CHEA) dataset within the Harmonizome. SeSAME meningioma DNA methylation groups are shown beneath the vertical dendrogram.
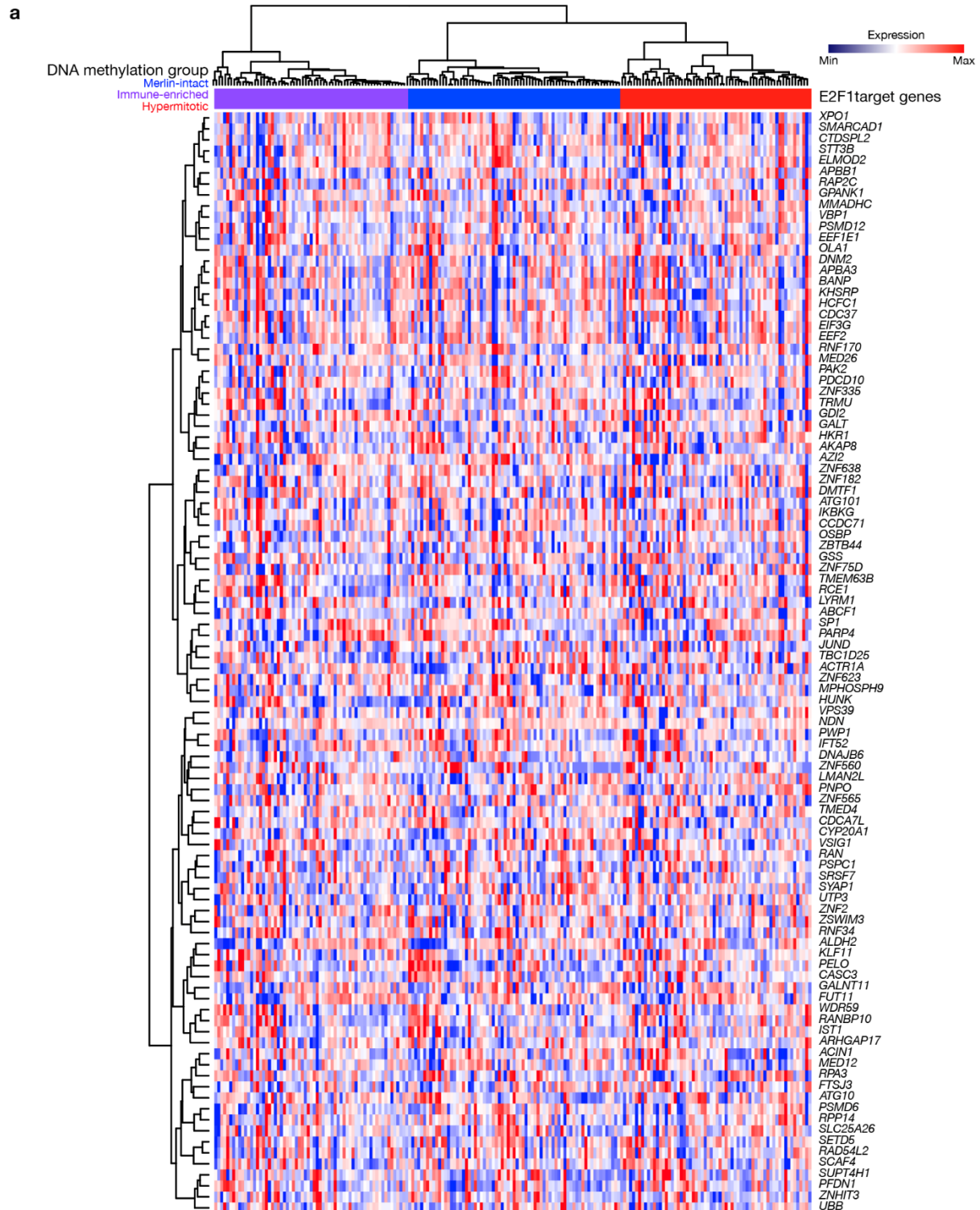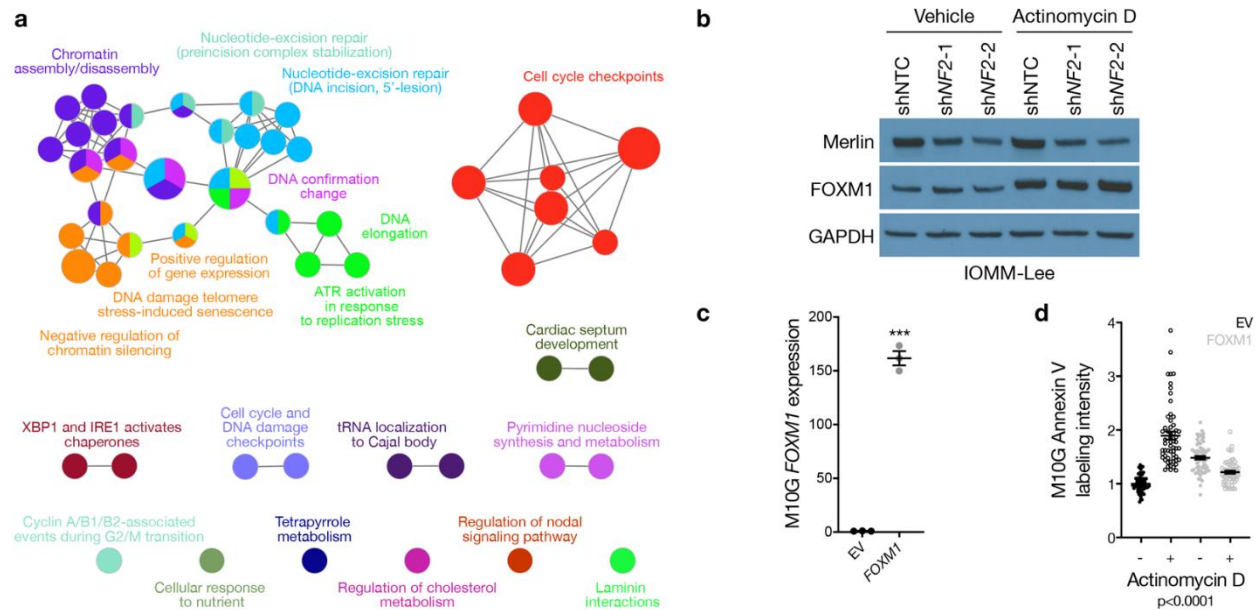
Figure S2.13 FOXM1 target gene functions in meningiomas and meningioma cells.

a, Predicted network of FOXM1-regulated pathways in Hypermitotic meningiomas based on H3K27ac ChIP sequencing of 25 meningiomas with matched RNA sequencing and DNA methylation profiling (15 Hypermitotic, 10 non-Hypermitotic)[7]. **b**, Immunoblot for Merlin, FOXM1, or GAPDH in IOMM-Lee meningioma cells stably expressing a non-targeting ontrol shRNA (shNTC) or shRNAs suppressing *NF2* (sh*NF2*-1 or sh*NF2*-2), after treatment with actinomycin D or vehicle control for 24 hours. **c**, QPCR for *FOXM1* in M10G meningioma cells over-expressing FOXM1 or empty vector (EV). *p≤0.0001 (Student's t test). **d**, Quantification of Annexin V confocal microscopy in M10G cells over-expressing FOXM1 or EV after treatment with actinomycin D or vehicle control for 24 hours (ANOVA). Lines represent means, and error bars represent standard error of the means.
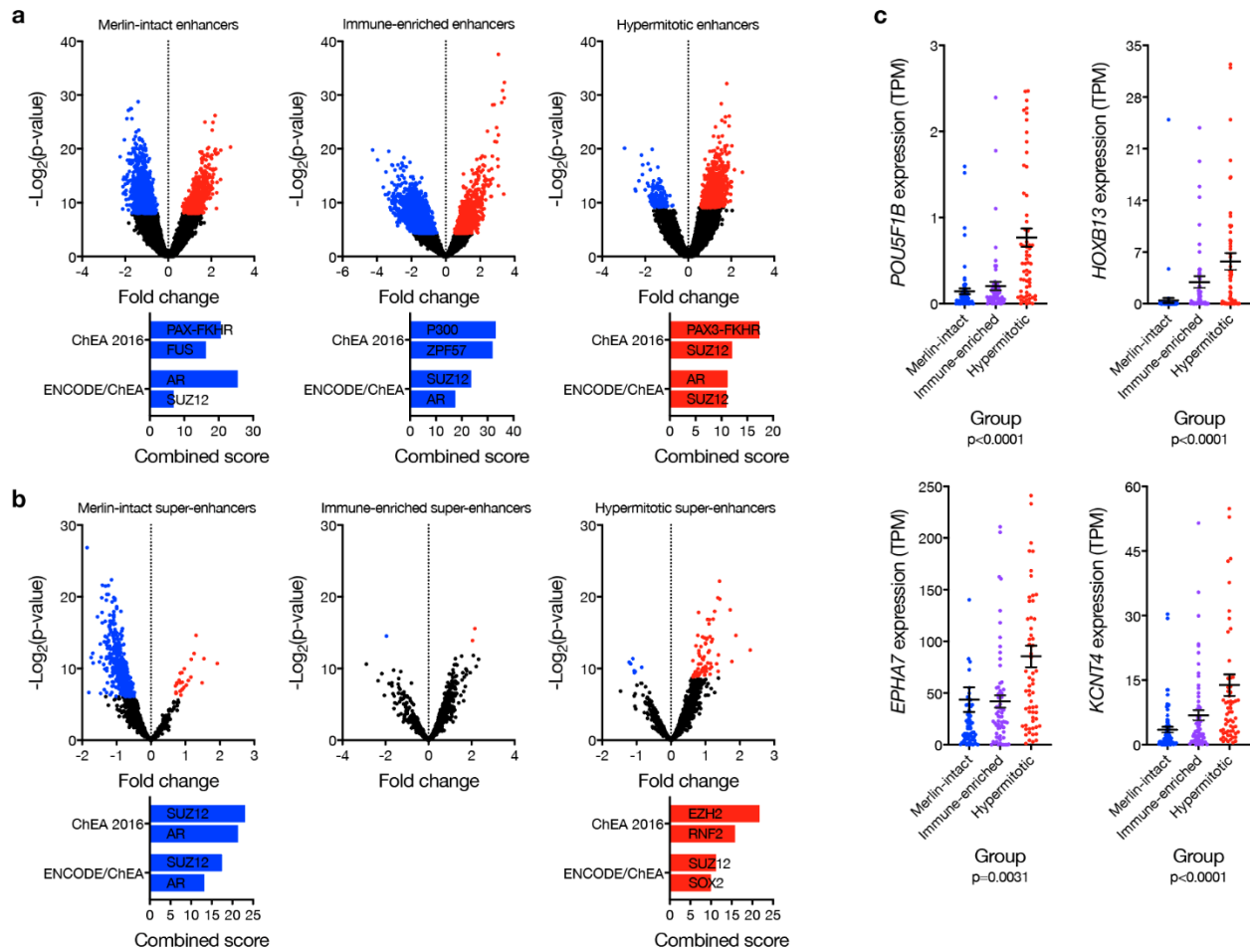
Figure S2.14 The enhancer landscape across meningioma DNA methylation groups.

a, Volcano plots of relative meningioma enhancer availability (n=25) across DNA methylation groups (top) from H3K27ac ChIP sequencing, and gene ontology analyses (bottom), of differentially enriched (red) or suppressed (blue) enhancers. ChEA, ChIP-X Enrichment Analysis. **b**, Volcano plots of meningioma relative super-enhancer expression (n=25) across DNA methylation groups (top), and gene ontology analyses (bottom), of differentially enriched (red) or suppressed (blue) super-enhancers. **c**, Meningioma transcripts per million (TPM) expression (n=200) of representative genes driving enhancer and super-enhancer ontologies from **a** and **b** across DNA methylation groups. Lines represent means, and error bars represent standard error of the means (ANOVA).
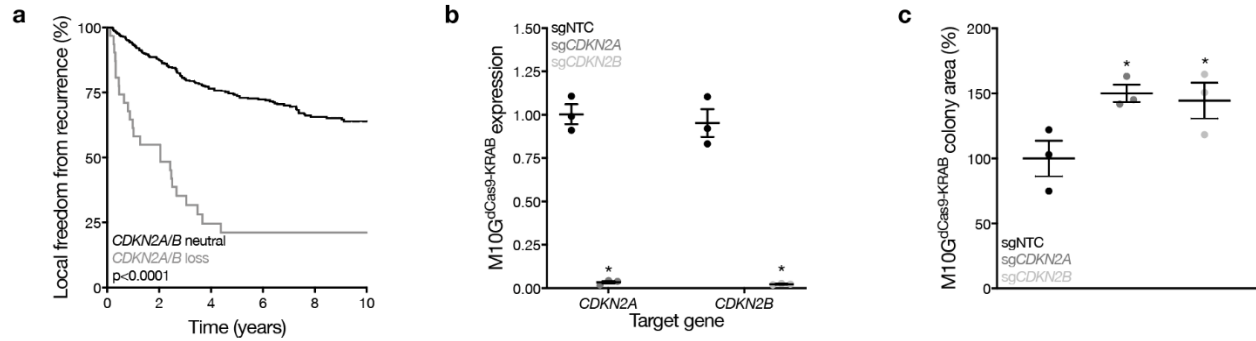
75

Figure S2.15 Loss of CDKN2A/B drives meningioma recurrence and meningioma cell proliferation.

a, Kaplan-Meier curve for meningioma local freedom from recurrence stratified by *CDKN2A/B* copy number status (n=565, Log-rank test). The number of samples with *CDKN2A/B* loss (n=37) prevented stratification across DNA methylation groups. **b**, QPCR for *CDKN2A* or *CDKN2B* in M10G$^{dCas9-KRAB}$ cells expressing a non-targeting control single-guide RNA (sgNTC), a single-guide RNA suppressing the p16^{INK4A} isoform of *CDKN2A* (sg*CDKN2A*), or a single-guide RNA suppressing *CDKN2B* (sg*CDKN2B*) (Student's t test). **c**, Relative colony area of M10G$^{dCas9-KRAB}$ cells expressing sgNTC, sg*CDKN2A*, or sg*CDKN2B* after 10 days of clonogenic growth (Student's t test). Lines represent means, and error bars represent standard error of the means. *p≤0.05.
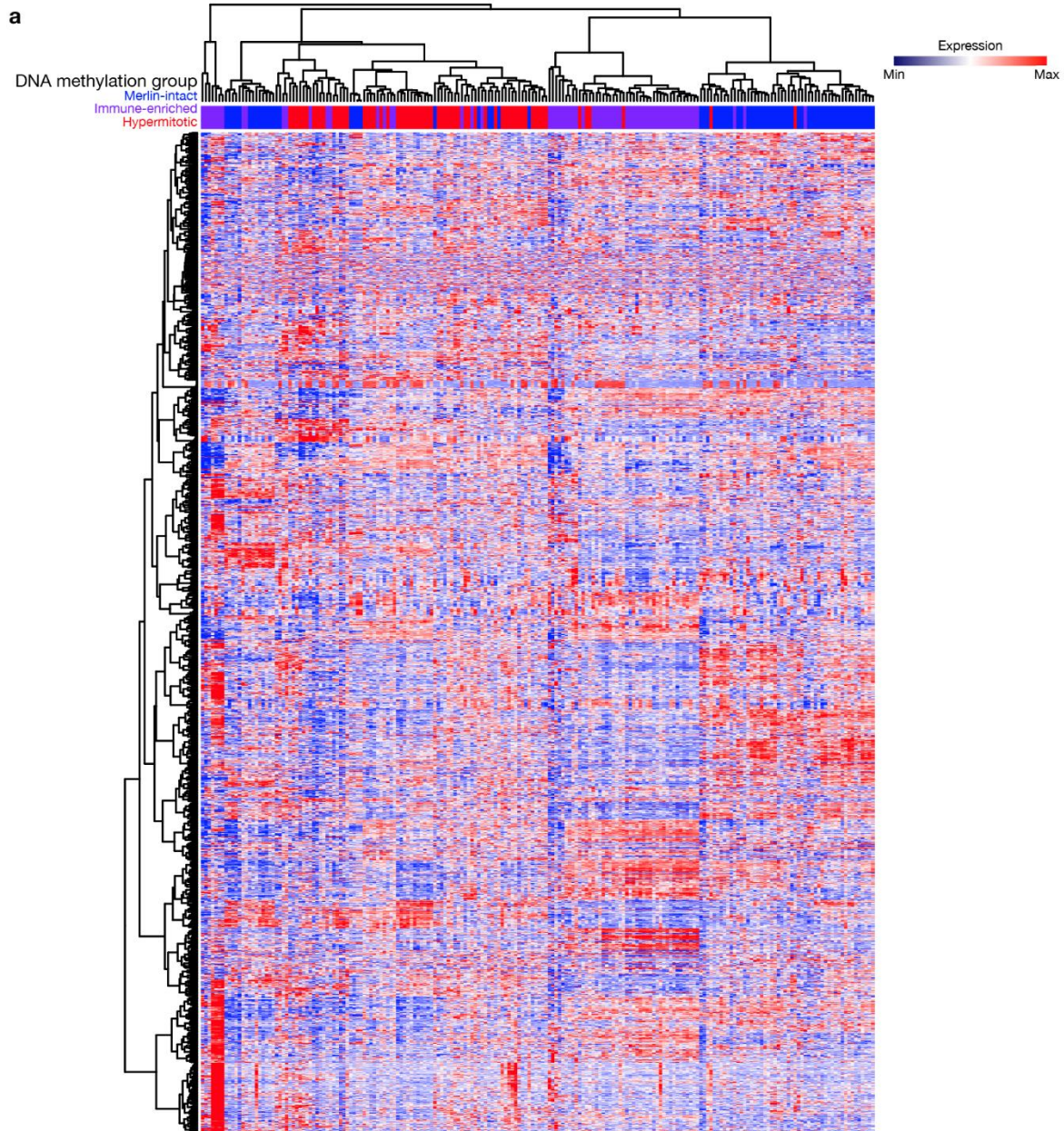
Figure S2.16 Meningioma DNA methylation groups are not distinguished by transcriptomes.

a, Unsupervised hierarchical clustering of meningiomas (n=200) using 2,000 differentially expressed genes. SeSAME meningioma DNA methylation groups are shown beneath the vertical dendrogram, and relative RNA-sequencing gene expression is visualized in the heatmap.
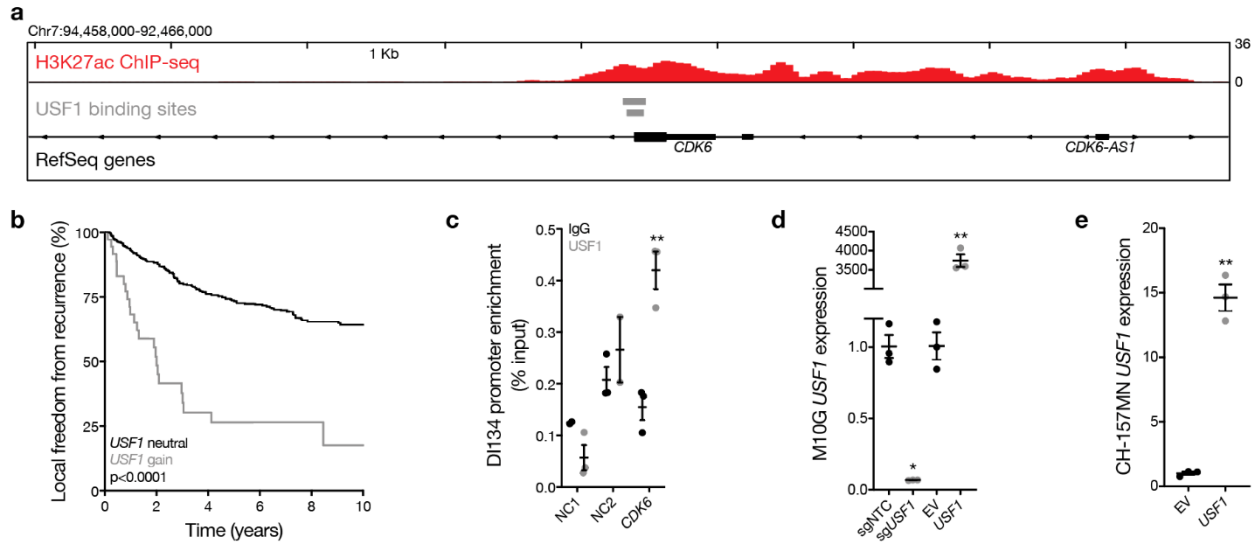
Figure S2.17 USF1 binds and activates the CDK6 promoter to drive meningioma recurrence and meningioma cell proliferation.

a, H3K27ac ChIP sequencing tracks of the *CDK6* locus in meningiomas (n=25) compared to normal neural cell and tissue samples (ChIP Atlas). **b**, Kaplan-Meier curve for meningioma local freedom from recurrence stratified by *USF1* copy number status (n=565, Log-rank test). The number of samples with *USF1* gain (n=42) prevented stratification across DNA methylation groups. **c**, ChIP-QPCR after USF1 pulldown in DI134 meningioma cells for the *CDK6* promoter (Student's t test) compared to negative control primers targeting a gene desert (NC1) or a gene not predicted to be bound by USF1 (NC2) from ChIP sequencing (Extended Data Table 10). **d**, QPCR for *USF1* in M10G[dCas9-KRAB] cells expressing sgNTC or a single-guide RNA suppressing *USF1* (sg*USF1*), or M10G cells over-expressing *USF1* or empty vector (EV) (Student's t test). **e**, QPCR for *USF1* in CH-157MN cells stably over-expressing USF1 or EV (Student's t test). Lines represent means, and error bars represent standard error of the means. *$p \leq 0.05$, **$p \leq 0.01$, ***$p \leq 0.0001$.
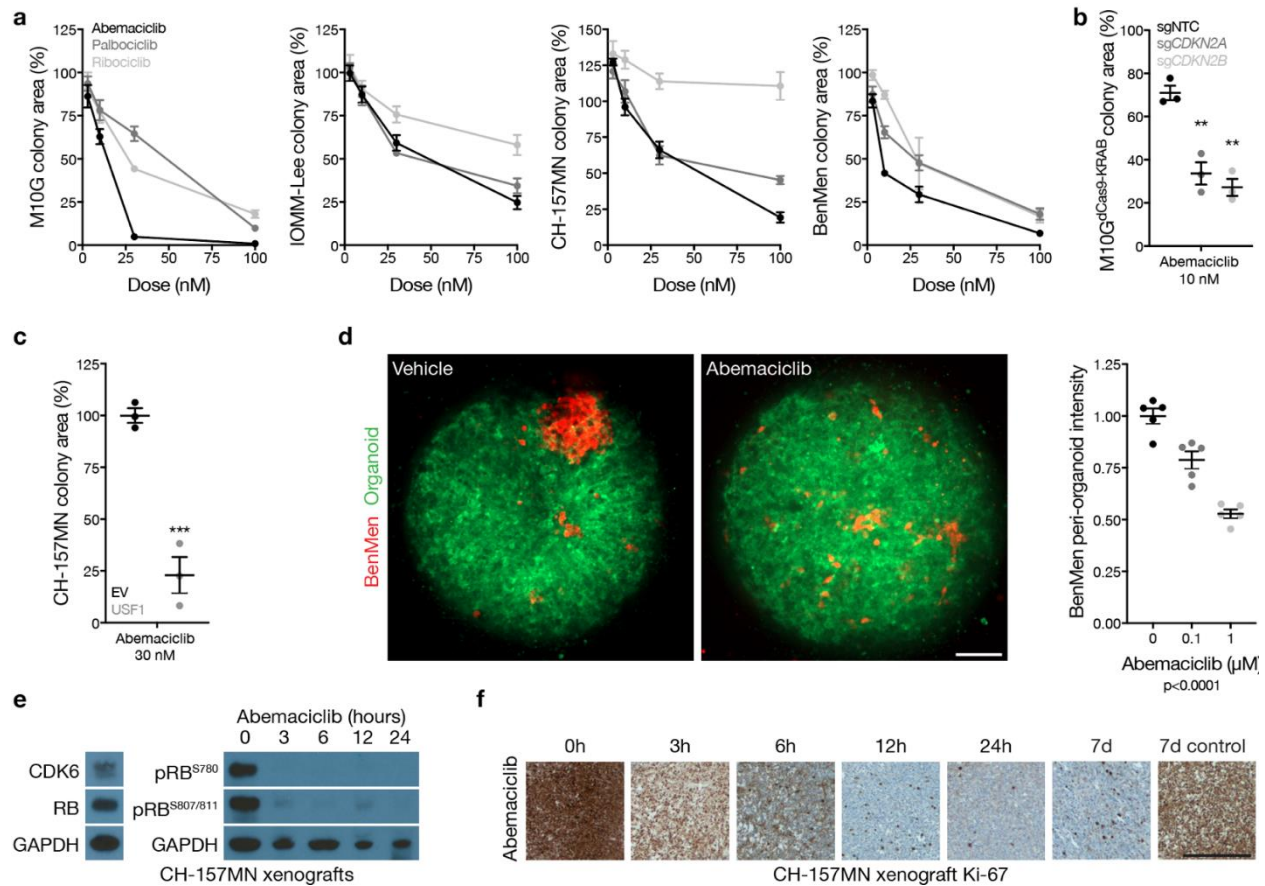
Figure S2.18 Cell cycle inhibition blocks meningioma growth in cells, organoids, and xenografts.

a, Relative colony area of M10G, BenMen, CH-157MN, or IOMM-Lee meningioma cells after 10 days of clonogenic growth and treatment with abemaciclib, ribociclib, or palbociclib. **b**, Relative colony area of M10G$^{dCas9-KRAB}$ cells expressing sgNTC, sg*CDKN2A*, or sg*CDKN2B* after 10 days of clonogenic growth and treatment with abemaciclib (Student's t test). Data are normalized to growth with vehicle treatment of each cell lines. **c**, Relative colony area of CH-157MN cells stably over-expressing USF or empty vector (EV) after 10 days of clonogenic growth and treatment with abemaciclib (Student's t test). Data are normalized to growth with vehicle treatment of each cell lines. **d**, Quantification of BenMen peri-organoid intensity after 10 days of growth and treatment with abemaciclib or vehicle control (ANOVA). Representative images of meningioma (red) and organoid (green) cells are shown. Scale bar 100 μM. **e**, Representative immunoblots from CH-157MN xenografts in NU/NU mice (left) harvested at intervals after a single treatment of abemaciclib (100 μg/g) via oral gavage (right). **f**, Representative images of CH-157MN xenograft Ki-67 immunohistochemistry after a daily treatment of abemaciclib or control. Scale bar 1 mm. Lines represent means, and error bars represent standard error of the means. **p$\leq$0.01.

a

Axial brain MRI

WHO grade 1

Ki-67 labeling index 7%
NF2 heterozygous loss, c1439C>T, and p.T480M
1p, 2q, 12q, 18p and 22q loss

b

Axial brain MRI

WHO grade 3

Ki-67 labeling index 20%
NF2 heterozygous loss and p.Q165*
CDKN2A/B homozygous loss
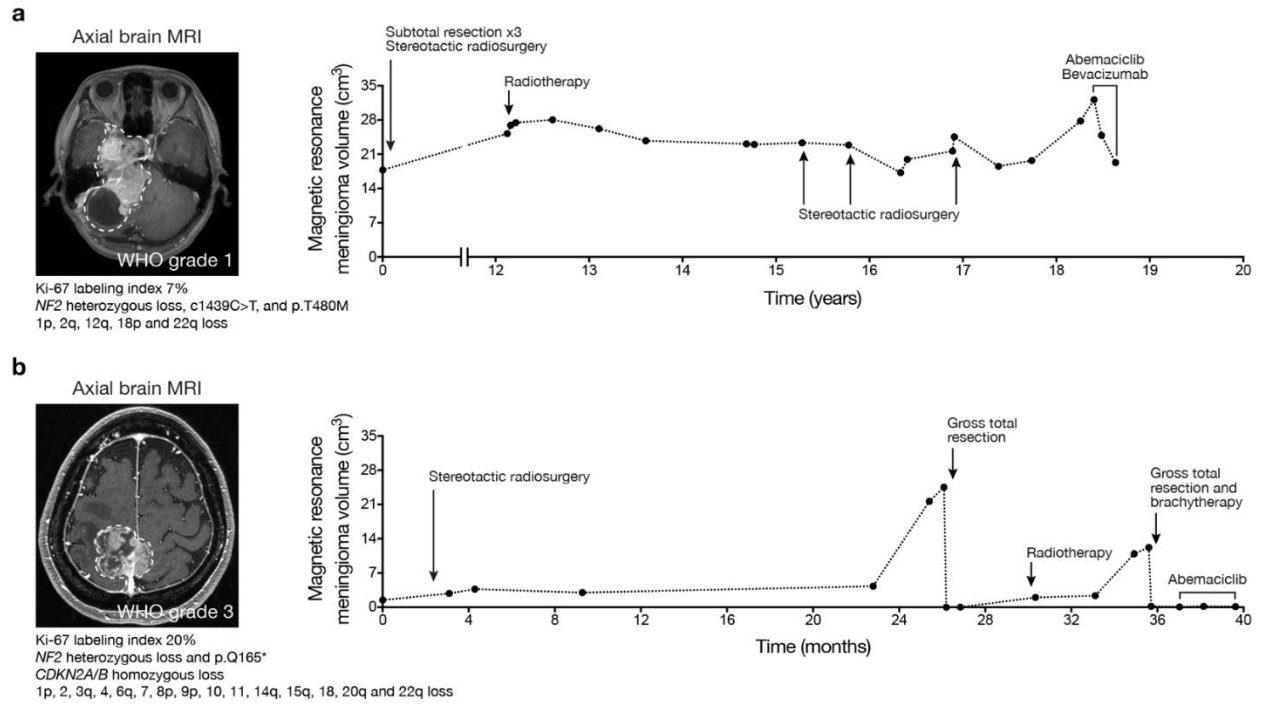1p, 2, 3q, 4, 6q, 7, 8p, 9p, 10, 11, 14q, 15q, 18, 20q and 22q loss

Figure S2.19 Cell cycle inhibition blocks meningioma growth in patients.

a, b, Magnetic resonance imaging and molecular features of meningiomas (left) that were resistant to cytotoxic therapies but responded to cytostatic cell cycle inhibition (right).

a Clinical features plus DNA methylation groups

b
n=565
34% Merlin-intact
38% Immune-enriched
28% Hypermitotic

22q intact or gain / 22q loss

n=275
59% Merlin-intact
26% Immune-enriched
15% Hypermitotic

n=290
10% Merlin-intact
50% Immune-enriched
40% Hypermitotic

1p intact / 1p loss

CNV1 n=223
64% Merlin-intact
30% Immune-enriched
6% Hypermitotic

CNV3 n=52
35% Merlin-intact
5% Immune-enriched
60% Hypermitotic

1p intact / 1p loss

n=205
8% Merlin-intact
62% Immune-enriched
30% Hypermitotic

CNV3 n=85
19% Merlin-intact
12% Immune-enriched
69% Hypermitotic

14q intact / 14q loss or gain

CNV2 n=168
6% Merlin-intact
77% Immune-enriched
17% Hypermitotic

CNV3 n=37
14% Merlin-intact
11% Immune-enriched
76% Hypermitotic

c Clinical features plus CNV groups

d CNV group p<0.0001

e

f Clinical features

81

Figure S2.20 Prognostic models for meningioma recurrence.

a, Comparison of observed and predicted 5-year local freedom from recurrence (LFFR) from a model incorporating clinical features and DNA methylation groups (Fig. 5e). Blue asterisks on the calibration curve denote the bootstrap optimism-corrected estimated probabilities. Lines represent means, and error bars represent standard error of the means. **b**, Recursive partitioning analysis of meningiomas (n=565) by CNVs reveals 3 CNV groups. **c**, Comparison of observed and predicted 5-year LFFR from a model incorporating clinical features and CNV groups (left, n=201), used to generate a nomogram for meningioma 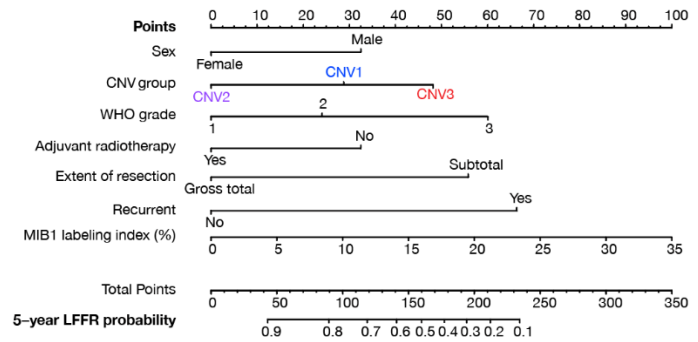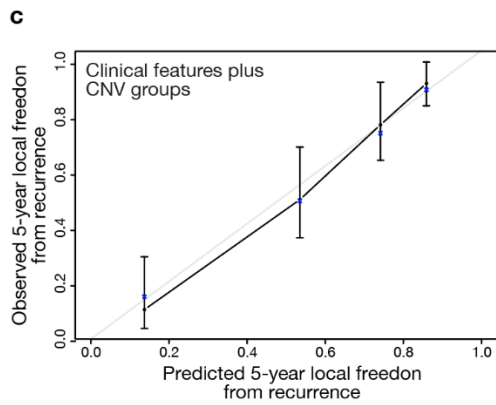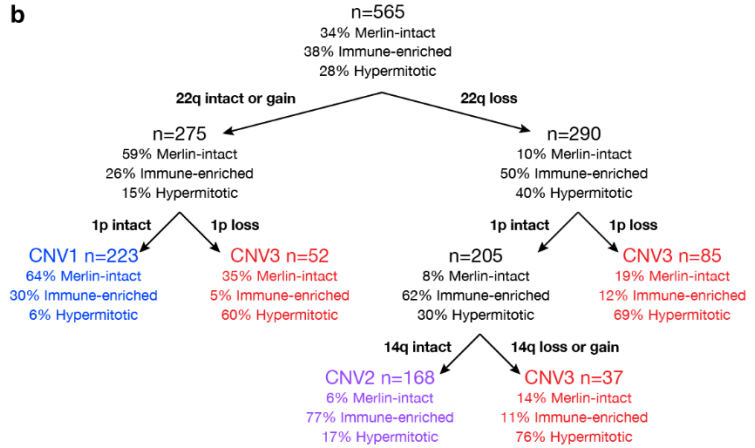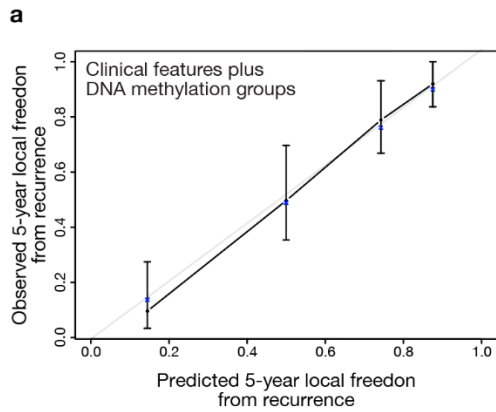LFFR (right, https://william-c-chen.shinyapps.io/RaleighLab_CNVSubgroupNomogram/). Variables contribute points (top row), which estimate the probably of 5-year LFFR (bottom rows). **d**, Meningioma DNA methylation groups and WHO grades (n=565) across CNV groups (Chi-squared tests). **e**, Kaplan-Meier curves for meningioma local freedom from recurrence and overall survival (n=565) comparing DNA methylation and CNV groups. **f**, Comparison of observed and predicted 5-year LFFR from a model incorporating clinical features (left, n=201), used to generate a nomogram for meningioma LFFR (right, https://william-c-chen.shinyapps.io/RaleighLab_ClinicalVariablesNomogram/).
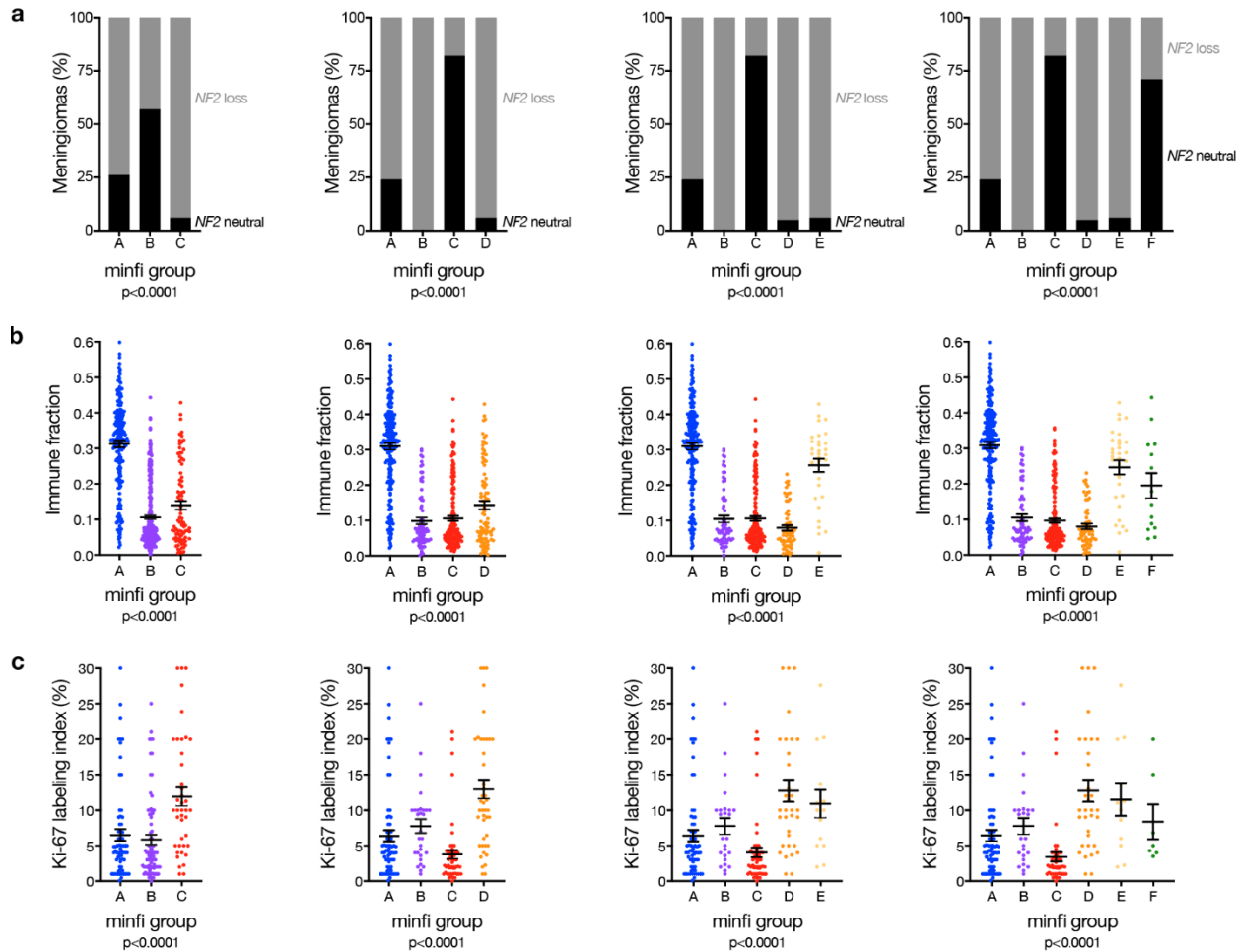
Figure S2.21 Meningioma DNA methylation analysis uncontrolled for CNV artifacts cannot identify a grouping scheme uniquely distinguished by NF2 status, immune enrichment, and proliferation.

a, Meningioma DNA methylation analysis of copy number loss at the *NF2* locus (n=565) across different numbers of DNA methylation groups determined by the minfi pre-processing pipeline (Chi-squared test). **b**, Meningioma DNA methylation estimation of leukocyte fraction (n=565) across different numbers of DNA methylation groups determined by the minfi pre-processing pipeline (ANOVA). **c**, Ki-67 labeling index from meningioma clinical pathology reports (n=206) across different numbers of DNA methylation groups determined by the minfi pre-processing pipeline (ANOVA). Regardless of the number of groups, meningioma DNA methylation analysis uncontrolled for CNV artifacts cannot identifying a grouping scheme with non-redundant differences in clinical outcomes (Extended Data Fig. 5c), *NF2* loss, immune enrichment, and cell proliferation. Lines represent means, and error bars represent standard error of the means.
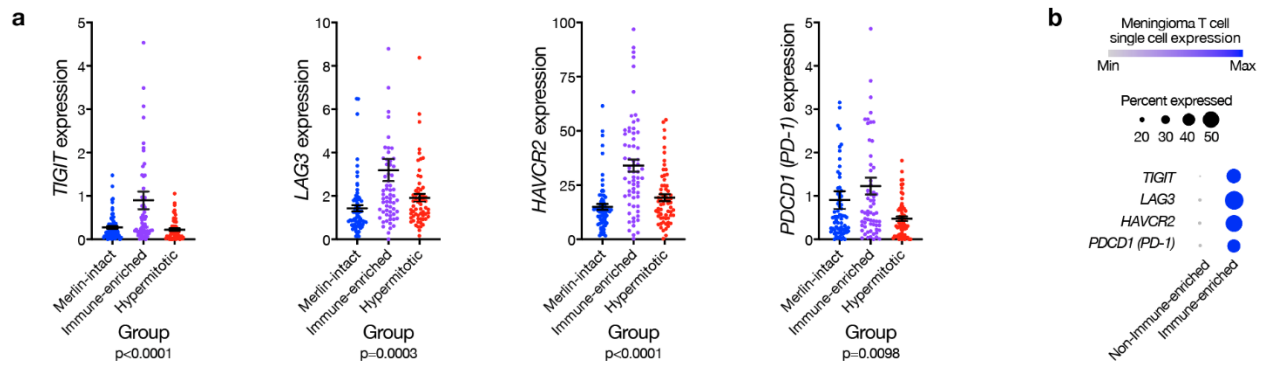
Figure S2.22 Meningioma intratumor T cells express markers of immune exhaustion.

a, Meningioma transcripts per million (TPM) expression of *TIGIT*, *LAG3*, *HAVCR2*, or *PDCD1* (n=200) T cell exhaustion markers across DNA methylation groups. Lines represent means, and error bars represent standard error of the means (ANOVA). **b**, Single-cell RNA sequencing relative expression of immune exhaustion genes in T cells across Immune-enriched (n=5) and non-Immune-enriched (n=3) meningioma samples. Circle size denotes percentage of cells. Circle shading denotes average expression.

References

1. Ostrom, Q. T. *et al.* CBTRUS Statistical Report: Primary Brain and Other Central Nervous System Tumors Diagnosed in the United States in 2012–2016. *Neuro-Oncol.* **21**, v1–v100 (2019).

2. Brastianos, P. K. *et al.* Advances in multidisciplinary therapy for meningiomas. *Neuro-Oncol.* **21**, i18–i31 (2019).

3. Wen, P. Y., Quant, E., Drappatz, J., Beroukhim, R. & Norden, A. D. Medical therapies for meningiomas. *J. Neurooncol.* **99**, 365–378 (2010).

4. Capper, D. *et al.* DNA methylation-based classification of central nervous system tumours. *Nature* **555**, 469–474 (2018).

5. Sahm, F. *et al.* DNA methylation-based classification and grading system for meningioma: a multicentre, retrospective analysis. *Lancet Oncol.* **18**, 682–694 (2017).

6. Olar, A. *et al.* Global epigenetic profiling identifies methylation subgroups associated with recurrence-free survival in meningioma. *Acta Neuropathol. (Berl.)* **133**, 431–444 (2017).

7. Nassiri, F. *et al.* DNA methylation profiling to predict recurrence risk in meningioma: development and validation of a nomogram to optimize clinical management. *Neuro-Oncol.* (2019) doi:10.1093/neuonc/noz061.

8. Vasudevan, H. N. *et al.* Comprehensive Molecular Profiling Identifies FOXM1 as a Key Transcription Factor for Meningioma Proliferation. *Cell Rep.* **22**, 3672–3683 (2018).

9. Harmancı, A. S. *et al.* Integrated genomic analyses of de novo pathways underlying atypical meningiomas. *Nat. Commun.* **8**, 14433 (2017).

10. Bi, W. L. *et al.* Genomic landscape of intracranial meningiomas. *J. Neurosurg.* **125**, 525–535 (2016).

11. Zhou, W., Triche, T. J., Laird, P. W. & Shen, H. SeSAMe: reducing artifactual detection of DNA methylation by Infinium BeadChips in genomic deletions. *Nucleic Acids Res.* **46**, e123–e123 (2018).

12. Aryee, M. J. *et al.* Minfi: a flexible and comprehensive Bioconductor package for the analysis of Infinium DNA methylation microarrays. *Bioinformatics* **30**, 1363–1369 (2014).

13. Evans, Dg. R. Neurofibromatosis type 2 (NF2): A clinical and molecular review. *Orphanet J. Rare Dis.* **4**, 1–11 (2009).

14. Clark, V. E. *et al.* Genomic analysis of non-NF2 meningiomas reveals mutations in TRAF7, KLF4, AKT1, and SMO. *Science* **339**, 1077–1080 (2013).

15. Brastianos, P. K. *et al.* Genomic sequencing of meningiomas identifies oncogenic SMO and AKT1 mutations. *Nat. Genet.* **45**, 285–289 (2013).

16. Youngblood, M. W. *et al.* Correlations between genomic subgroup and clinical features in a cohort of more than 3000 meningiomas. *J. Neurosurg.* **1**, 1–10 (2019).

17. Agnihotri, S. *et al.* Therapeutic radiation for childhood cancer drives structural aberrations of NF2 in meningiomas. *Nat. Commun.* **8**, 186 (2017).

18. Sahm, F. *et al.* Meningiomas induced by low-dose radiation carry structural variants of NF2 and a distinct mutational signature. *Acta Neuropathol. (Berl.)* **134**, 155–158 (2017).

19. Reuss, D. E. *et al.* Secretory meningiomas are defined by combined KLF4 K409Q and TRAF7 mutations. *Acta Neuropathol. (Berl.)* **125**, 351–358 (2013).

20. Sahm, F. *et al.* AKT1E17K mutations cluster with meningothelial and transitional meningiomas and can be detected by SFRP1 immunohistochemistry. *Acta Neuropathol. (Berl.)* **126**, 757–762 (2013).

21. Findakly, S. *et al.* Meningioma cells express primary cilia but do not transduce ciliary Hedgehog signals. *Acta Neuropathol. Commun.* **8**, 114 (2020).

22. Curto, M., Cole, B. K., Lallemand, D., Liu, C.-H. & McClatchey, A. I. Contact-dependent inhibition of EGFR signaling by Nf2/Merlin. *J. Cell Biol.* **177**, 893–903 (2007).

23. Chiasson-MacKenzie, C. *et al.* NF2/Merlin mediates contact-dependent inhibition of EGFR mobility and internalization via cortical actomyosin. *J Cell Biol* **211**, 391–405 (2015).

24. Li, W. *et al.* Merlin/NF2 Suppresses Tumorigenesis by Inhibiting the E3 Ubiquitin Ligase CRL4DCAF1 in the Nucleus. *Cell* **140**, 477–490 (2010).

25. Magill, S. T. *et al.* Multiplatform genomic profiling and magnetic resonance imaging identify mechanisms underlying intratumor heterogeneity in meningioma. *Nat. Commun.* **11**, 4803 (2020).

26. Lee, W. H. Characterization of a newly established malignant meningioma cell line of the human brain: IOMM-Lee. *Neurosurgery* **27**, 389–395; discussion 396 (1990).

27. Gilbert, L. A. *et al.* Genome-Scale CRISPR-Mediated Control of Gene Repression and Activation. *Cell* **159**, 647–661 (2014).

28. Yeo, N. C. *et al.* An enhanced CRISPR repressor for targeted mammalian gene regulation. *Nat. Methods* **15**, 611–616 (2018).

29.   Tsai, J.-C., Goldman, C. K. & Gillespie, G. Y. Vascular endothelial growth factor in human glioma cell lines: induced secretion by EGF, PDGF-BB, and bFGF. *J. Neurosurg.* **82**, 864–873 (1995).

30.   Lobingier, B. T. *et al.* An Approach to Spatiotemporally Resolve Protein Interaction Networks in Living Cells. *Cell* **169**, 350-360.e12 (2017).

31.   LeClerc, S., Palaniswami, R., Xie, B. X. & Govindan, M. V. Molecular cloning and characterization of a factor that binds the human glucocorticoid receptor gene and represses its expression. *J. Biol. Chem.* **266**, 17333–17340 (1991).

32.   Leclerc, S., Xie, B. X., Roy, R. & Govindan, M. V. Purification of a human glucocorticoid receptor gene promoter-binding protein. Production of polyclonal antibodies against the purified factor. *J. Biol. Chem.* **266**, 8711–8719 (1991).

33.   Flammer, J. R. *et al.* The type I interferon signaling pathway is a target for glucocorticoid inhibition. *Mol. Cell. Biol.* **30**, 4564–4574 (2010).

34.   Ballegeer, M. *et al.* Glucocorticoid receptor dimers control intestinal STAT1 and TNF-induced inflammation in mice. *J. Clin. Invest.* **128**, 3265–3279 (2018).

35.   Aran, D., Hu, Z. & Butte, A. J. xCell: digitally portraying the tissue cellular heterogeneity landscape. *Genome Biol.* **18**, 220 (2017).

36.   Benelli, M., Romagnoli, D. & Demichelis, F. Tumor purity quantification by clonal DNA methylation signatures. *Bioinforma. Oxf. Engl.* **34**, 1642–1649 (2018).

37.   Müller, S., Cho, A., Liu, S. J., Lim, D. A. & Diaz, A. CONICS integrates scRNA-seq with DNA sequencing to map gene expression to tumor sub-clones. *Bioinforma. Oxf. Engl.* **34**, 3217–3219 (2018).

38.   McGranahan, N. *et al.* Allele-Specific HLA Loss and Immune Escape in Lung Cancer Evolution. *Cell* **171**, 1259-1271.e11 (2017).

39.   Frye, M. *et al.* Matrix stiffness controls lymphatic vessel formation through regulation of a GATA2-dependent transcriptional program. *Nat. Commun.* **9**, 1511 (2018).

40.   Zhang, X., Groopman, J. E. & Wang, J. F. Extracellular matrix regulates endothelial functions through interaction of VEGFR-3 and integrin alpha5beta1. *J. Cell. Physiol.* **202**, 205–214 (2005).

41.   Vaahtomeri, K., Karaman, S., Mäkinen, T. & Alitalo, K. Lymphangiogenesis guidance by paracrine and pericellular factors. *Genes Dev.* **31**, 1615–1634 (2017).

42.   Wiig, H., Keskin, D. & Kalluri, R. Interaction between the extracellular matrix and lymphatics: consequences for lymphangiogenesis and lymphatic function. *Matrix Biol. J. Int. Soc. Matrix Biol.* **29**, 645–656 (2010).

43.   Louveau, A. *et al.* Structural and functional features of central nervous system lymphatic vessels. *Nature* **523**, 337–341 (2015).

44.   Antila, S. *et al.* Development and plasticity of meningeal lymphatic vessels. *J. Exp. Med.* **214**, 3645–3667 (2017).

45.   Ahn, J. H. *et al.* Meningeal lymphatic vessels at the skull base drain cerebrospinal fluid. *Nature* **572**, 62–66 (2019).

46.   Hu, X. *et al.* Meningeal lymphatic vessels regulate brain tumor drainage and immunity. *Cell Res.* **30**, 229–243 (2020).

47.   Rustenhoven, J. *et al.* Functional characterization of the dural sinuses as a neuroimmune interface. *Cell* **0**, (2021).

48.   Banerji, S. *et al.* LYVE-1, a New Homologue of the CD44 Glycoprotein, Is a Lymph-specific Receptor for Hyaluronan. *J. Cell Biol.* **144**, 789–801 (1999).

49.   Noor, S. & Wilson, E. H. Role of C-C chemokine receptor type 7 and its ligands during neuroinflammation. *J. Neuroinflammation* **9**, 77 (2012).

50.   Wigle, J. T. *et al.* An essential role for Prox1 in the induction of the lymphatic endothelial cell phenotype. *EMBO J.* **21**, 1505–1513 (2002).

51.   Louis, D. N. *et al.* The 2016 World Health Organization Classification of Tumors of the Central Nervous System: a summary. *Acta Neuropathol. (Berl.)* **131**, 803–820 (2016).

52.   Rogers, L. *et al.* Meningiomas: knowledge base, treatment outcomes, and uncertainties. A RANO review. *J. Neurosurg.* **122**, 4–23 (2015).

53.   Paramasivam, N. *et al.* Mutational patterns and regulatory networks in epigenetic subgroups of meningioma. *Acta Neuropathol. (Berl.)* **138**, 295–308 (2019).

54.   Chen, W. C. *et al.* A Prognostic Gene-Expression Signature and Risk Score for Meningioma Recurrence After Resection. *Neurosurgery* (2020) doi:10.1093/neuros/nyaa355.

55.   de Olano, N. *et al.* The p38 MAPK-MK2 axis regulates E2F1 and FOXM1 expression after epirubicin treatment. *Mol. Cancer Res. MCR* **10**, 1189–1202 (2012).

56.   Prager, B. C. *et al.* The Meningioma Enhancer Landscape Delineates Novel Subgroups and Drives Druggable Dependencies. *Cancer Discov.* (2020) doi:10.1158/2159-8290.CD-20-0160.

57.   Clark, V. E. *et al.* Recurrent somatic mutations in POLR2A define a distinct subset of meningiomas. *Nat. Genet.* **48**, 1253–1259 (2016).

58.	Sievers, P. *et al.* YAP1-fusions in pediatric NF2-wildtype meningioma. *Acta Neuropathol. (Berl.)* **139**, 215–218 (2020).

59.	Williams, E. A. *et al.* Distinct genomic subclasses of high-grade/progressive meningiomas: NF2-associated, NF2-exclusive, and NF2-agnostic. *Acta Neuropathol. Commun.* **8**, 171 (2020).

60.	Youngblood, M. W. *et al.* Associations of Meningioma Molecular Subgroup and Tumor Recurrence. *Neuro-Oncol.* (2020) doi:10.1093/neuonc/noaa226.

61.	Sahm, F. *et al.* TERT Promoter Mutations and Risk of Recurrence in Meningioma. *J. Natl. Cancer Inst.* **108**, (2016).

62.	Spiegl-Kreinecker, S. *et al.* TERT promoter mutations are associated with poor prognosis and cell immortalization in meningioma. *Neuro-Oncol.* **20**, 1584 (2018).

63.	Shankar, G. M. & Santagata, S. BAP1 mutations in high-grade meningioma: implications for patient care. *Neuro-Oncol.* **19**, 1447 (2017).

64.	Guyot, A. *et al.* Analysis of CDKN2A gene alterations in recurrent and non-recurrent meningioma. *J. Neurooncol.* **145**, 449–459 (2019).

65.	Shoshani, O. *et al.* Chromothripsis drives the evolution of gene amplification in cancer. *Nature* 1–5 (2020) doi:10.1038/s41586-020-03064-z.

66.	Cohen-Sharir, Y. *et al.* Aneuploidy renders cancer cells vulnerable to mitotic checkpoint inhibition. *Nature* **590**, 486–491 (2021).

67.	Quinton, R. J. *et al.* Whole-genome doubling confers unique genetic vulnerabilities on tumour cells. *Nature* **590**, 492–497 (2021).

68.	Appay, R. *et al.* CDKN2A homozygous deletion is a strong adverse prognosis factor in diffuse malignant IDH-mutant gliomas. *Neuro-Oncol.* **21**, 1519–1528 (2019).

69.   Merlo, A. *et al.* 5′ CpG island methylation is associated with transcriptional silencing of the tumour suppressor p16/CDKN2/MTS1 in human cancers. *Nat. Med.* **1**, 686–692 (1995).

70.   Herman, J. G. *et al.* Distinct Patterns of Inactivation of p15INK4B and p16INK4A Characterize the Major Types of Hematological Malignancies. *Cancer Res.* **57**, 837–841 (1997).

71.   Levine, A. J., Jenkins, N. A. & Copeland, N. G. The Roles of Initiating Truncal Mutations in Human Cancers: The Order of Mutations and Tumor Cell Type Matters. *Cancer Cell* **35**, 10–15 (2019).

72.   Tien, A.-C. *et al.* MNGI-01. A PHASE 0 TRIAL OF RIBOCICLIB IN AGGRESSIVE MENINGIOMA PATIENTS INCORPORATING A TUMOR PHARMACODYNAMIC- AND PHARMACOKINETIC-GUIDED EXPANSION COHORT. *Neuro-Oncol.* **21**, vi139 (2019).

73.   Iasonos, A., Schrag, D., Raj, G. V. & Panageas, K. S. How to build and interpret a nomogram for cancer prognosis. *J. Clin. Oncol. Off. J. Am. Soc. Clin. Oncol.* **26**, 1364–1370 (2008).

74.   Anderson, A. C., Joller, N. & Kuchroo, V. K. Lag-3, Tim-3, and TIGIT: Co-inhibitory Receptors with Specialized Functions in Immune Regulation. *Immunity* **44**, 989–1004 (2016).

75.   Pagès, F. *et al.* Immune infiltration in human tumors: a prognostic factor that should not be ignored. *Oncogene* **29**, 1093–1102 (2010).

76.   Louis, D., Ohgaki, H., Wiestler, O. & Cavenee, W. *WHO Classification of Tumours of the Central Nervous System.* (2016).

77.   Fortin, J.-P. *et al.* Functional normalization of 450k methylation array data improves replication in large cancer studies. *Genome Biol.* **15**, 1–17 (2014).

78.   Pidsley, R. *et al.* Critical evaluation of the Illumina MethylationEPIC BeadChip microarray for whole-genome DNA methylation profiling. *Genome Biol.* **17**, 1–17 (2016).

79.   Wilkerson, M. D. & Hayes, D. N. ConsensusClusterPlus: a class discovery tool with confidence assessments and item tracking. *Bioinformatics* **26**, 1572–1573 (2010).

80.   Kline, C. N. *et al.* Targeted next-generation sequencing of pediatric neuro-oncology patients improves diagnosis, identifies pathogenic germline mutations, and directs targeted therapy. *Neuro-Oncol.* **19**, 699–709 (2017).

81.   Li, H. & Durbin, R. Fast and accurate short read alignment with Burrows-Wheeler transform. *Bioinforma. Oxf. Engl.* **25**, 1754–1760 (2009).

82.   DePristo, M. A. *et al.* A framework for variation discovery and genotyping using next-generation DNA sequencing data. *Nat. Genet.* **43**, 491–498 (2011).

83.   McKenna, A. *et al.* The Genome Analysis Toolkit: a MapReduce framework for analyzing next-generation DNA sequencing data. *Genome Res.* **20**, 1297–1303 (2010).

84.   Talevich, E., Shain, A. H., Botton, T. & Bastian, B. C. CNVkit: Genome-Wide Copy Number Detection and Visualization from Targeted DNA Sequencing. *PLoS Comput. Biol.* **12**, e1004873 (2016).

85.   Bolger, A. M., Lohse, M. & Usadel, B. Trimmomatic: a flexible trimmer for Illumina sequence data. *Bioinforma. Oxf. Engl.* **30**, 2114–2120 (2014).

86.   Schneider, V. A. *et al.* Evaluation of GRCh38 and de novo haploid genome assemblies demonstrates the enduring quality of the reference assembly. *Genome Res.* **27**, 849–864 (2017).

87.   Kim, D., Paggi, J. M., Park, C., Bennett, C. & Salzberg, S. L. Graph-based genome alignment and genotyping with HISAT2 and HISAT-genotype. *Nat. Biotechnol.* **37**, 907–915 (2019).

88.   Liao, Y., Smyth, G. K. & Shi, W. featureCounts: an efficient general purpose program for assigning sequence reads to genomic features. *Bioinforma. Oxf. Engl.* **30**, 923–930 (2014).

89.   Love, M. I., Huber, W. & Anders, S. Moderated estimation of fold change and dispersion for RNA-seq data with DESeq2. *Genome Biol.* **15**, 550 (2014).

90.   Zhu, A., Ibrahim, J. G. & Love, M. I. Heavy-tailed prior distributions for sequence count data: removing the noise and preserving large differences. *Bioinformatics* **35**, 2084–2092 (2019).

91.   Chen, E. Y. *et al.* Enrichr: interactive and collaborative HTML5 gene list enrichment analysis tool. *BMC Bioinformatics* **14**, 128 (2013).

92.   Kuleshov, M. V. *et al.* Enrichr: a comprehensive gene set enrichment analysis web server 2016 update. *Nucleic Acids Res.* **44**, W90-97 (2016).

93.   Rouillard, A. D. *et al.* The harmonizome: a collection of processed datasets gathered to serve and mine knowledge about genes and proteins. *Database J. Biol. Databases Curation* **2016**, (2016).

94.   Andrews, S. *FastQC.*

95. Langmead, B. & Salzberg, S. L. Fast gapped-read alignment with Bowtie 2. *Nat. Methods* **9**, 357–359 (2012).

96. Auwera, G. A. V. der *et al.* From FastQ Data to High-Confidence Variant Calls: The Genome Analysis Toolkit Best Practices Pipeline. *Curr. Protoc. Bioinforma.* **43**, 11.10.1-11.10.33 (2013).

97. Cingolani, P. *et al.* A program for annotating and predicting the effects of single nucleotide polymorphisms, SnpEff: SNPs in the genome of Drosophila melanogaster strain w1118; iso-2; iso-3. *Fly (Austin)* **6**, 80–92 (2012).

98. Cingolani, P. *et al.* Using Drosophila melanogaster as a Model for Genotoxic Chemical Mutational Studies with a New Program, SnpSift. *Front. Genet.* **3**, 35 (2012).

99. Püttmann, S. *et al.* Establishment of a benign meningioma cell line by hTERT-mediated immortalization. *Lab. Invest.* **85**, 1163 (2005).

100. Adamson, B. *et al.* A Multiplexed Single-Cell CRISPR Screening Platform Enables Systematic Dissection of the Unfolded Protein Response. *Cell* **167**, 1867-1882.e21 (2016).

101. Horlbeck, M. A. *et al.* Compact and highly active next-generation libraries for CRISPR-mediated gene repression and activation. *eLife* **5**, e19760 (2016).

102. Cox, J. & Mann, M. MaxQuant enables high peptide identification rates, individualized p.p.b.-range mass accuracies and proteome-wide protein quantification. *Nat. Biotechnol.* **26**, 1367–1372 (2008).

103. Prianichnikov, N. *et al.* MaxQuant Software for Ion Mobility Enhanced Shotgun Proteomics. *Mol. Cell. Proteomics MCP* **19**, 1058–1069 (2020).

104. Shukla, S. A. *et al.* Comprehensive analysis of cancer-associated somatic mutations in class I HLA genes. *Nat. Biotechnol.* **33**, 1152–1158 (2015).

105. Cao, H. *et al.* An integrated tool to study MHC region: accurate SNV detection and HLA genes typing in human MHC region using targeted high-throughput sequencing. *PloS One* **8**, e69388 (2013).

106. Butler, A., Hoffman, P., Smibert, P., Papalexi, E. & Satija, R. Integrating single-cell transcriptomic data across different conditions, technologies, and species. *Nat. Biotechnol.* **36**, 411–420 (2018).

107. Stuart, T. *et al.* Comprehensive Integration of Single-Cell Data. *Cell* **177**, 1888-1902.e21 (2019).

108. Hafemeister, C. & Satija, R. Normalization and variance stabilization of single-cell RNA-seq data using regularized negative binomial regression. *Genome Biol.* **20**, 296 (2019).

109. Korsunsky, I. *et al.* Fast, sensitive and accurate integration of single-cell data with Harmony. *Nat. Methods* **16**, 1289–1296 (2019).

110. Tirosh, I. *et al.* Dissecting the multicellular ecosystem of metastatic melanoma by single-cell RNA-seq. *Science* **352**, 189–196 (2016).

111. Newman, A. M. *et al.* Determining cell type abundance and expression from bulk tissues with digital cytometry. *Nat. Biotechnol.* **37**, 773–782 (2019).

112. Whyte, W. A. *et al.* Master Transcription Factors and Mediator Establish Super-Enhancers at Key Cell Identity Genes. *Cell* **153**, 307–319 (2013).

113. Lovén, J. *et al.* Selective Inhibition of Tumor Oncogenes by Disruption of Super-Enhancers. *Cell* **153**, 320–334 (2013).

114. Bindea, G. *et al.* ClueGO: a Cytoscape plug-in to decipher functionally grouped gene ontology and pathway annotation networks. *Bioinformatics* **25**, 1091–1093 (2009).

115. Shannon, P. *et al.* Cytoscape: A Software Environment for Integrated Models of Biomolecular Interaction Networks. *Genome Res.* **13**, 2498–2504 (2003).

116. Schoenfeld, D. Partial residuals for the proportional hazards regression model. *Biometrika* **69**, 239–241 (1982).

117. Breiman, L. Random Forests. *Mach. Learn.* **45**, 5–32 (2001).

118. Song, X. & Zhou, X.-H. A SEMIPARAMETRIC APPROACH FOR THE COVARIATE SPECIFIC ROC CURVE WITH SURVIVAL OUTCOME. *Stat. Sin.* **18**, 947–965 (2008).

119. Hastie, T., Tibshirani, R. & Friedman, J. *The Elements of Statistical Learning: Data Mining, Inference, and Prediction.* (2009).

Chapter 3: Characterization of Notch3+ perivascular cells in meningioma

Introduction

Background

Reductionist laboratory model systems are critical for investigating mechanisms of tumor initiation and growth, as well as for preclinical testing of new therapies. Ideally, cancer models are able to recapitulate the histopathology, genetics and tumor microenvironment of human diseases, and can be broadly divided into *in vitro* and *in vivo* categories. *In vitro* models consist of cell lines grown in conditioned media outside of an organism. In contrast, *in vivo* models rely on tumor growth in animals to approximate human pathophysiology. While *in vitro* models often fail to recapitulate intratumor heterogeneity and cancer cell interactions with the immune system, they are typically easier to manipulate and test in a high-throughput fashion compared to *in vivo* systems. Numerous *in vitro* and *in vivo* models have been developed to study meningioma biology, but many of these models have significant limitations, leaving an unmet need in our ability to study and understand meningioma.

Cell Culture

Cell lines are populations of cells that can, ideally, divide and be maintained indefinitely when cultured *in vitro*. Many human meningioma cell lines have been derived from resected patient tumors, and some of the more prevalent meningioma cell systems are listed in Table 3.1. *NF2* status is particularly important in models of meningioma because *NF2* loss is the most common genetic alteration in meningioma[1] and is thought to be fundamental for meningioma oncogenesis. Meningioma cell lines have been derived from a variety of tumors, ranging in location, patient gender, patient age and *NF2* status.

Yet the available meningioma cell lines remain small in number, are incompletely characterized and can be difficult to culture. The most commonly used and cited amongst these is Ben-Men-1, a cell line derived from a benign Grade I meningioma that was subsequently immortalized through hTERT transduction[2].

In addition to specific problems, such as lack of characterization or unverified immortality of many specific meningioma cell lines, all suffer from limitations that are intrinsic to *in vitro* systems, such as (i) 2D cell culture conditions that are very different from the tumor microenvironment and 3D growth of meningiomas *in vivo*; (ii) the process of culturing cell lines selects for cells that may not be relevant in patient tumors; (iii) fundamental changes in cell physiology due to immortalization; and (iv) the potential for new genetic alterations not seen in original tumors. Thus, while many cell lines for meningioma exist, their shortcomings prevent us from fully and holistically understanding all aspects of meningioma biology with these models.

Recent advances in cell culture technology provide a new potential avenue for more accurate models of meningioma. Organoids are miniature version of organs grown *in vitro*, but in 3D culture, that can mimic human physiology. Indeed, many advances have been made in the development of brain organoids in the recent past[3,4]. Co-cultures of brain organoids with cells from glioblastomas, another common intracranial tumor, have been successfully used to model glioblastoma growth and response to therapy[5]. While no papers to date have published organoid co-culture models with meningioma cells, the successful use of this framework for other intracranial tumors lends credence to the idea that organoid models are a potential path forward in the future development of *in vitro* meningioma models that more faithfully recapitulate *in vivo* biology.

Mouse Models

      In vivo mouse models of cancer are more costly and less expedient than cell culture systems, but they typically overcome many of the limitations of *in vitro* models. Moreover, preclinical *in vivo* testing is a necessary component of drug development and translation into clinical trials. Thus, establishing mouse models that recapitulate human meningioma is essential for understanding meningioma biology and improving treatments for meningioma patients.

Genetically Engineered Mouse Models

      Genetically engineered mouse models (GEMMs) of cancer are mice that are genetically altered to overexpress or lack specific genes that either induce or inhibit tumor growth, respectively. For tumors with clear genetic causes that can be recapitulated in murine systems, GEMMs are incredibly powerful because they often closely mimic *de novo* tumor initiation, growth and progression in the context of immunocompetent mammalian physiology with a controlled genetic background. Thus, GEMMs are a popular choice for studying many types of cancer, but they have two major drawbacks. First, tumor latency can be long and variable. Depending on the necessary genetic changes, the timing of tumor growth in GEMMs can be inconsistent and the percentage of mice that develop tumors can be small. Thus, it can be difficult to perform large-scale, reproducible, robust experiments with GEMMs. Second, differences between human and mouse genetics and physiology can vary widely depending on the gene and tissue of interest. While most human genes are conserved and have orthologs in mice, many do not. Moreover, the regulation and function even of conserved genes can vary unpredictably across species.

Given the frequency of *NF2* inactivation in human meningioma, all approaches to generate GEMMs for meningioma involve inactivation of *Nf2*. *Nf2* is critical for development of the extraembryonic ectoderm in mice; thus, mice with homozygous germline deletion of *Nf2* die early in embryonic development[6]. Heterozygous germline deletion of *NF2* in humans defines neurofibromatosis type 2, a clinical syndrome associated with a spectrum of tumorous growths, including bilateral vestibular schwannomas, multiple meningiomas and ependymomas[7,8]. However, mice with heterozygous germline deletion of *Nf2* develop osteosarcomas instead of schwannomas or meningiomas[9], suggesting that mice use and regulate *Nf2* differently than humans.

Consistent with syndromic tumors arising from germline deletion of *NF2*, somatic loss of *NF2* in the human meninges is also associated with sporadic meningiomas. To localize the effects of *Nf2* loss to the meninges of mice, laboratory scientists have generated a GEMM, known as *Nf2^{fl/fl}*, with special genetic sequences (loxP) flanking the *Nf2* gene [10]. In normal cells, loxP sequences have no effect on the gene that they flank. However, in cells that express Cre, a protein that targets and recombines DNA flanked by loxP sites, all genetic material in between loxP sites is deleted, which in the case of *Nf2^{fl/fl}*, means the *Nf2* gene. In order to express Cre in the meninges of the mice and induce tumor formation, adenovirus Cre-recombinase is injected into the cerebrospinal fluid (CSF) of *Nf2^{fl/fl}* mice. After intrathecal injection, *Nf2^{fl/fl}* mice develop meningioma-like growths that mimic the histopathology of the most common subtype of meningioma in humans[10]. Unfortunately, only 30% of *Nf2^{fl/fl}* animals develop these tumors, and the vast majority are benign, which makes survival comparisons and studies difficult. Moreover, perhaps owing to the location of the intrathecal adenovirus Cre-recombinase injection,

many *Nf2^{fl/fl}* mice develop spinal meningiomas, resulting in spinal cord compression, which is incredibly rare in humans.

Introducing a heterozygous *p53* mutation in the *Nf2^{fl/fl}* mice increases meningioma burden and decreases survival. However, the lack of *TP53* alterations in human meningiomas calls into question the physiological relevance of meningioma models lacking *p53*. In contrast, the *CDKN2AB* locus is more frequently altered in human meningiomas (although less than *NF2*). Loss of *Cdkn2ab* in addition to *Nf2* in the meninges of mice via intrathecal adenovirus Cre-recombinase injection results in a majority of mice growing high-grade meningiomas[11]. While this GEMM represents a significant step forward in modeling meningioma, many of the mice develop non-meningioma tumors, such as osteomas, liver tumors and subcutaneous sarcomas, revealing non-specific effects of the genetic alterations and adenovirus Cre-recombinase injection.

Another method to specifically target the meninges cells of mice has been to identify markers of those cells. In particular, prostaglandin D2 synthase (*PDGS*) is a marker of arachnoid cells in the meninges[12], and *Nf2* inactivation in mouse cells expressing *Pdgs* results in meningeal overgrowth, suggesting PDGS expression may identify a potential cell of origin for mouse meningioma[13]. However, meningeal tumors are only seen in 38% of *Pdgs-Cre Nf2^{fl/fl}* mice, and the histology of tumors that do develop is more consistent with meningeal hyperplasia than oncogenesis. Beyond *NF2* alterations, the platelet-derived growth factor (PDGF) pathway is often upregulated in human meningiomas[14]. Thus, to increase the tumorigenicity of the *Pdgs-Cre Nf2^{fl/fl}* GEMM, *PDGF* is concurrently overexpressed in addition to *Nf2* inactivation in *Pdgs*-positive mouse

102

arachnoid cells. While these mice grow more meningiomas than *Nf2* inactivation alone, the mice also grow as many gliomas, suggesting non-meningioma-specific effects of the genetic alterations[15]. Thus, *Pdgs*-positive cells in mice can give rise to meningioma-like phenotypes when specific genes are altered, but the specificity of these phenotypes and their generalizability to human meningioma remain incompletely defined.

Patient-Derived Xenograft Models

Patient-derived xenograft (PDX) models provide an alternative way to study human disease in mice when mouse genetics differ significantly from human genetics or if a disease is not genetically defined. PDX models rely on engrafting of patient-derived tumor cells into immunocompromised mice, thus allowing human tumor cells to grow in a much more physiologic environment than *in vitro* cell culture. While the tumor microenvironment is incompletely recapitulated in PDX models due to the lack of immune cells, the use of actual human tumor cells makes this an attractive model for preclinical testing of novel therapeutic agents. Engraftments can be heterotopic (i.e. at a different site on the mouse than the human) or orthotopic (i.e. the same site). While orthotopic engraftments are generally thought to be more physiologically relevant, difficulty in accessing tumor growth at certain orthotopic sites, such as the skull base where many meningiomas grow, can affect reproducibility of engraftments and make it difficult to track tumor growth.

PDX models have been attempted for meningioma since 1945, when human meningiomas were injected into the eyes of guinea pigs, an immune-privileged site[16]. Heterotopic mouse PDX models of meningioma, where resected patient tumors are engrafted into the subcutaneous flank of immunocompromised mice, were first reported in the 1970s[17,18]. Recent characterizations of meningioma PDX models find that the

engrafted cells retain the chromosomal, genetic and histologic features of parental tumors[19]. However, patient tumors are not readily accessible for a vast majority of researchers and there can be substantial heterogeneity between patients. Thus, most recent efforts in generating PDX models for meningioma involve orthotopic injection of human meningioma cell lines into mice. Most commonly, Ben-Men-1 and IOMM-Lee cells (**Table 3.1**) are used in orthotopic systems, but the growth of tumors in mice is slow and varies substantially among and within research groups, likely due to the technical skill required for replicable orthotopic brain injections. Another drawback of the PDX model is that engrafted cells sometimes exhibit ventricular invasion and leptomeningeal invasion, which are incredibly rare findings in human meningioma patients[20].

Chemically Induced Mouse Models

ENU, a potent carcinogen and DNA alkylating agent, has been used to induce mutations and tumors in model organisms since its discovery in 1951[21]. Cancer models using ENU, which induces random mutations throughout the genome, have become less common as it becomes easier to make more targeted genetic alterations in mice. Nevertheless, ENU mutagenesis of mice heterozygous for *p16* and *p19* induces meningioma growth[22]. However, the genetic landscape of these tumors has never been characterized; thus, basic questions such as the *Nf2* status of the tumors remain unanswered. The median age of diagnosis for meningiomas is 66 years old and they are vanishingly rare in children[23], suggesting that randomly acquired mutations over time play a role in meningioma's pathogenesis and progression. Thus, future models could take advantage of this chemical mutagenesis system and combine it with a GEMM that is genetically susceptible to meningioma, such mice with heterozygous deletion of *Nf2* in

the meninges. Combining knowledge about the genetics (frequency of *Nf2* alterations) and natural history (accumulation of random mutations over time) of meningioma may be the next step in the development of new mouse models.

Preclinical Studies

In addition to shedding light on the fundamental biology of meningioma, an optimal use of meningioma mouse models is as a first line of validation for novel therapeutics. Unfortunately, none of the available mouse meningioma models discussed have been successfully used for preclinical trials. Despite the increasing prevalence of orthotopic PDX models, all preclinical studies thus far have been performed in PDX models where meningioma cell lines were heterotopically injected into the flank of the mouse. Preclinical studies conducted in meningioma PDX models include the use of antiprogesterone RU-38486[24], FAS inhibitor GSK2194069[25], celecoxib[26], and the combination of hydroxyurea and verapamil[27]. Despite initially promising results *in vivo*, a lack of reproducibility or poor rates of response precluded any of these drugs from clinical translation.

Substantial work has been done to establish easy-to-manipulate models that recapitulate the genetics, histology and progression of meningioma. Unfortunately, many of the models established thus far have considerable drawbacks and fail to encapsulate essential components of human meningioma. The lack of tractable model systems hinders our ability to study the biology and mechanisms underlying meningioma. Fortunately, advances in cell culture technology and imaging of xenografts will allow for improvement of our current models towards something physiologically more accurate. Organoid co-culture models combine the scalability of cell culture with the physiologically accurate microenvironment of *in vivo* animal models. Moreover, recent multi-modal

sequencing efforts have given new insight into the molecular mechanisms and drivers of meningioma[28,29]. Combining new knowledge with new techniques will be crucial for developing robust models of meningioma.

Meningiomas harbor Notch3⁺ perivascular cells

To understand how the different cell types underlying meningioma drive tumorigenesis, we analyzed 40,918 cells from 8 meningioma samples from the meningioma cell clusters identified by the single-cell RNA sequencing performed in **Chapter 2** (**Fig. 3.1a**). While the majority of cells demonstrated chromosome 22q loss, we identified a distinct cluster of perivascular cells where only half the cells had chromosome 22q loss (**Fig. S2.9a**). Chromosome 22q includes *NF2*, whose loss is the most common and penetrant chromosomal alteration in meningioma and a driver of meningiomagenesis[1,7,30]. Therefore, we hypothesized that this cell population might represent meningioma progenitors in an early stage of tumorigenesis. A comparison of perivascular cells from meningiomas with perivascular cells from normal meningeal samples confirmed that all normal meningeal cells were copy-neutral at chromosome 22q, compared with two-thirds of meningioma tumor cells (**Fig. 3.1b**). Setting this population of cells as the starting point for pseudotime trajectory analysis demonstrated a transcriptomic progression that encompassed all other meningioma cell clusters (**Fig. 3.1c**).

NOTCH3, a Notch pathway receptor and mural cell marker[31], and *CD90*, a cancer stem cell marker[32–34], were differentially expressed in the perivascular cell population compared to all other cell populations (**Fig. 3.1d**). Gene ontology analysis of differentially

expressed genes in this population also revealed enrichment of several stem cell and dedifferentiation pathways (**Fig. S3.1a**). Notably, *NOTCH3* expression, but not that of other Notch receptors, marked this population of cells (**Fig. S3.1b**). Therefore, we hypothesized that NOTCH3 expression specifically identifies a dedifferentiated progenitor population within meningiomas. To characterize NOTCH3-expressing cells in meningiomas, we performed immunohistochemistry and immunofluorescence, which localized NOTCH3 to the perivascular niche in WHO Grade 1 and 2 meningiomas. Similar but more diffuse staining was observed in WHO Grade 3 meningiomas (**Fig. 3.1e-g and S3.2**). Co-staining with endothelial markers, such as SMA and vWF, confirmed that NOTCH3 specifically marks perivascular, but not endothelial cells, in meningiomas (**Fig. S3.3-S3.8**). To transcriptomically confirm these differences across WHO grades, reference transcriptomic signatures of meningioma single-cell clusters were used to estimate proportions of meningioma cell types from bulk RNA-sequencing of 200 meningiomas. This analysis confirmed an enrichment of Notch3^{+} perivascular cells in WHO Grade 3 meningiomas (**Fig. 3.1h**). As expansion of dedifferentiated and stem cell-like populations in other cancers correlates with worse outcomes[35], these results may partially explain the worse clinical outcomes of WHO Grade 3 meningiomas.

Notch3^{+} perivascular cells are conserved across vertebrate meningeal tumors

To confirm the relevance of this perivascular population across vertebrate meningeal tumors, we performed single-cell RNA sequencing of 54,607 cells from 3 canine meningiomas and 2 canine meningeal samples (**Fig. 3.2a and S3.9**). Cell cluster identities from our human meningioma data (**Fig. 2.3c**) were projected onto the canine

samples based on the transcriptional correlation and expression of marker genes conserved across species (**Fig. 3.2b**). In addition to a perivascular population that clustered separately from the meningioma cells, many cells transcriptionally similar to perivascular cells were present within canine meningioma cell clusters (**Fig. 3.2c**). These data suggest that normal canine perivascular cells share transcriptional features with a subset of canine meningioma cells, consistent with our findings in human meningiomas.

Hemangiopericytomas, another human meningeal tumor type, are rare and often indistinguishable from meningiomas by radiographic imaging (**Fig. 3.2d**). Unlike meningiomas, which are most commonly characterized by loss of *NF2*[1], hemangiopericytomas are characterized by the NAB2-STAT6 fusion[36]. To analyze the cell types underlying hemangiopericytomas, we performed single-cell RNA sequencing of 7,046 cells from 1 human hemangiopericytoma sample. Cell cluster identities from our human meningioma data were projected onto the hemangiopericytoma sample based on transcriptional correlation and expression of marker genes (**Fig. 3.2e**). As in human meningiomas, we found a small population of perivascular cells expressing *NOTCH3* which clustered in proximity to hemangiopericytoma tumor cells in reduced dimensionality space (**Fig. 3.2f**). Immunofluorescence further confirmed NOTCH3 expression in the perivascular niche within hemangiopericytomas (**Fig. 3.2g**). These data demonstrate that multiple meningeal tumors across vertebrate species demonstrate the presence of a perivascular niche that may harbor dedifferentiated tumor progenitor cells.

Notch3⁺ perivascular cells are conserved across vertebrate meningeal development and homeostasis

As we hypothesized that Notch3⁺ perivascular cells might represent a dedifferentiated progenitor population within meningeal tumors, we sought to understand the role of this population in vertebrate development and homeostasis. Immunofluorescence of human embryos at gestational week 17 localized NOTCH3 expression to perivascular cells during normal human development (**Fig. 3.3a**). Both immunohistochemistry and immunofluorescence also showed that NOTCH3 marked perivascular cells in adult human meninges (**Fig. 3.3b, c**). To identify this population of cells in other vertebrates, we generated a Notch3-Cre^ERT2 ROSA^mT/mG mouse. In these transgenic mice, Cre becomes active upon tamoxifen administration and induces recombination of the mT/mG locus to express eGFP instead of tdTomato (**Fig. 3.3d**). Both *in utero* and postnatal recombination of the mT/mG locus revealed that Notch3 localization specific to perivascular cells (**Fig. 3.3e, f**). In contrast, Pdgs-cre, which has been used to generate prior meningioma mouse models[13], non-specifically marked cells within the mouse meninges and was not specifically expressed in any human meningioma single-cell clusters (**Fig. S3.10a, b**). Taken together, these data suggest that Notch3 expressing cells may be specific cells of origin for meningiomas across several vertebrates.

Discussion

Current meningioma mouse models are non-specific and often inadequate to study meningioma biology or develop new therapies. By identifying a potential meningioma

progenitor population that is conserved across vertebrate species, we hope to spur the development of new, more representative models of meningioma. We hypothesize that loss of *NF2* in Notch3$^+$ cells represents the first step in meningiomagenesis. While other genetic or epigenetic perturbations may also be necessary for tumorigenesis and this hypothesis does not account for all meningiomas, some of which retain an intact *NF2* locus, this framework fundamentally shifts how meningeal tumors are understood. The conservation of a perivascular population across multiple meningeal tumors suggests that different genetic perturbations to this same population, such as *NF2* loss versus NAB2-STAT6 fusion, may result in the formation of different types of meningeal tumors, such meningioma and hemangiopericytoma. With this framework, new mouse models of meningeal tumors can be developed, a crucial step in studying these tumors in a more physiologic system, understanding their underlying biology, and developing new treatments.

Methods

Single cell RNA sequencing

Fresh human and canine meningioma and dura samples and the fresh hemangiopericytoma sample were acquired from the operating room and transported to the laboratory in PBS at 4°C. Tissue samples were processed as previously described in the Methods section of **Chapter 2**. Single cell suspensions were processed for single cell RNA sequencing using a 10X Chromium controller, and libraries were generated using the Chromium Single Cell 3' Library & Gel Bead Kit v3 on a 10X Chromium controller using the manufacturer recommended default protocol and settings (#1000121, 10X Genomics). Libraries were sequenced on an Illumina NovaSeq 6000, targeting >50,000 reads/cell, at the UCSF Center for Advanced Technology.

Single cell RNA sequencing analysis was performed using CellRanger version 3.02, R version 3.6.1, and Seurat[37,38] version 3.0.1, as previously described in the Methods section of **Chapter 2**. Canine meningioma samples were aligned to the canFam3.1 canine reference genome[39]. Uniform Manifold Approximation and Projection (UMAP) was performed on the data with a minimum distance metric of 0.3 and Louvain clustering was performed using a resolution of 0.1. The human hemangiopericytoma sample was aligned to the GRCh38 human reference genome. UMAP was performed on the data with a minimum distance metric of 0.2 and Louvain clustering was performed using a resolution of 0.5.

Cell cluster identities from the human meningioma single-cell dataset were projected onto the canine meningioma and human hemangiopericytoma datasets using the 'FindTransferAnchors' and 'TransferData' functions in Seurat. The first 30 reduced

dimensions were used and the 'normalization.method' was set to 'SCT.' Bulk RNA-seq expression of meningiomas was deconvolved using reference transcriptomic signatures of single-cell clusters with CIBERSORTx[40] as previously described in the Methods section of **Chapter 2**.

Immunofluorescence

Human gestational week 17 brains were cut into ~1.5 cm coronal or sagittal blocks, fixed in 4% paraformaldehyde for 2 days, and then cryoprotected in a 30% sucrose solution. Blocks were cut into 30-micron sections on a cryostat, mounted on glass slides for immunohistochemistry, and stored at -80°C. Frozen slides were gradually equilibrated to room temperature, moved from -80°C to 4°C the night prior to staining and then to the lab bench for 2 hours before beginning the immunostaining protocol. Slides were washed once with PBS for 5 minutes, then once with TBS for 5 minutes before blocking with TBS+ (goat serum, BSA, albumin, glycine, and Triton-X 100 in TBS) for 1 hour. Primary antibody stainings were performed overnight at room temperature in TBS+. Primary antibodies used were NOTCH3 (1:200, #MABC594, Millipore Sigma), CD34 (1:200, #AF7227, R&D), and PDGFRβ (1:200, #AF385, R&D). The following day, three TBS washes were performed before incubating with secondary antibodies in TBS+ for 2 hours. After three additional TBS washes, DAPI was added and the slides were mounted.

Microscopy

Fluorescence microscopy was performed on a LSM 800 confocal laser scanning microscope with a PlanApo 20X air objective (Zeiss). Images were processed and

quantified from representative regions of each tumor or coverslip using ImageJ. Histologic and immunohistochemical features were evaluated using light microscopy on an BX43 microscope with standard objectives (Olympus). Images were obtained and analyzed using the Olympus cellSens Standard Imaging Software package.

Mice

This study was approved by the UCSF Institutional Animal Care and Use Committee (AN174769-03A), and all experiments complied with relevant ethical regulations. The Notch3$^{tm1.1(cre/ERT2)Sat}$ (Notch3-Cre^{ERT2}) mice were obtained from the Sweet-Cordero Lab at UCSF. The Gt(ROSA)26Sor$^{tm4(ACTB-tdTomato,-EGFP)Luo}$ (ROSA$^{mT/mG}$) mice were obtained from The Jackson Laboratory. These mice were intercrossed to generate Notch3-Cre^{ERT2} ROSA$^{mT/mG}$ mice. Recombination of the mT/mG locus in these mice was induced via intraperitoneal injection of 75 mg/kg of tamoxifen (#T5648, Sigma-Aldrich), dissolved in corn oil. For *in utero* recombination, pregnant ROSA$^{mT/mG}$ dams were injected with tamoxifen once at E16.5. For postnatal recombination, Notch3-Cre^{ERT2} ROSA$^{mT/mG}$ mice were injected daily 5 times with tamoxifen and euthanized 7 days after the fifth injection.

Mouse skullcaps were removed as previously described[41] after perfusion with PBS. Skullcaps were fixed in 4% paraformaldehyde (#15710, Electron Microscopy Sciences) overnight at 4°C, washed with PBS, and stored in PBS with 0.02% sodium azide. Meninges were dissected from the skullcaps as previously described[41] and mounted in ProLong Diamond Antifade Mountant with DAPI (#P36966, Thermo Fischer Scientific).
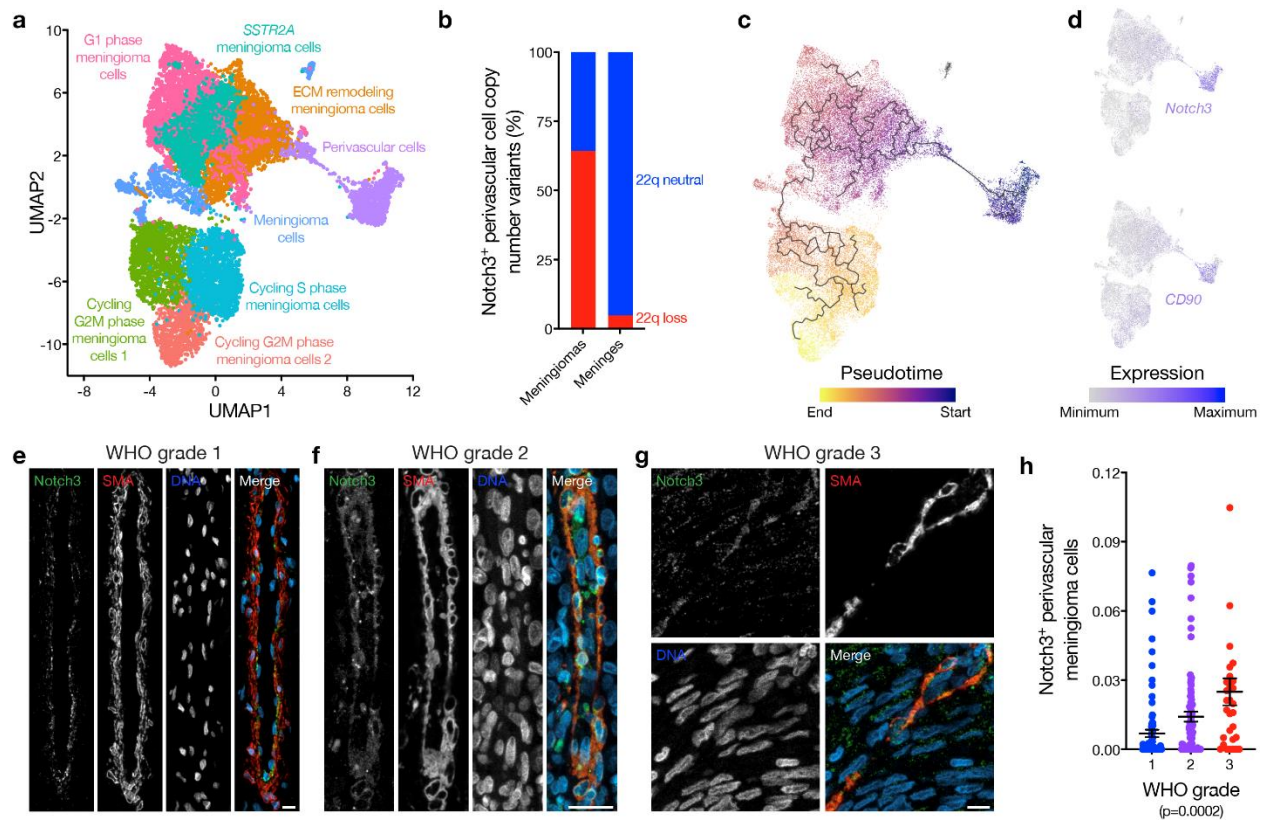
Figure 3.1 Meningiomas harbor Notch3+ perivascular cells

a, UMAP of single-cell RNA sequencing transcriptomes of 40,918 cells from meningioma cell clusters of 8 human meningioma samples and 2 human dura samples, colored by assignments from Louvain clustering. **b**, Percentage of cells with loss of chromosome 22q (whole arm) in Notch3+ perivascular cells, split by tissue type of origin. Cells from meningioma samples with loss of chromosome 22q and from dura samples with intact chromosome 22q were used for this analysis. **c**, Pseudotime analysis of single-cell transcriptomes from **a**, with the perivascular cell cluster set as the starting point. **d**, Gene expression of *NOTCH3* and *CD90* in meningioma single cells in reduced dimensionality space. **e**, Representative images of WHO grade 1 meningioma NOTCH3 and SMA confocal immunofluorescence microscopy. DNA is marked with Hoechst 33342. Scale bar 10 μM. **f**, Representative images of WHO grade 2 meningioma NOTCH3 and SMA confocal immunofluorescence microscopy. DNA is marked with Hoechst 33342. Scale bar 10 μM. **g**, Representative images of WHO grade 3 meningioma NOTCH3 and SMA confocal immunofluorescence microscopy. DNA is marked with Hoechst 33342. Scale bar 10 μM. **h**, Fraction of meningioma samples (n=200) classified as Notch3+ perivascular meningioma cells across WHO grade, based on single-cell reference transcriptomes from **a**.
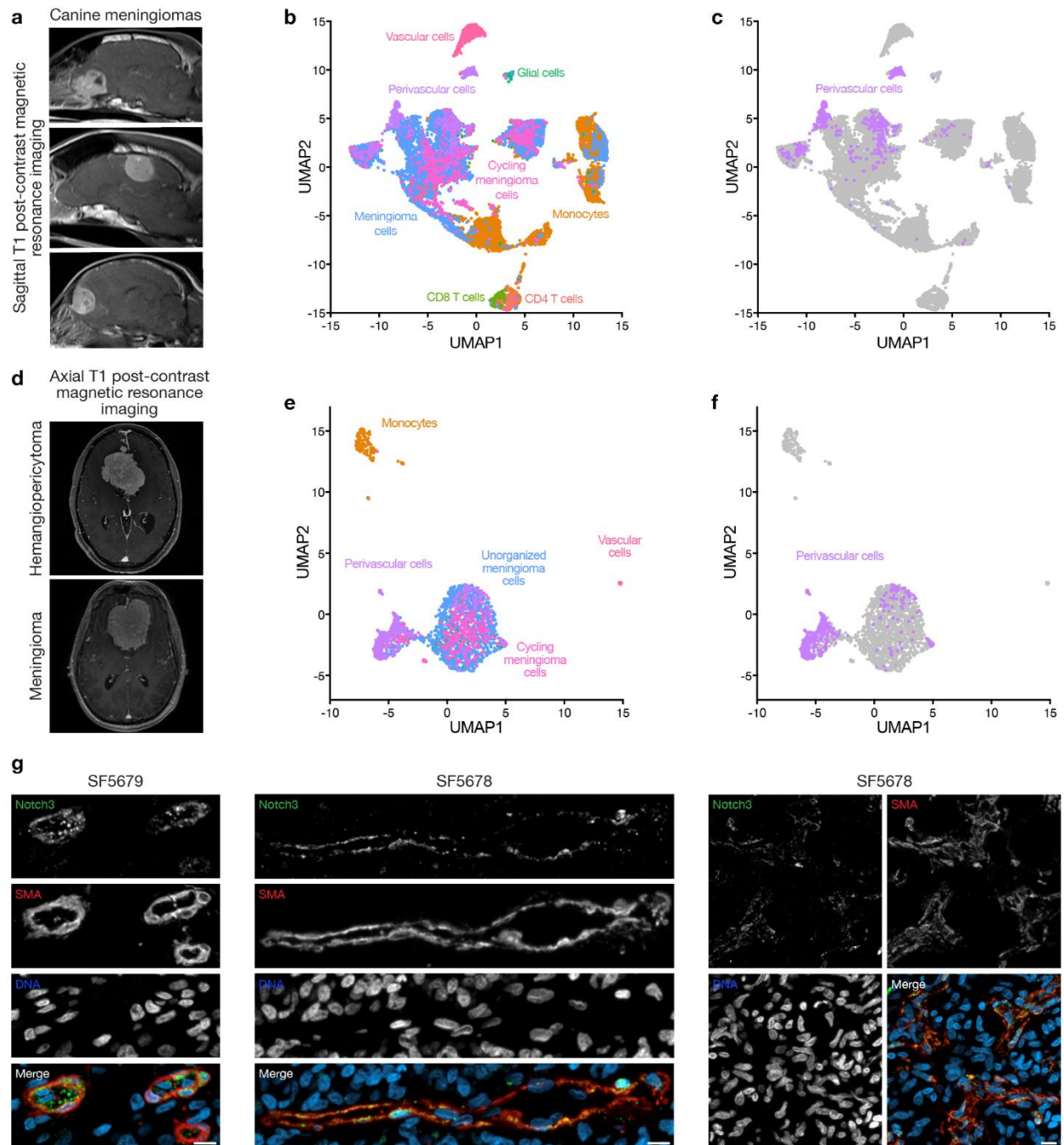
114

Figure 3.2 Notch3⁺ perivascular cells are conserved across vertebrate meningeal development and homeostasis

a, Magnetic resonance imaging of canine meningiomas processed for single-cell sequencing. **b**, UMAP of single-cell RNA sequencing transcriptomes of 54,607 cells from 3 canine meningioma samples and 2 canine dura samples, colored by cell identities projected from our human meningioma single-cell dataset. **c**, UMAP from **b** with only cells projected to have the perivascular identity colored. **d**, Magnetic resonance imaging of a hemangiopericytoma processed for single-cell sequencing (above) and a meningioma (below). **e**, UMAP of single-cell RNA sequencing transcriptomes of 7,046 cells from 1 human hemangiopericytoma sample, colored by cell identities projected from our human meningioma single-cell dataset. **f**, UMAP from **e** with only cells projected to have the perivascular identity colored. **g**, Representative images of

115

hemangiopericytoma NOTCH3 and SMA confocal immunofluorescence microscopy. DNA is marked with Hoechst 33342. Scale bar 10 µM.
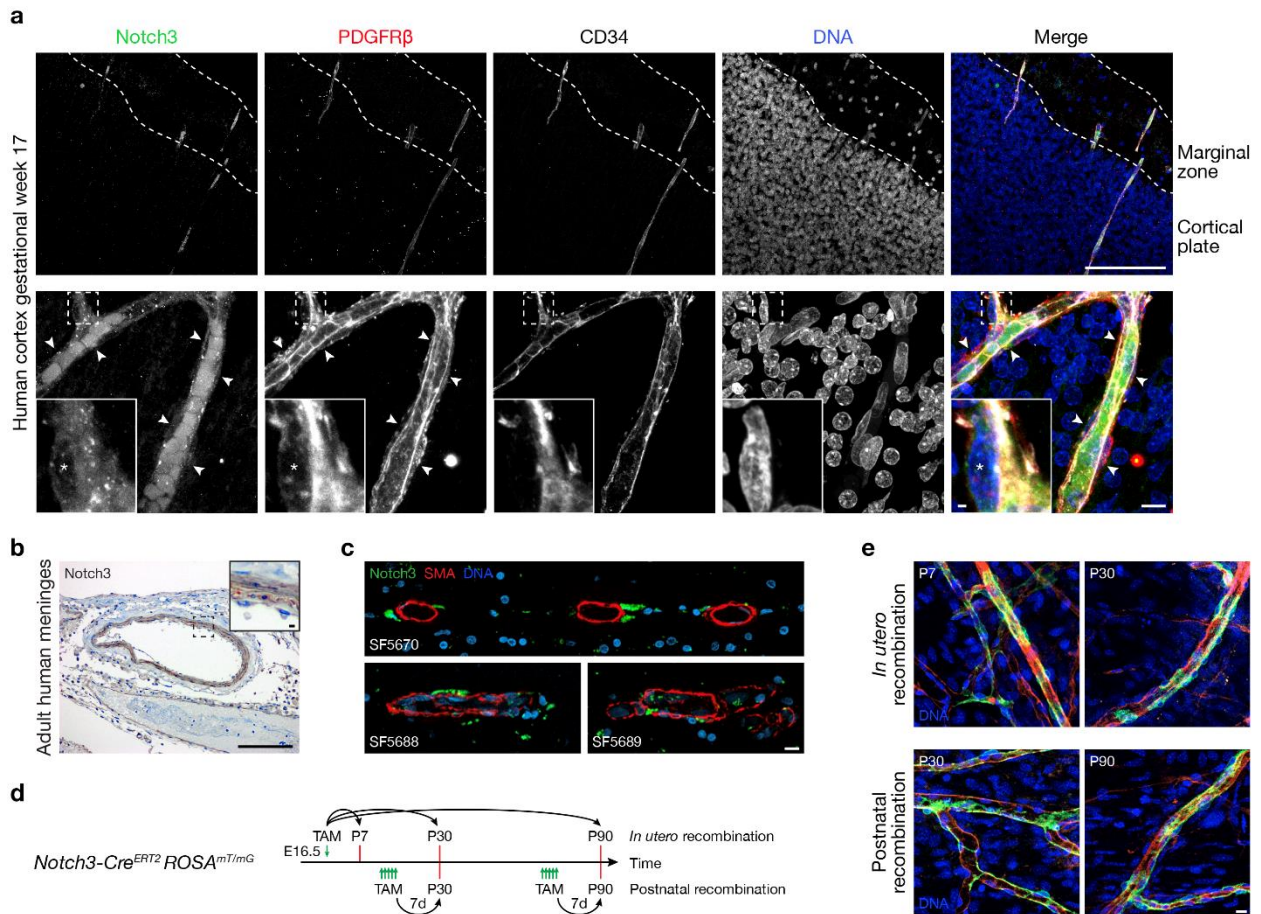
Figure 3.3 Notch3⁺ perivascular cells are conserved across vertebrate meningeal tumors

a, Representative images of human gestational week 17 brain tissue NOTCH3, PDGFRβ, and CD34 confocal immunofluorescence microscopy. DNA is marked with Hoechst 33342. Scale bar 10 µM. **b**, Representative images of NOTCH3 immunohistochemistry in adult human meninges. Scale bar 100 µM. **c**, Representative images of adult human meninges NOTCH3 and SMA confocal immunofluorescence microscopy. DNA is marked with Hoechst 33342. Scale bar 10 µM. **d**, Schema of *in utero* and postnatal recombination strategies in the Notch3-Cre^ERT2 ROSA^mT/mG mouse. Tamoxifen (TAM) injection timepoints are marked with green arrows. Euthanasia timepoints are marked in red. **e**, Representative images of Notch3-Cre^ERT2 ROSA^mT/mG mouse meninges confocal immunofluorescence microscopy after *in utero* (above) and postnatal (below) recombination. DNA is marked with DAPI. Scale bar 10 µM.
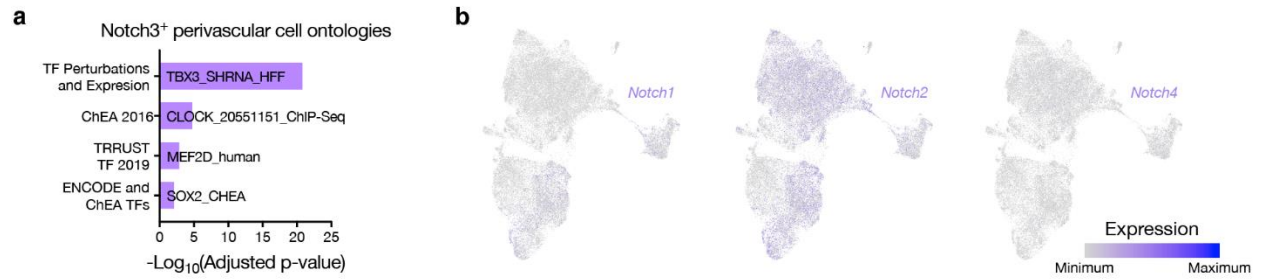
Figure S3.1 Meningioma Notch3+ perivascular cell ontologies and Notch receptor expression

a, Gene ontology analysis of differentially expressed genes in the perivascular cell single-cell cluster compared to other single-cell clusters. TF, transcription factor; ChEA, ChIP-X Enrichment Analysis. **b**, Gene expression of *Notch1*, *Notch2*, and *Notch4* in meningioma single cells in reduced dimensionality space.
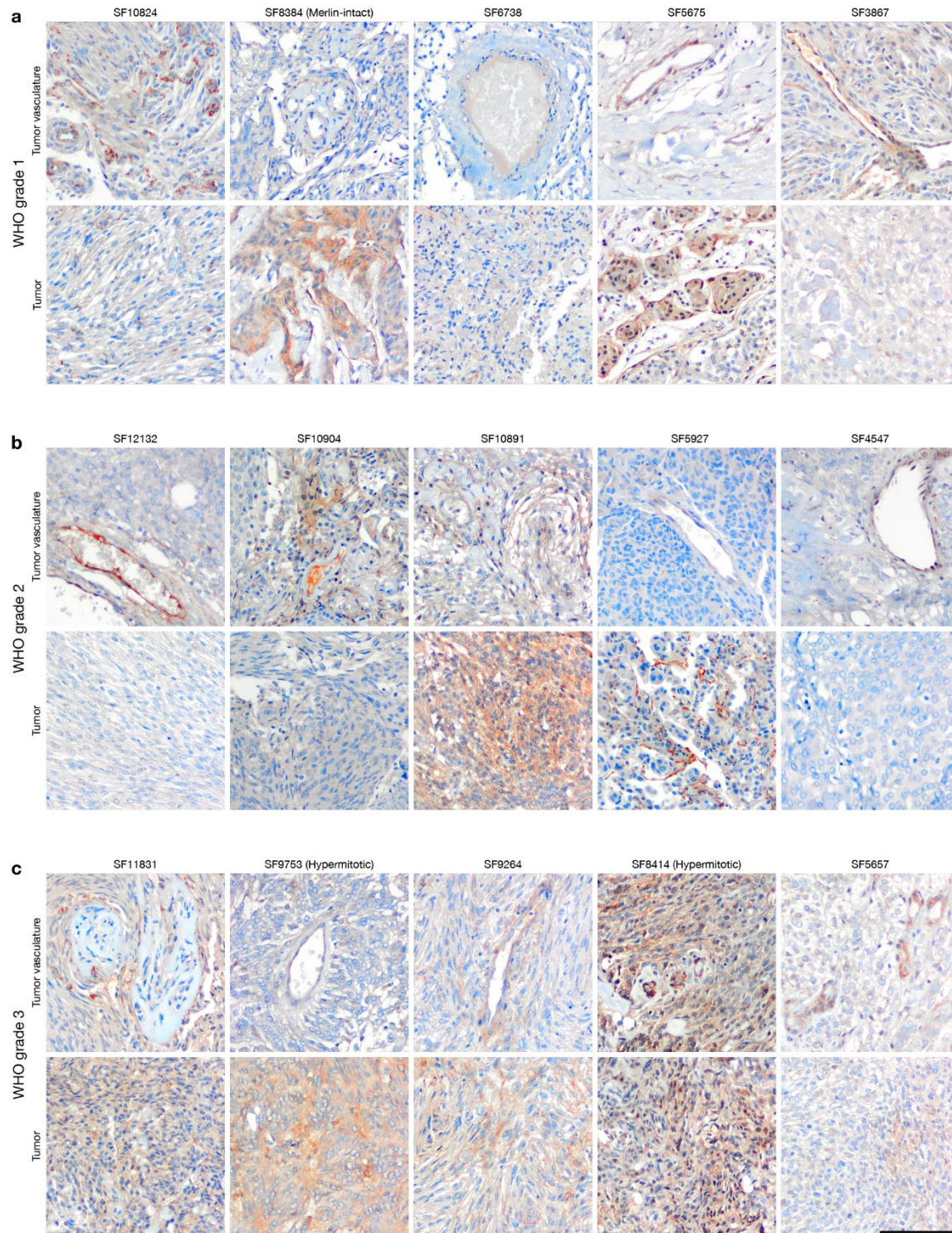
Figure S3.2 Meningioma Notch3 expression

Representative images of meningioma NOTCH3 immunohistochemistry in WHO Grade 1 (**a**), 2 (**b**), and 3 (**c**) meningiomas. Scale bar 10 μM.
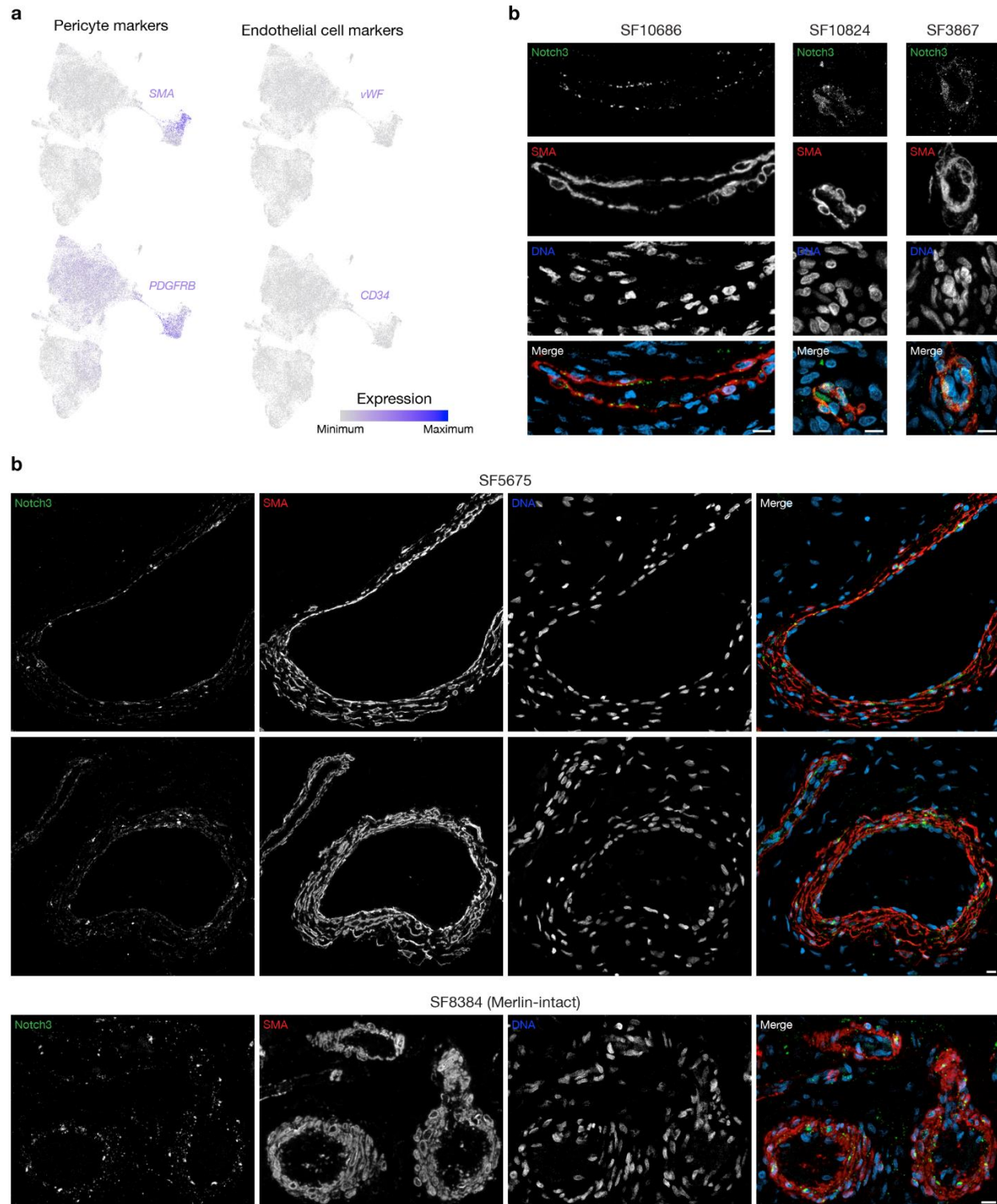
Figure S3.3 Notch3 and pericyte expression in WHO grade 1 meningiomas

a, Gene expression of *SMA*, *PDGFRB*, *vWF*, and *CD34* in meningioma single cells in reduced dimensionality space. **b**, Representative images of WHO grade 1 meningioma NOTCH3 and SMA confocal immunofluorescence microscopy. DNA is marked with Hoechst 33342. Scale bars 10 μM.

120

a

SF12132

Notch3

SMA

DNA

Merge

SF10891

Notch3

SMA

DNA

Merge

SF11041

Notch3

SMA

DNA

Merge

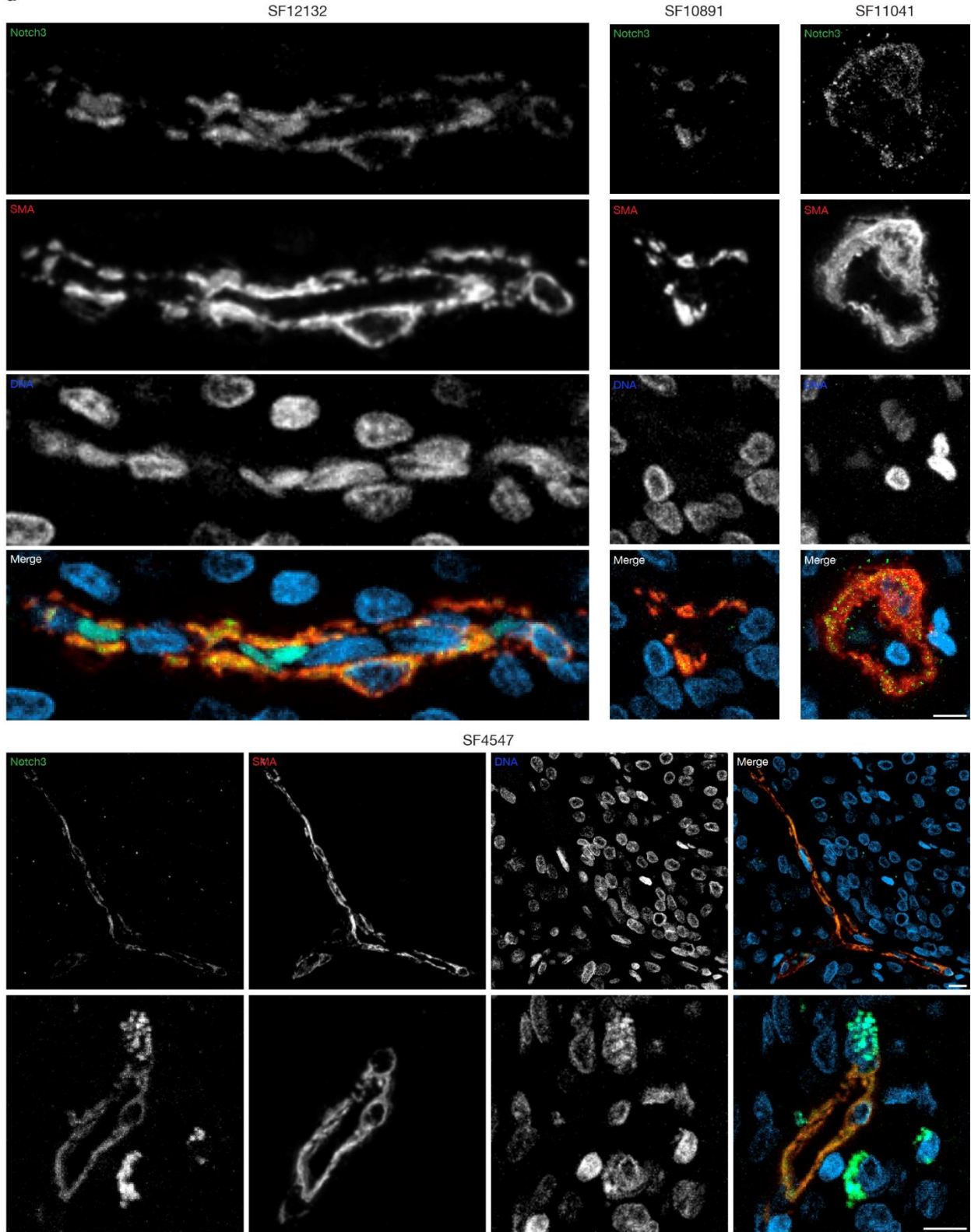SF4547

Notch3   SMA   DNA   Merge

Figure S3.4 Notch3 and pericyte expression in WHO grade 2 meningiomas

Representative images of WHO grade 2 meningioma NOTCH3 and SMA confocal immunofluorescence microscopy. DNA is marked with Hoechst 33342. Scale bars 10 μM.
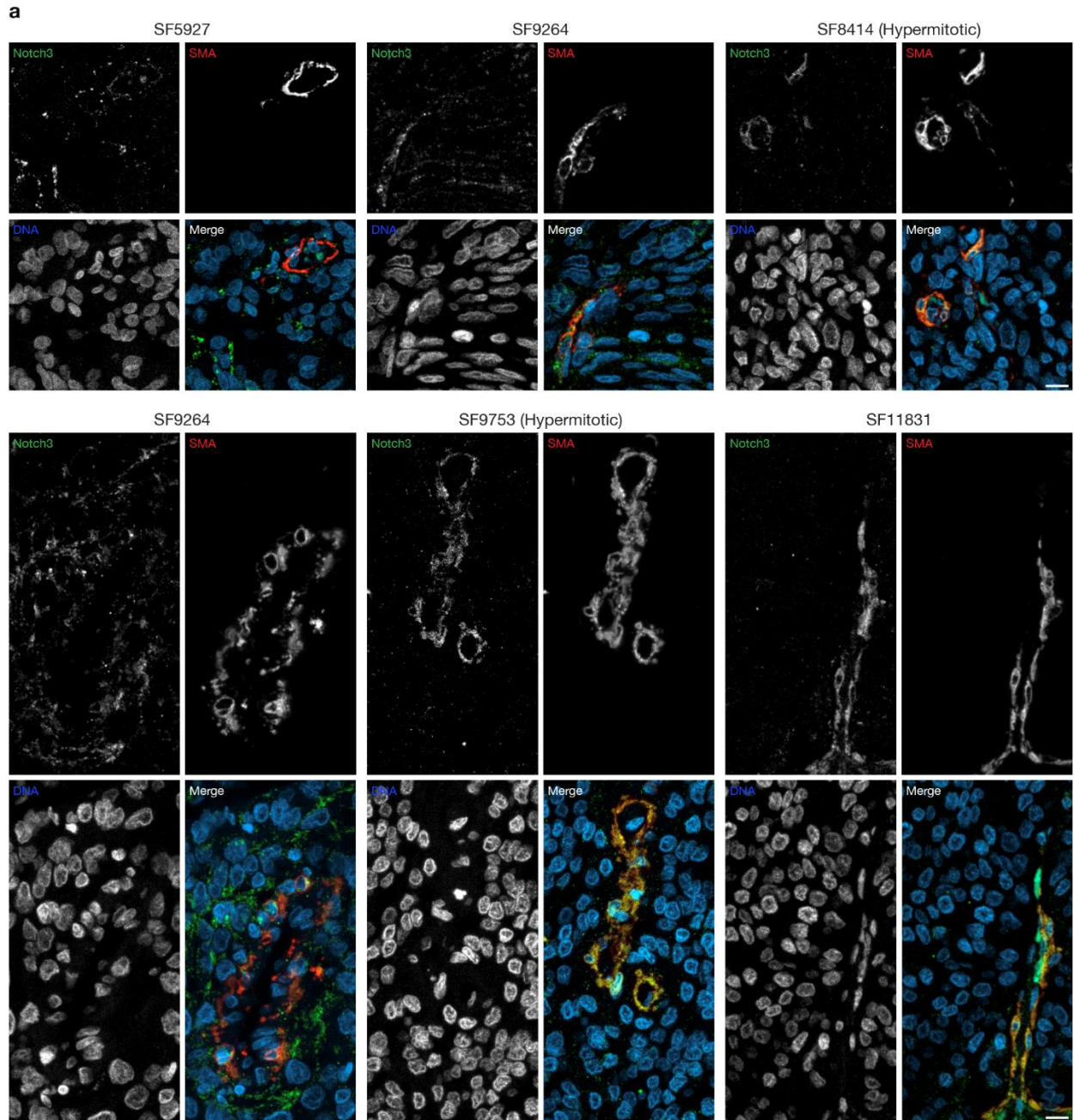
Figure S3.5 Notch3 and pericyte expression in WHO grade 3 meningiomas

Representative images of WHO grade 3 meningioma NOTCH3 and SMA confocal immunofluorescence microscopy. DNA is marked with Hoechst 33342. Scale bars 10 μM.
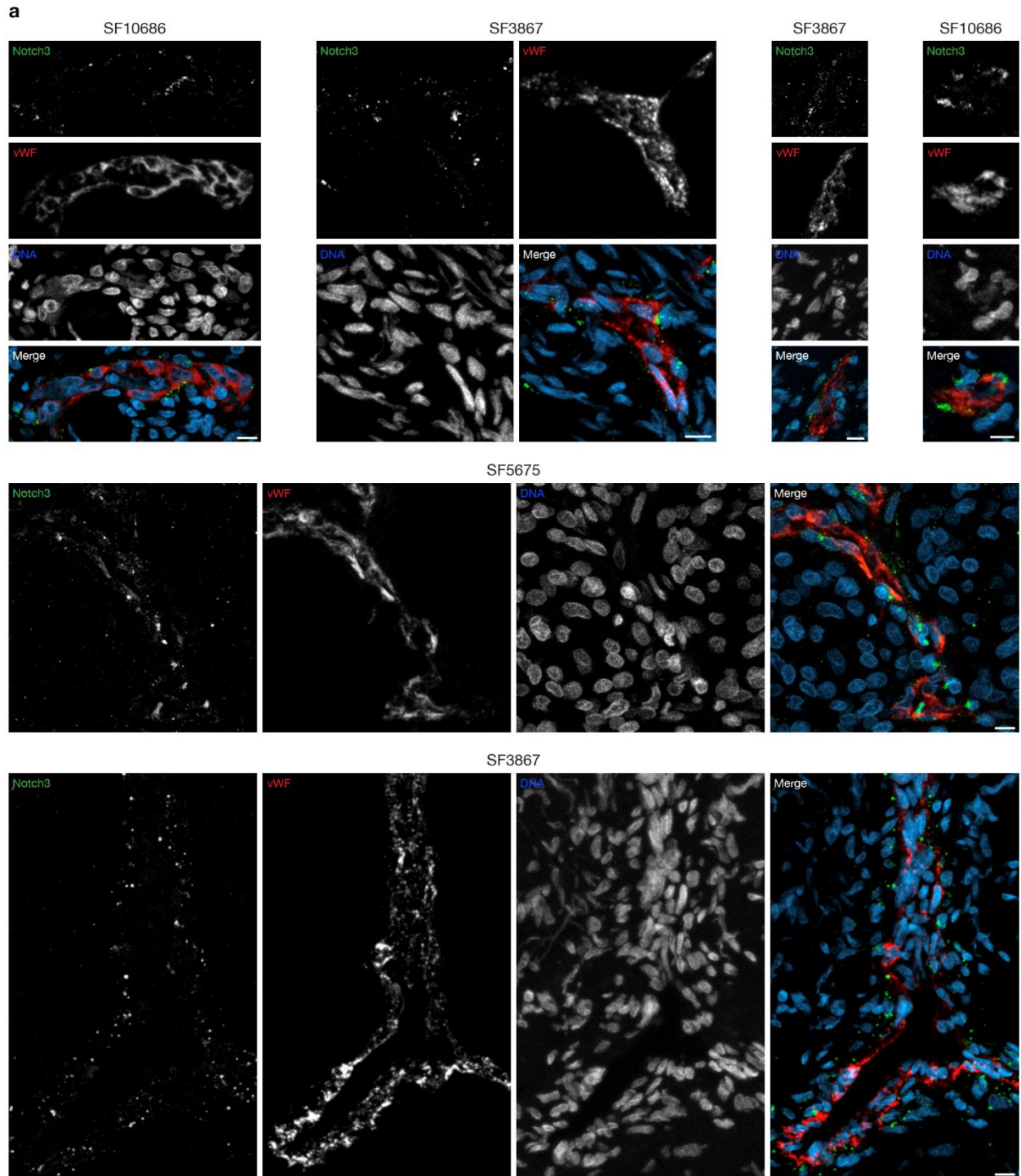
a

Figure S3.6 Notch3 and endothelial cell expression in WHO grade 1 meningiomas

Representative images of WHO grade 1 meningioma NOTCH3 and vWF confocal immunofluorescence microscopy. DNA is marked with Hoechst 33342. Scale bars 10 μM.
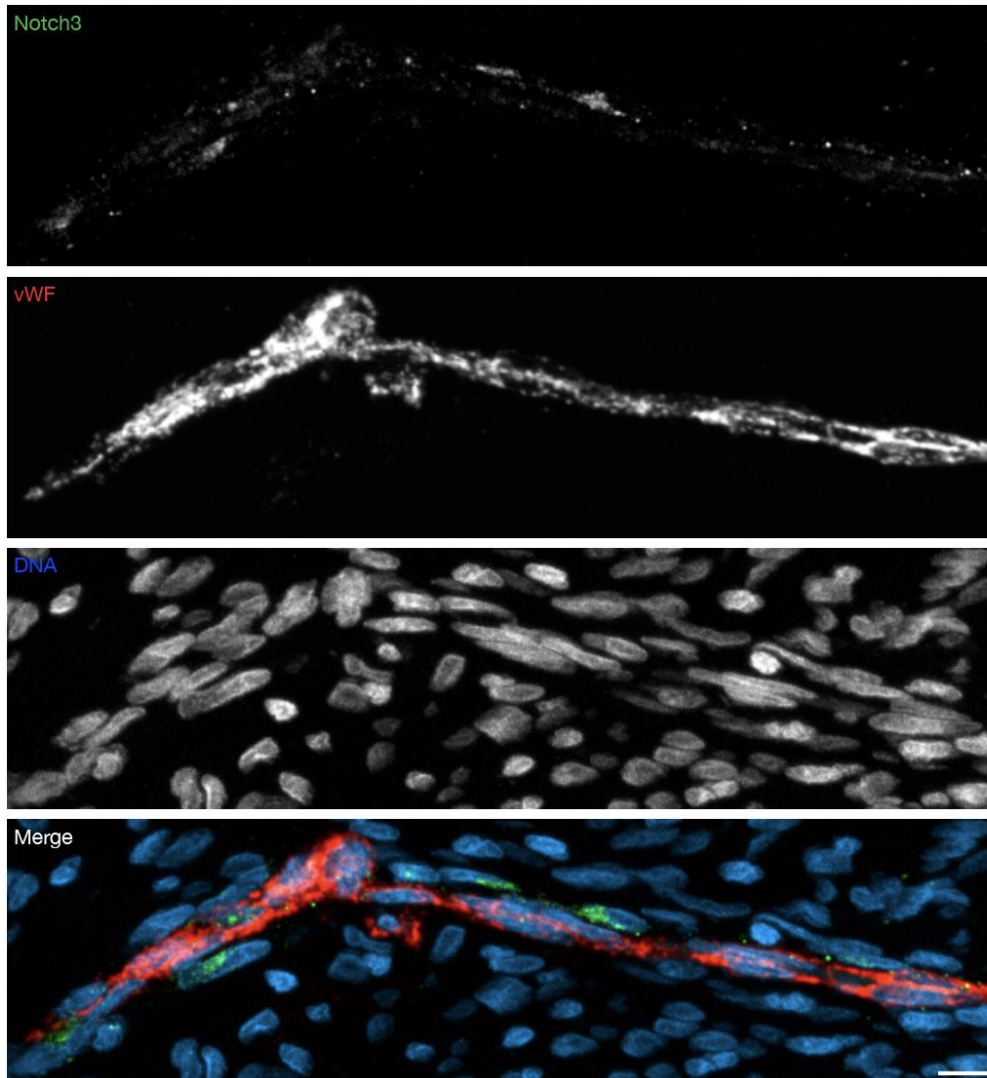
124

a

SF11041

Figure S3.7 Notch3 and endothelial cell expression in WHO grade 2 meningiomas

Representative images of WHO grade 2 meningioma NOTCH3 and vWF confocal immunofluorescence microscopy. DNA is marked with Hoechst 33342. Scale bars 10 μM.
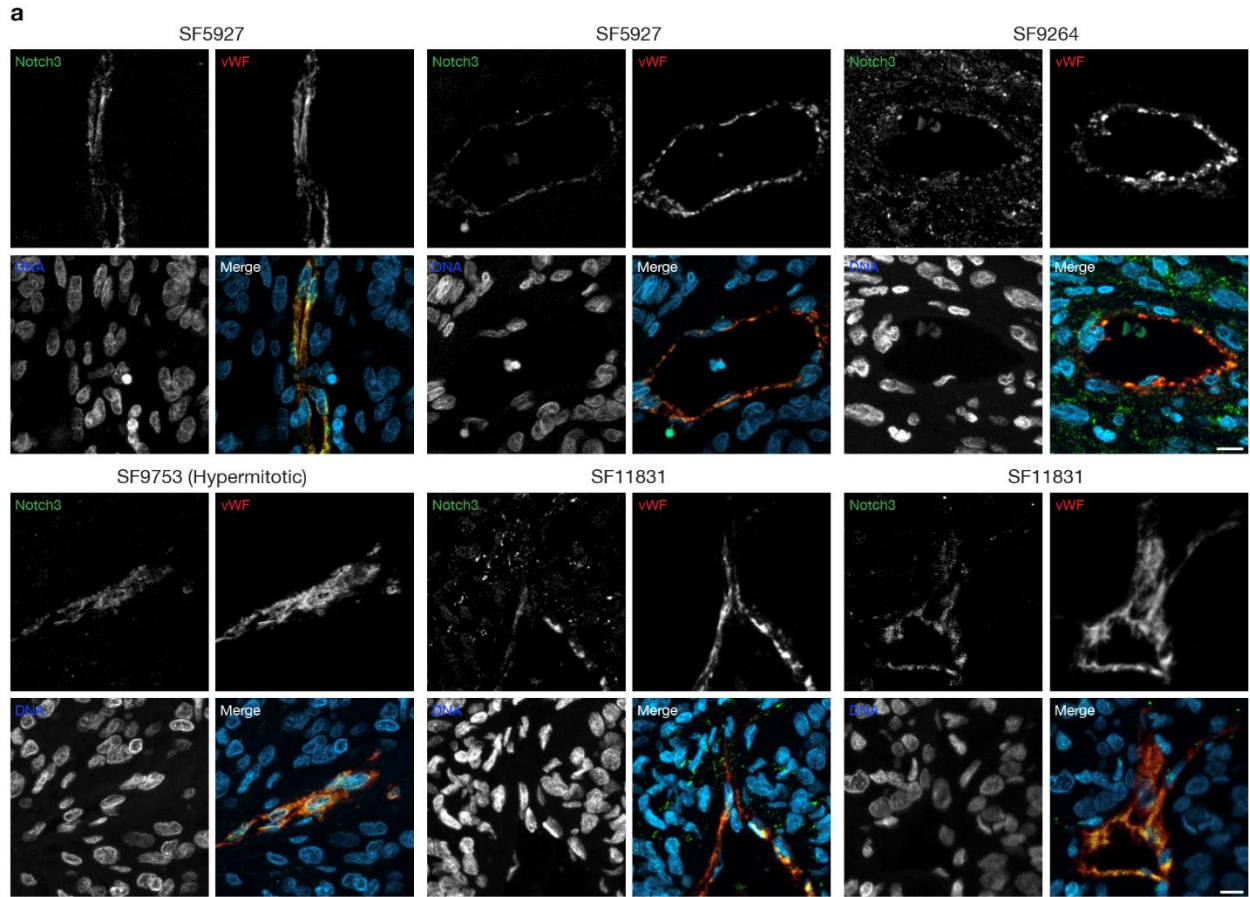
Figure S3.8 Notch3 and endothelial cell expression in WHO grade 3 meningiomas

Representative images of WHO grade 3 meningioma NOTCH3 and vWF confocal immunofluorescence microscopy. DNA is marked with Hoechst 33342. Scale bars 10 μM.
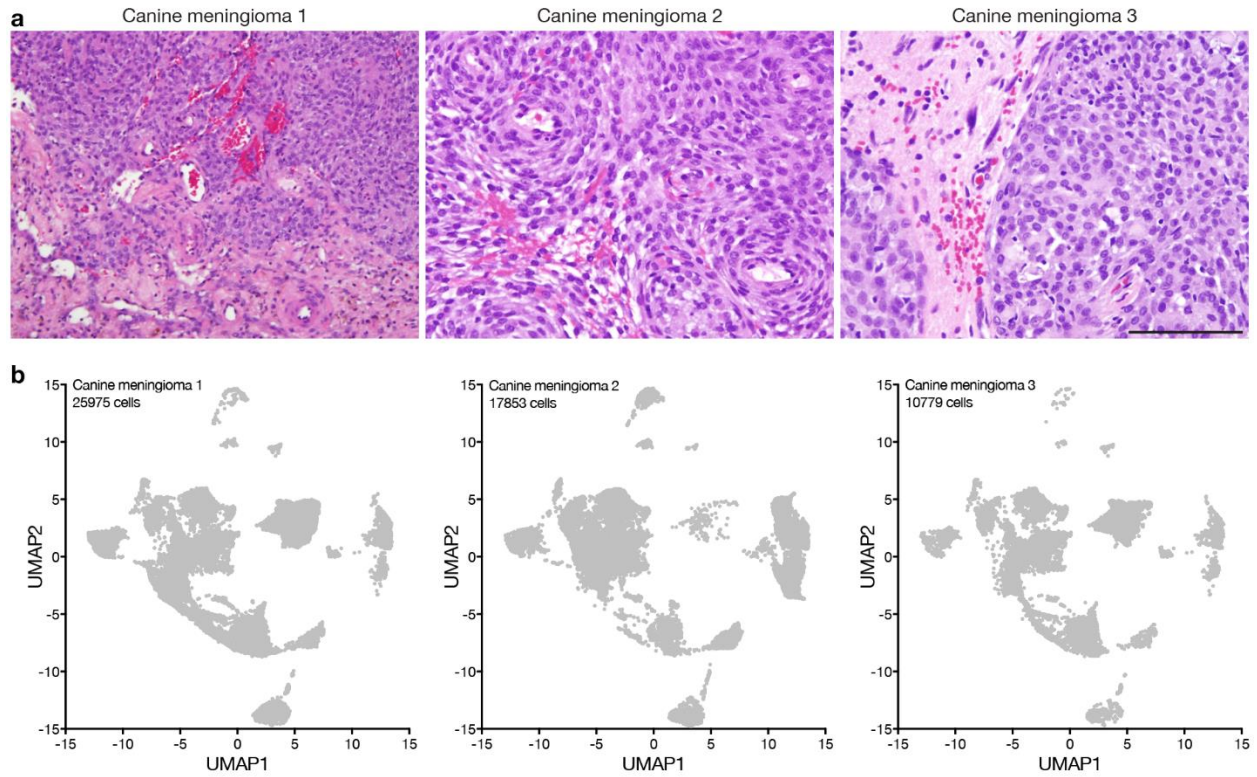
Figure S3.9 Canine meningioma single-cell RNA sequencing

a, Hematoxylin and eosin histologic staining of 3 canine meningiomas analyzed with single-cell sequencing.
b, Uniform manifold approximation and projection of single-cell RNA sequencing transcriptomes from 3 canine meningioma samples and 2 canine dura samples, split by patient of origin.

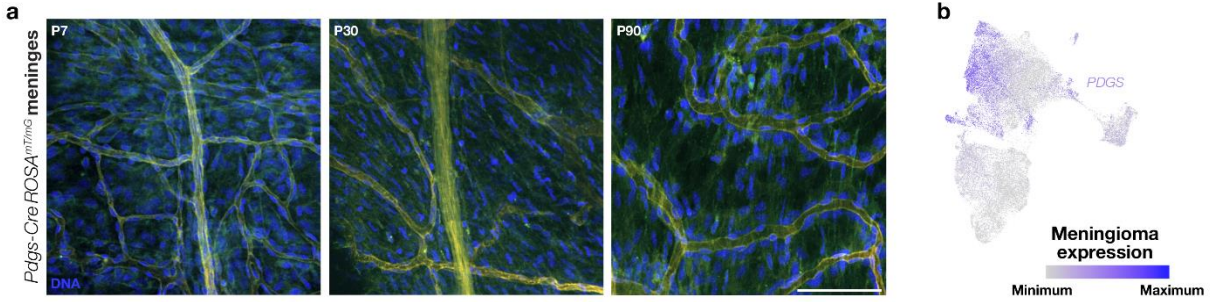*Figure S3.10* Meningeal Pdgs expression is non-specific and meningioma cells expressing *PDGS* do not represent a starting point in tumor evolution

a, Representative images of confocal immunofluorescence microscopy of Pdgs-cre ROSA$^{mT/mG}$ mice at P7, P30, and P90. **b**, Gene expression of *PDGS* in human meningioma single cells in reduced dimensionality space.

Table 3.1 Common meningioma cell lines and their characteristics.

Cell line	WHO Grade	Location	Gender	Age	NF2 status	Reference
Ben-Men-1	I	Optical canal	Female	47	Lost	(Püttmann et al., 2005)
HBL-52	I	Parietal falx	Female	68	Intact	(Akat et al., 2008)
IOMM-Lee	III	Intraosseous	Male	61	Intact	(Lee, 1990)
CH157-MN	Unknown	Unknown	Female	41	Lost	(Tsai et al., 1995)
KT21-MG1	Unknown	Unknown	Female	47	Lost	(Tanaka et al., 1989)

References

1. Yuzawa, S., Nishihara, H. & Tanaka, S. Genetic landscape of meningioma. *Brain Tumor Pathol.* **33**, 237–247 (2016).

2. Püttmann, S. *et al.* Establishment of a benign meningioma cell line by hTERT-mediated immortalization. *Lab. Invest.* **85**, 1163 (2005).

3. Krencik, R. *et al.* Systematic Three-Dimensional Coculture Rapidly Recapitulates Interactions between Human Neurons and Astrocytes. *Stem Cell Rep.* **9**, 1745–1753 (2017).

4. Pollen, A. A. *et al.* Establishing Cerebral Organoids as Models of Human-Specific Brain Evolution. *Cell* **176**, 743-756.e17 (2019).

5. Linkous, A. *et al.* Modeling Patient-Derived Glioblastoma with Cerebral Organoids. *Cell Rep.* **26**, 3203-3211.e5 (2019).

6. McClatchey, A. I., Saotome, I., Ramesh, V., Gusella, J. F. & Jacks, T. The Nf2 tumor suppressor gene product is essential for extraembryonic development immediately prior to gastrulation. *Genes Dev.* **11**, 1253–1265 (1997).

7. Petrilli, A. M. & Fernández-Valle, C. Role of Merlin/NF2 inactivation in tumor biology. *Oncogene* **35**, 537–548 (2016).

8. Rouleau, G. A. *et al.* Alteration in a new gene encoding a putative membrane-organizing protein causes neuro-fibromatosis type 2. *Nature* **363**, 515 (1993).

9. McClatchey, A. I. *et al.* Mice heterozygous for a mutation at the Nf2 tumor suppressor locus develop a range of highly metastatic tumors. *Genes Dev.* **12**, 1121–1133 (1998).

10. Kalamarides, M. *et al.* Nf2 gene inactivation in arachnoidal cells is rate-limiting for meningioma development in the mouse. *Genes Dev.* **16**, 1060–1065 (2002).

11. Peyre, M. *et al.* Meningioma progression in mice triggered by *Nf2* and *Cdkn2ab* inactivation. *Oncogene* **32**, 4264–4272 (2013).

12. Kawashima, M., Suzuki, S. O., Yamashima, T., Fukui, M. & Iwaki, T. Prostaglandin D Synthase (β-Trace) in Meningeal Hemangiopericytoma. *Mod. Pathol.* **14**, 197 (2001).

13. Kalamarides, M. *et al.* Identification of a progenitor cell of origin capable of generating diverse meningioma histological subtypes. *Oncogene* **30**, 2333–2344 (2011).

14. Figarella–Branger, D. *et al.* Platelet–derived growth factor (PDGF) and receptor (PDGFR) expression in human meningiomas: correlations with clinicopathological features and cytogenetic analysis. *Neuropathol. Appl. Neurobiol.* **20**, 439–447 (1994).

15. Peyre, M. *et al.* PDGF activation in PGDS-positive arachnoid cells induces meningioma formation in mice promoting tumor progression in combination with Nf2 and Cdkn2ab loss. *Oncotarget* **6**, 32713–32722 (2015).

16. Greene, H. S. N. & Arnold, H. The Homologous and Heterologous Transplantation of Brain and Brain Tumors. *J. Neurosurg.* **2**, 315–331 (1945).

17. Rana, M. W., Pinkerton, H., Thornton, H. & Nagy, D. Heterotransplantation of human glioblastoma multiforme and meningioma to nude mice. *Proc. Soc. Exp. Biol. Med. Soc. Exp. Biol. Med. N. Y. N* **155**, 85–88 (1977).

18. Ueyama, Y. *et al.* Xenotransplantation of a human meningioma and its lung metastasis in nude mice. *Br. J. Cancer* **37**, 644–647 (1978).

19. Rath, P. *et al.* Isolation and characterization of a population of stem-like progenitor cells from an atypical meningioma. *Exp. Mol. Pathol.* **90**, 179–188 (2011).

20.	McCutcheon, I. E. *et al.* Intracranial injection of human meningioma cells in athymic mice: an orthotopic model for meningioma growth. *J. Neurosurg.* **92**, 306–314 (2000).

21.	Russell, W. L. *et al.* Specific-locus test shows ethylnitrosourea to be the most potent mutagen in the mouse. *Proc. Natl. Acad. Sci. U. S. A.* **76**, 5818–5819 (1979).

22.	Morrison, J. P. *et al.* N-ethyl-N-nitrosourea (ENU)-Induced Meningiomatosis and Meningioma in p16INK4a/p19ARF Tumor Suppressor Gene-Deficient Mice. *Toxicol. Pathol.* **35**, 838–845 (2007).

23.	Ostrom, Q. T. *et al.* CBTRUS Statistical Report: Primary Brain and Other Central Nervous System Tumors Diagnosed in the United States in 2011–2015. *Neuro-Oncol.* **20**, iv1–iv86 (2018).

24.	Olson, J. J., Beck, D. W., Schlechte, J. A. & Loh, P.-M. Effect of the antiprogesterone RU-38486 on meningioma implanted into nude mice. *J. Neurosurg.* **66**, 584–587 (1987).

25.	Stepanova, D. S. *et al.* An Essential Role for the Tumor-Suppressor Merlin in Regulating Fatty Acid Synthesis. *Cancer Res.* **77**, 5026–5038 (2017).

26.	Ragel, B. T., Jensen, R. L., Gillespie, D. L., Prescott, S. M. & Couldwell, W. T. Celecoxib inhibits meningioma tumor growth in a mouse xenograft model. *Cancer* **109**, 588–597 (2007).

27.	Karsy, M. *et al.* Combined Hydroxyurea and Verapamil in the Clinical Treatment of Refractory Meningioma: Human and Orthotopic Xenograft Studies. *World Neurosurg.* **86**, 210–219 (2016).

28.	Sahm, F. *et al.* DNA methylation-based classification and grading system for meningioma: a multicentre, retrospective analysis. *Lancet Oncol.* **18**, 682–694 (2017).

29.   Vasudevan, H. N. *et al.* Comprehensive Molecular Profiling Identifies FOXM1 as a Key Transcription Factor for Meningioma Proliferation. *Cell Rep.* **22**, 3672–3683 (2018).

30.   Bi, W. L. *et al.* Genomic landscape of intracranial meningiomas. *J. Neurosurg.* **125**, 525–535 (2016).

31.   Liu, H., Zhang, W., Kennard, S., Caldwell, R. B. & Lilly, B. Notch3 is critical for proper angiogenesis and mural cell investment. *Circ. Res.* **107**, 860–870 (2010).

32.   Shaikh, M. V., Kala, M. & Nivsarkar, M. CD90 a potential cancer stem cell marker and a therapeutic target. *Cancer Biomark. Sect. Dis. Markers* **16**, 301–307 (2016).

33.   Tang, K. H. *et al.* A CD90+ Tumor-Initiating Cell Population with an Aggressive Signature and Metastatic Capacity in Esophageal Cancer. *Cancer Res.* **73**, 2322–2332 (2013).

34.   Yang, Z. F. *et al.* Significance of CD90+ Cancer Stem Cells in Human Liver Cancer. *Cancer Cell* **13**, 153–166 (2008).

35.   Ren, F., Sheng, W.-Q. & Du, X. CD133: a cancer stem cells marker, is used in colorectal cancers. *World J. Gastroenterol.* **19**, 2603–2611 (2013).

36.   Fritchie, K. *et al.* The impact of histopathology and NAB2-STAT6 fusion subtype in classification and grading of meningeal solitary fibrous tumor/hemangiopericytoma. *Acta Neuropathol. (Berl.)* **137**, 307–319 (2019).

37.   Butler, A., Hoffman, P., Smibert, P., Papalexi, E. & Satija, R. Integrating single-cell transcriptomic data across different conditions, technologies, and species. *Nat. Biotechnol.* **36**, 411–420 (2018).

38.   Stuart, T. *et al.* Comprehensive Integration of Single-Cell Data. *Cell* **177**, 1888-1902.e21 (2019).

39.   Hoeppner, M. P. *et al.* An Improved Canine Genome and a Comprehensive Catalogue of Coding Genes and Non-Coding Transcripts. *PLOS ONE* **9**, e91172 (2014).

40.   Newman, A. M. *et al.* Determining cell type abundance and expression from bulk tissues with digital cytometry. *Nat. Biotechnol.* **37**, 773–782 (2019).

41.   Louveau, A., Filiano, A. J. & Kipnis, J. Meningeal whole mount preparation and characterization of neural cells by flow cytometry. *Curr. Protoc. Immunol.* **121**, (2018).

Publishing Agreement

It is the policy of the University to encourage open access and broad distribution of all theses, dissertations, and manuscripts. The Graduate Division will facilitate the distribution of UCSF theses, dissertations, and manuscripts to the UCSF Library for open access and distribution. UCSF will make such theses, dissertations, and manuscripts accessible to the public and will take reasonable steps to preserve these works in perpetuity.

I hereby grant the non-exclusive, perpetual right to The Regents of the University of California to reproduce, publicly display, distribute, preserve, and publish copies of my thesis, dissertation, or manuscript in any form or media, now existing or later derived, including access online for teaching, research, and public service purposes.

DocuSigned by:

Abrar Choudhury

305FFBBDDC5E480...   Author Signature

4/7/2021

Date